Modulated magnetic and structural states

Dynamics and functionalities

Francesco Foggetti

Quantum Materials Theory
Italian Institute of Technology
University of Genova

Contents

List of Publications

Magnetic monopoles and toroidal moments in $LuFeO_3$ and related compounds
F. Foggetti, S. W. Cheong, S. Artyukhin, Phys. Rev. B 100, 180408(R), doi: 10.1103/PhysRevB.100.180408

Soft magnon contributions to dielectric constant in spiral magnets with domain walls
F. Foggetti, A. Pimenov, S. Artyukhin, arXiv:2012.15383

Skyrmion signatures in the ultrafast time domain: coherent and incoherent photo-excited spin dynamics of Néel-type skyrmion host GaV_4S_8
F. Sekiguchi, F. Foggetti, S. Artyukhin, K. Budzinauskas, P. Padmanabhan, R. B. Versteeg, V. Tsurkan, I. Kézsmárki, P. H. M. van Loosdrecht, in preparation

Improper ferroelectricity in metal-organic frameworks
F. Foggetti, A. Stroppa, S. Artyukhin, in preparation

Theory of Devil staircase in $IrTe_2$ F. Foggetti, D. Khomskii, S. Artyukhin, in preparation

Motion of ferroelectric domain walls in spiral magnets
F. Foggetti, S. Artyukhin, in preparation

Magnetic excitations in Ni_3TeO_6
F. Foggetti, S. Artyukhin, in preparation

Introduction

The study and comprehension of the properties of matter has been, and still is, a crucial topic in the development of our civilization. As the characteristics of different materials were revealed, new technologies were built, new phenomena were observed, and new discoveries were made. The knowledge that scientists of the past produced acted as a stepping stone for their successors, enabling them to continue studying and unraveling the hidden treasures that the nature keeps secret.

As the research continues, the possibilities for different materials keep increasing. For example, if we consider materials science, we observe a dramatic increase in the number of new materials created during the last century. We moved from the optimized use of the naturally available resources (i.e. metals, minerals, fuel...) to a situation in which we create new materials according to our needs. We can now construct something completely new, that behaves like nothing known before (2D and layered materials, new alloys, perovskites, organic-inorganic hybrid materials to name a few). As the number of new interesting materials grows, so does their inherent complexity, thus forcing new ways to describe them and new tools to address the problems that come with their study.

Complexity is a key word in this context. As the inner structures of the materials we are studying are becoming less and less trivial, the physics that they host becomes far more complex. As a double edged sword the complexity of a physical system prevents us from an easy description of the latter, but also hides new phenomena that have no analogues in simpler systems. We often refer to the appearing of new physics from a complex background as *emergence*. Examples of emergent physics are collective excitations inside materials (phonons, magnons and other quasi particles) as well as new, unobserved, phases and states of matter.

This Thesis is mainly, but not only, focused on the study of these kinds of excitations. Great importance is given in particular to magnetic excitations (magnons) that will be contextualized with the peculiar orders of the materials that exhibit them. The concept of order is of crucial importance, as the emergence of the properties we try to rationalize is directly caused by the particular order and structure of a material we examine. In this Thesis diverse problems have been reported. The structure of the Thesis is the following: each project has a dedicated Chapter and every Chapter has a brief introduction to make the reader accustomed to the different language, tools, and physical background of the case. The content of the chapters is summarized here:

- In Chapter 1 we study the magnetic excitations of a 2D triangular spin lattice, a structure that has been observed in materials such as hexagonal manganites and ferrites ($RMnO_3$ and $RFeO_3$ with R being a rare earth element). We consider the particular case of $LuFeO_3$, where many of the layers we describe are stacked on top of each other. We study the collective magnetic excitation (magnons) in the lattice in order to identify signatures of elusive magnetic order that this material can host, magnetic monopoles and toroidal moments.

- In Chapter 2 we further exploit the analytical tools developed in Chapter 1. We analyze magnetic and electric excitations in a spin chain where *magnetic frustration* induces a cycloidal arrangement of spins, a configuration observed in materials such as $TbMnO_3$ and $MnWO_4$. We compute the contributions of the excitation to magnetic and electric susceptibilities and discuss how the excitations affect the dielectric properties of the material.

- In Chapter 3 we discuss the properties of the multiferroic GaV_4S_8. Starting from experimental evidences of magnon photoinduced dynamics and thermal transport we perform a simulation based on a realistic microscopic model. The model takes into account the fundamental symmetric (Heisenberg) and anti-symmetric (Dzyaloshinskii-Moriya) spin interactions as well as spin anisotropy and external magnetic field. A combination with LLG equation is used to describe the spin dynamics. This simple asset is sufficient to reproduce the rich phase diagram of the real material for different magnetic fields and temperatures as well as describing the physical behaviour of the coherent and incoherent dynamics of the magnon excitations. This set of tools is then used to address the problem of magnetic phase-dependent thermal conductivity and the photoinduced precession motion of the magnetization.

- In Chapter 4 we discuss a new mechanism for improper ferroelectricity in hybrid organic-inorganic materials. We study (DMA)$Fe^{II-III}(COOH)_3$ (DMA being $NH_2(CH_3)$) where a small ferroelectric polarization has been observed. We use a Landau theory to describe the phase transition that generates the polarization and we compute the phase diagram of the material. As the discovered mechanism is related to the toroidal ordering of DMA molecules and can be extended to other similar structures, we compute the energy barrier for the rotation of DMA molecules in our particular case.

- In Chapter 5 we discuss $IrTe_2$, a layered transition metal dichalchogenide that presents a series of stripe-ordered states. Stripes are formed by Ir dimers. Ir atoms dimerize by shortening their bond length by 20%, and dimers order in stripes throughout the material. We focus on the understanding of the ordering mechanism, a problem that is still not fully comprehended after a decade of research. We combine phenomenological considerations and ab-initio calculations in order to build a simplified model. We use our model to predict the phase diagram of $IrTe_2$. An infinite series of dimerized states is expected as the temperature is lowered, forming a peculiar shape know as Devil's Staircase.

An appendix with the list of acronyms and abbreviations, as well as a complete list of bibliographic references, is given at the end.

Chapter 1

Magnetic monopoles, toroidal moments and non-reciprocal magnons in hexagonal Manganites and Ferrites

1.1 Introduction

In the study of a material, a great number of factors can affect its characteristics. The possible sources of interesting properties can be related to the contemporary presence of several ingredients, i.e. the particular composition of the material, the oxidation states of the individual atoms, the geometrical disposition of its elements, the presence of order or symmetries, the breaking of symmetries, the presence of lattice distortions, and competing internal forces.

Different behaviors in the materials are observed as one or more of these characteristics become dominant over the others. We distinguish the materials according to these behaviors, classifying them into macro categories or classes.

A fascinating class of materials that we will focus our attention on is the class of *multiferroics*. As the name suggests multiferroic materials host multiple *ferroic* orders, resulting in a material that may have ferromagnetic and ferroelectric order in the same phase, thus exhibiting both magnetic and ferroelectric properties. In fact, multiferroics show, aside from the already mentioned ferroelectricity and ferromagnetism, a plethora of other properties such as electrostriction, magnetostriction, piezoelectricity, and magnetoelectricity [1]. Multiferroic materials are attracting attention due to their versatility and the great number of potential applications [2].

In this Chapter we will study the magnetic properties of hexagonal $LuFeO_3$, a multiferroic material that, at room temperature, possesses a weak ferromagnetic moment [3, 4]. As the magnetic properties come from the Fe atoms (Lu^{3+} is non-magnetic), we model the magnetic subsystem as a stack of layers with a triangular lattice that matches the disposition of Fe atoms inside the material (Fig. 1.1). This study can be generalized to the entire group of hexagonal manganites and ferrites RMO_3 with R being a rare earth element and M a magnetic ion (M=Mn,Fe). Magnetic ions in these compounds arrange themselves in triangular layers allowing us to broaden the validity of our model to a great number of materials withing this group.

The magnetic properties of the system we are considering are a consequence of the

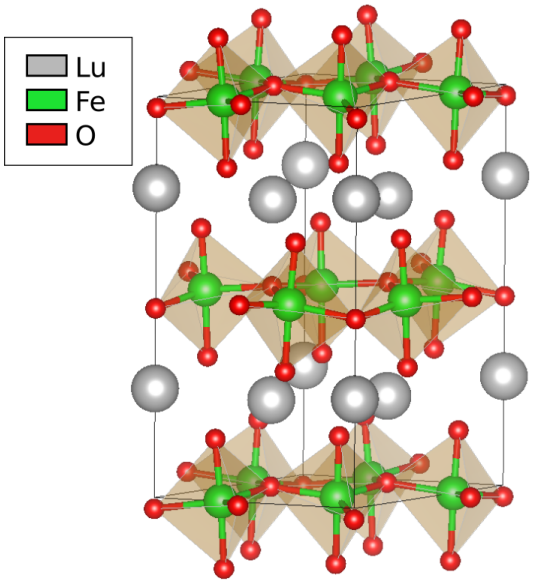

Figure 1.1: Structure of $LuFeO_3$ contains the layers of corner-sharing FeO_5 bipyramids, interspaced with layers of Lu ions (grey), arranged on a triangular lattice. Fe ions with $S = 5/2$ are positioned in a triagular lattice.

interaction between the magnetic ions of the material. The interaction between nearest neighbor magnetic ions is of the antiferromagnetic (AFM) kind and thus favors an antiparallel orientation of the spins of the ions. The triangular disposition of the ions does not allow for all the spins to be antiparallel on a triangle, due to the odd number of bonds. This situation is referred to as geometric frustration, and forces a different kind of ordering. In this case the frustrated interactions favor an angle of 120° between neighboring spins, as seen in Fig. 1.2.

There are multiple reasons that make AFM triangular lattices worth studying. They host peculiar orders, and the magnetic excitations in the lattice may be utilized to manipulate information without electric currents [5]. Moreover the frustrated spin texture may allow for the presence of particular topological objects e.g. magnetic monopoles, toroidal moments, spirals and skyrmions. Our study will focus on the peculiar magnetic excitations and on two elusive topological objects that can exist in this framework, magnetic monopoles and toroidal moments.

This Chapter has the following structure: we first define the mathematical framework that maps the real material into our model. Semiclassical approximation for spins and Hamiltonian mechanics will be used along with linear spin wave theory to study the dynamics of the spin excitations (magnons). We discuss how the presence of distortions in the real material breaks the symmetry in the lattice and allows for the emergence of magnetic monopoles and toroidal moments. A general analysis of the symmetries of the system is then performed highlighting the most interesting features of the excitations. In the last part a simulation of inelastic neutron scattering shows the magnon spectrum and predicts magnon non-reciprocity within a suitable region of the momentum-space.

1.2 Triangular lattice: outline

We model hexagonal $LuFeO_3$ with a 2D triangular lattice. This choice is made to mimic the structure of $LuFeO_3$ and of hexagonal ferrites and manganites in general. Lu^{3+} and O^{2-} are nonmagnetic, while Fe^{3+} has five unpaired electrons in the outer 3d shell and thus spin equal to 5/2. Fe and Lu atoms are arranged in separate planes with the atoms being the vertices of equilateral triangles, as seen from the structure of the material shown in Fig 1.1. As the magnetic properties only come from Fe atoms we map the real material into a set of 2D planes stacked on top of each other with spins localized at the sites of the lattice and with interlayer and intralayer interactions between spins. It is worth mentioning that the oxygens instead are arranged in six-faced bypiramids with the Fe ions in the center. We will focus more on the role of the oxygens later in this chapter as a small buckling of the bypiramids induces distortions in the material, thus setting the stage for the more intriguing features to be described.

We now discuss the details of the quasi-2D spin lattice model. At this level we only consider spin interactions of the symmetric Heisenberg type: the interaction between two neighboring spins at sites i and j will be of the type $\mathbf{S}_i \cdot \mathbf{S}_j$. It is known from experiments [6] that in-plane interactions are of the AFM type, so if we only have two spins the interaction energy has the form

$$\mathcal{H}_{int}^{ij} = J\mathbf{S}_i \cdot \mathbf{S}_j \tag{1.1}$$

where $J > 0$ is the AFM coupling constant and the energy is minimized if the scalar product of the spins is equal to -1 i.e. the spins are antiparallel. In the 2D lattice the situation is less trivial because the triangular arrangement of spins does not allow for a trivial (parallel or antiparallel) configuration of spins. Let us consider the easiest non-trivial case, that of three spins on the vertices of an equilateral triangle (Fig. 1.2).

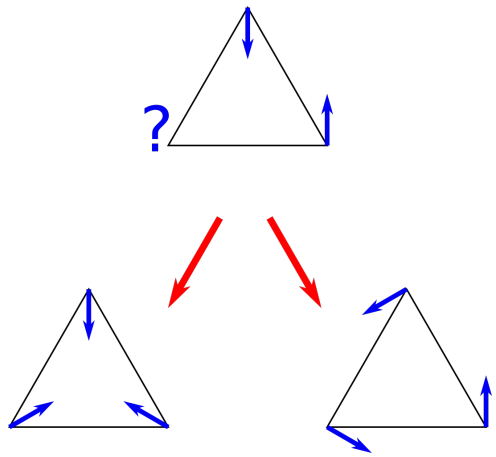

Figure 1.2: Frustration of three spins on the vertices of a triangle. As it is not possible for the three spins to be all antiparallel at the same time a new configuration is favoured and the spins arrange themselves with an angle of 120° between each other.

The Heisenberg interaction of three spins is described by the Hamiltonian

$$\mathcal{H} = J(\mathbf{S}_1 \cdot \mathbf{S}_2 + \mathbf{S}_1 \cdot \mathbf{S}_3 + \mathbf{S}_2 \cdot \mathbf{S}_3) \tag{1.2}$$

which can be rewritten as

$$\mathbf{S}_1 \cdot \mathbf{S}_2 + \mathbf{S}_1 \cdot \mathbf{S}_3 + \mathbf{S}_2 \cdot \mathbf{S}_3 = \frac{1}{2}[(\mathbf{S}_1 + \mathbf{S}_2 + \mathbf{S}_3)^2 - (\mathbf{S}_1^2 + \mathbf{S}_2^2 + \mathbf{S}_3^2)] \tag{1.3}$$

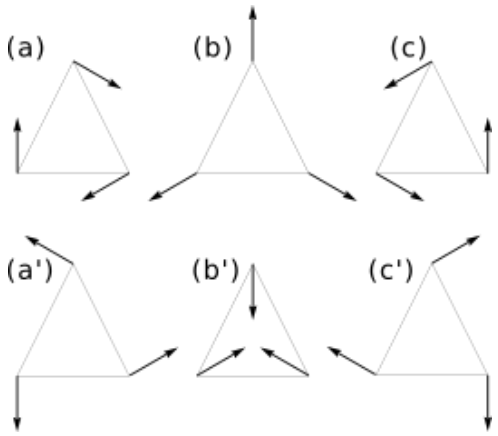

Figure 1.3: Possible spin configurations, compatible with a triangular lattice. (a,c) Inward and (a',c') outward toroidal moment. (b) Outward and (b') inward monopole. A monopole is generated on a triangle between two opposite toroidal moments. Notice that outward toroidal moments are associated to inward monopole and vice versa.

thus, redefining the energy up to a constant. We can then rewrite Eq. (1.2) as

$$\mathcal{H} = \frac{J}{2}(\mathbf{S}_1 + \mathbf{S}_2 + \mathbf{S}_3)^2 \tag{1.4}$$

which is minimized when $\mathbf{S}_1 + \mathbf{S}_2 + \mathbf{S}_3 = 0$. As all spins have the same modulus, this condition is realized when the angle between two spins is 120°.

Extending this argument to an infinite 2D lattice, we see that the directions of all spins on the lattice are completely defined once one single triangle on the lattice is fixed, the triangles composing the lattice adopt two (four if we consider an inward or outward orientation) possible spin configurations that we will call monopolar and toroidal configurations (Fig. 1.3). We refer to these textures as "magnetic monopoles" and "toroidal moments" in reference to the hypothetical particles that would create the associated magnetic field lines [7]. In the monopolar case the magnetic field lines are directed towards the center of the triangle, inward or outward, like it would be if a single hypothetical magnetic charge was positioned there. In a similar way the magnetic field in the toroidal configuration runs around the triangle in a torus-shaped way or, equivalently, like if a current perpendicular to the triangle plane was running through the center of the triangle. We can clarify these definitions by associating to the monopolar configuration a "monopolar charge" or "monopolar magnitude" $\mathbf{r}_i \cdot \mathbf{S}_i$ and by defining properly the toroidal moment as $\mathbf{r}_i \times \mathbf{S}_i$ where a summation over the index $i = 1, 2, 3$ is considered. These quantities are respectively maximized for pure monopolar and toroidal configurations.

However, there is one last consideration that we must make: in a perfect 2D triangular lattice all triangles have the same size, are equivalent, and thus when an infinite lattice exhibits the alternating monopolar and toroidal order the different contributions of the two objects cancel each other. To better understand this last statement we must point out that the alternating monopoles and toroidal moments on the lattice can be thought of in terms of opposite toroidal moments. A monopole can in fact be though as the transition region between two opposite toroidal moments (Fig. 1.3 (b,b')). With this configuration in mind it is easier to comprehend that for equivalent triangles magnetic monopoles and toroidal moments (or equivalently opposite toroidal moments) will compensate each other to a net zero contribution and no macroscopic order.

As we anticipated in the introduction there is a key factor that provides for the existence of monopolar or toroidal order that breaks the duality we describe above. It allows for one of the two configurations to become dominant in the total balance and to establish an ordering for the whole material. We refer to distortions in the material that induce trimerization of the triangles [8]. (Fig. 1.4).

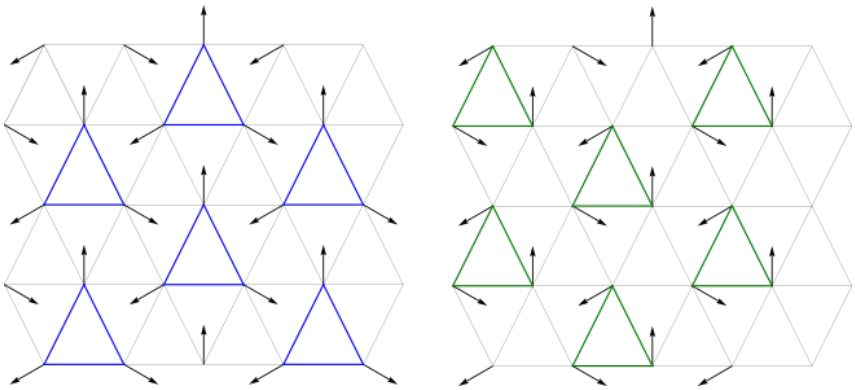

Figure 1.4: Trimerization in the lattice: as some bonds become shorter the strength of the bonding increases thus making some triangles inequivalent to the others. The contribution from the monopole charge (blue) or from the toroidal moment (green) of these triangles (bold in figure) will be greater than the regular ones, hence defining a global monopolar or toroidal order for the whole material.

This argument is general for hexagonal manganites and ferrites. As oxygen atoms are positioned around one central iron atom to form triangular bipyramids (Fig. 1.1 it is possible for the axes of these pyramids to cant. Corner-sharing bipyramids are interconnected among each other, therefore the tilting of a single bipyramid affects the others too. We observe that a buckling of three bipyramids towards the center of the iron triangle makes that triangle smaller (i.e. the bonds between irons are stronger), but at the same time this causes the nearby triangles to become bigger (i.e. with weaker bonds) because of the shared apical oxygen moving away from the center of the triangle (Fig. 1.5).

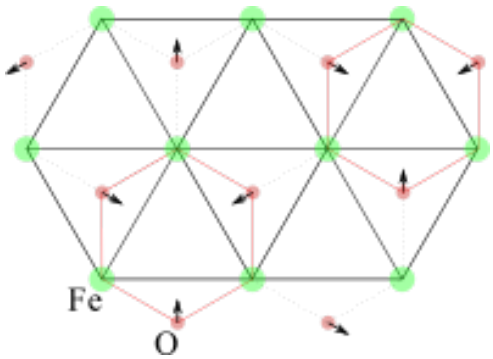

Figure 1.5: Trimerization due to buckling of bipyramids. Oxygens (red) are responsible for the exchange interaction between iron ions (green). As the oxygen bipyramids are tilted, apical oxygens move towards the center of an iron triangle (red hexagons), therefore strengthening the bonds and making the bonds of nearby triangles weaker.

1.3 Hamiltonian of the system

In this section we describe the model developed to study the magnetic excitations in the 2D lattice introduced in the previous section, and our method to solve it. The Hamiltonian we use is the following

$$\mathcal{H} = \sum_{ij} \left(J_{ij}\mathbf{S}_i \cdot \mathbf{S}_j + \mathbf{D}_{ij} \cdot \mathbf{S}_i \times \mathbf{S}_j\right) + \sum_i \left(-K(\mathbf{S}_i \cdot \mathbf{n}_i)^2 + K'(S_i^z)^2 - g\mu_{\mathrm{B}}\mathbf{H} \cdot \mathbf{S}_i\right). \quad (1.5)$$

The first term describes the intralayer AFM Heisenberg interaction and the FM interlayer interaction as the site indices i and j select spins belonging to the same plane or to two adjacent planes. The second term describes the antisymmetric Dzyaloshinkii-Moriya (DM) interaction [9, 10, 11] between nearest neighbor (NN) spins in the same plane [12]. The DM vector $\mathbf{D}_{ij} = \alpha_{DM}\mathbf{r}ij \times \boldsymbol{\delta}$ is computed from the structural data of the material. Here α_{DM} is a coupling constant, while $\mathbf{r}_{ij}$ connects two neighboring irons at sites i and j; $\boldsymbol{\delta}$ connects the middle point of $\mathbf{r}_{ij}$ to the closest oxygen. The terms with K and K' are anisotropy terms. The term with K represents the easy axis anisotropy within ab-plane, induced by trimerization, and $\mathbf{n}_i$ are the shifts of apical oxygens projected in the *ab*-plane. K' defines a hard-axis anisotropy that is perpendicular to the iron layers and forces the spin to lay in the 2D plane. The last term describes the effects of an external magnetic field $\mathbf{H}$ on the spins, $g = -2$ is the gyromagnetic ratio and μ_B the Bohr magneton.

We are able to select between a state that favours toroidal order over the monopolar one, or vice versa by manipulating the parameters in the model. In particular it is sufficient to only alter two parameters in the model to obtain the configurations we want to explore: the easy axis constant K and the interlayer coupling J'. By changing the sign of K we rotate the easy axis by 90° which transforms the easy direction into a hard direction.

This affects the spin structure: a positive K sets the easy direction along the shifts of the apical oxygens, thus leading to monopolar ordering (e.g. A2 and B1 phases in Fig. 1.6), while a negative K leads to a perpendicular in-plane direction to be an easy one, resulting in toroidal states, such as A1 and B2 in Fig. 1.6). Therefore if, for example, before the switching of anisotropy the spins were arranged in monopolar order, after the rotation of the easy axis we would have a toroidal order as the dominant one. Hence the sign of K selects one of the two possible states in each layer, monopolar or toroidal.

The sign of J' instead sets the relative orientation of spins in adjacent magnetic layers, so that for FM J' ($J' < 0$) the toroidal moments or monopolar charges in adjacent planes are the same, and for $J' > 0$ they alternate. Therefore the number of possible phases selected by K and J' is four. Fig. 1.6 shows the four phases that in literature are denoted as A_1, A_2, B_1, B_2 [13]. For example, $K < 0$ and $J' < 0$ results in a toroidal order with the same toroidal moment in all magnetic layers, as seen in the A1 state.

1.4 Monopoles, toroidal moments and non-reciprocity

In Section 1.2 we explained that the 120° spin order in conjunction with lattice trimerization may lead to the emergence of a toroidal or monopolar order. Strikingly, these orders result in non-reciprocal magnon propagation, a phenomenon that leads to a different absorption of neutrons with opposite wavevectors. Of fundamental importance for this endeavor will be the non-reciprocal character of particular magnons that we first identify with a general symmetry analysis. In the following section we simulate INS spectra to

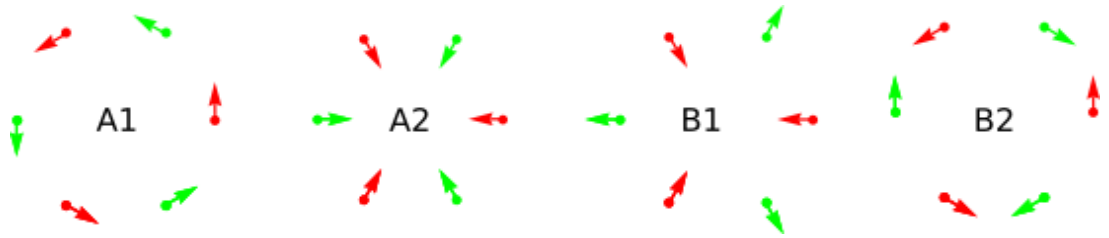

Figure 1.6: The four spin configurations that we considered. Red and green arrows represent spins from two adjacent layers. Configurations A1 (B1) and B2 (A2) are toroidal (monopolar) phases with, respectively, FM and AFM interlayer coupling.

demonstrate how they can be used to identify the monopolar and toroidal states and discriminate between them.

	$2_{001}\|(00\frac{1}{2})$	2_{110}	I	3_z	T
$(\mathbf{r}_i \times \mathbf{S}_i)_z$	+	−	−	+	−
$\mathbf{r}_i \cdot \mathbf{S}_i$	+	+	−	+	−
k_z	+	−	−	+	−
P_z	+	−	−	+	+
H_z	+	−	+	+	−
$(\mathbf{k} \times \mathbf{H})_z$	+	−	−	+	+
Phases					
A_1	+	−	−	+	−
A_2	+	+	−	+	−
B_1	−	+	+	+	−
B_2	−	−	+	+	−

Table 1.1: Transformation properties of relevant physical quantities (toroidal moment, monopolar charge; wave vector, ferroelectric polarization and magnetic field components; Pointing vector of the electromagnetic field; order parameters of magnetic phases) under the generators of the group $P6_3/mmc$. Notice that phases A_1 and A_2 transform, respectively, as a toroidal moment and a magnetic monopole. 2_{001} is a 180° rotation around c axis, combined with a translation along c by half a cell constant; 2_{110} is a 180° rotation around [110] axis, I is the inversion operation, 3_z is 120° rotation around c axis; T is the time reversal operation.

We now proceed with a systematic symmetry analysis of the different orders we just introduced. This analysis allows us to extract general information that will be used as a guide to drive our study. Table 1.1 shows the transformation properties of important physical quantities under the generators of the group $P6_3/mmc$, a high-temperature parent structure of hexagonal ferrites. This information is of fundamental importance as it tells us how to combine different objects to obtain symmetry-allowed terms that may contribute to the symmetry invariants such as a neutron absorption cross-section, magnon dispersion, or a free energy of the system. The presence of wave vector-odd terms in the magnon dispersion signifies non-reciprocal effects. We will show that terms that induce non-reciprocal propagation of magnons are allowed by symmetry. The following statements follow from this analysis:

- A toroidal moment along the c axis $(\mathbf{r}_i \times \mathbf{S}_i)_z$ can generate a non-reciprocal magnon in that direction. This is due to the term $k_z(\mathbf{r}_i \times S_i)_z$ being invariant under all

the symmetries of $P6_3/mmc$. The immediate implications are that INS data should report a contribution to the magnon dispersion $\omega(\mathbf{k})$ that is linear in k_z, i.e. non reciprocal, as in fact our simulation does in Fig. 1.7(e);

- On the contrary, the presence of monopoles alone (with $P_z = 0$) cannot induce non-reciprocity of spin wave propagation along the c axis, because $k_z(\mathbf{r} \cdot \mathbf{S})$ is not invariant. As there are no contributions to $\omega(\mathbf{k})$, linear in the components of k, there is only reciprocal propagation, as seen in the simulated spectra in Fig. 1.9(f);

- Non reciprocal spin waves are still possible in the presence of monopoles. In fact, an invariant term $P_z[\mathbf{k} \times \mathbf{H}]_z$ is allowed. When $\mathbf{k}$ and $\mathbf{H}$ are in the $[ab]$ plane, the invariant term is exactly $\mathbf{P} \cdot [\mathbf{k} \times \mathbf{H}]$ which is equivalent to $\mathbf{k} \cdot [\mathbf{H} \times \mathbf{P}]$. If the polarization is parallel to the c axis, the term $\mathbf{H} \times \mathbf{P}$ is only in-plane and non-reciprocal magnon propagation in the ab plane is possible.

- Magneto-electric (ME) effect results from the presence of monopoles. The term $(\vec{r} \cdot \vec{S}) P_z H_z$ is an invariant quantity and it introduces a coupling between an external magnetic field and the polarization inside the material.

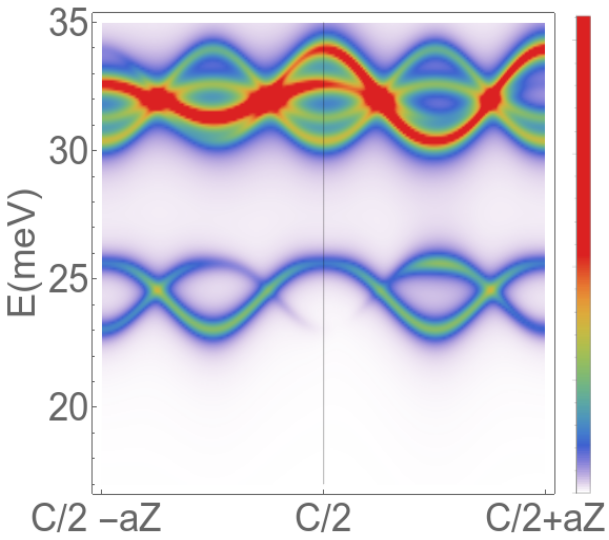

Figure 1.7: Non reciprocal magnon in INS simulation, computed in a toroidal phase. C/2 is the middle point between C and Γ points (cf. Fig. 1.8(c)), "aZ" refers to a small deviation from C/2 along k_z direction. Further details on this figure, and discussion of the methods used to compute the INS data are provided in Section 1.6.

An important clarification must be made: our symmetry analysis describes terms that are allowed by symmetry in the magnon dispersion, but it gives no information on the constants that come with them. We cannot yet establish which terms give important contributions and which are negligible. As such, in the following INS simulations we were able to see magnon non-reciprocity along k_z in the toroidal state, while the in-plane non-reciprocity in the monopolar state is not seen.

1.5 Magnetic dynamics

We now focus on computing the spin dynamics generated by the Hamiltonian (1.5). In order to obtain magnon excitations and a correct description of inelastic neutron scattering we use linear spin wave theory. For $S = 5/2$ a semiclassical treatment is justified. Because the modulus of spins is constant, we can express a generic spin at site i in terms of spherical coordinates with angles (θ_i, ϕ_i)

$$\mathbf{S}_i = (\sin\theta_i \cos\phi_i, \sin\theta_i \sin\phi_i, \cos\theta_i) \tag{1.6}$$

We expand the Hamiltonian around its ground state, chracterized by θ_{i0}, ϕ_{i0}, the values at the minimum of the spherical coordinates θ and ϕ of the spin at site i. Then we introduce α_i and β_i as small deviations from the ground state so the rule for the expansion will have the form

$$\begin{aligned} \theta_i &= \theta_{i0} + \alpha_i, \\ \phi_i &= \phi_{i0} + \beta_i. \end{aligned} \tag{1.7}$$

With this choice of coordinates the Hamilton equations are:

$$\begin{aligned} \dot{\theta}_i \sin\theta_i &= \frac{\partial \mathcal{H}}{\partial \phi_i} \\ \dot{\phi}_i \sin\theta_i &= -\frac{\partial \mathcal{H}}{\partial \theta_i}. \end{aligned} \tag{1.8}$$

It is straightforward to justify the $\sin\theta$ term and the shape of these equations if we consider the equivalent Lagrangian formulation [14].

$$\mathcal{L} = \sum_i \dot{\phi}_i \cos\theta_i - \mathcal{H}. \tag{1.9}$$

After expanding the Hamiltonian around the ground state, equations (1.8) take the form:

$$\begin{aligned} \dot{\alpha}_i &= \frac{1}{\sin\theta_{0i}} \frac{\partial \mathcal{H}}{\partial \beta_i}, \\ \dot{\beta}_i &= -\frac{1}{\sin\theta_{0i}} \frac{\partial \mathcal{H}}{\partial \alpha_i}. \end{aligned} \tag{1.10}$$

The ground state around which we expand the equations is computed through a numeric minimization of Eq. (1.5). The resulting configuration is very close to the 120° spin order we described in the previous section, with small deviations due to the DM term and the easy axis anisotropy term that, being driven by the oxygen displacements, slightly moves the spins away from the ideal 120° order. This expansion makes possible an analytical solution of the equation of motion and allow prediction of the magnon spectrum. More details are given in Appendix B. In order to gain insight into the spectrum, we need to move the problem into the Fourier space. To do so, we use the transformations,

$$\beta_j = e^{i\mathbf{k}\mathbf{r}_j - i\omega t}\beta_k, \qquad \alpha_j = e^{i\mathbf{k}\mathbf{r}_j - i\omega t}\alpha_k \tag{1.11}$$

where $\mathbf{k}$ is the momentum vector, $\mathbf{r}$ is the lattice vector and ω is the frequency. Thus in the Fourier space the equation of motions take the form of an eigenvalue problem:

$$(A - i\omega \mathbb{1}) \begin{pmatrix} \alpha_k \\ \beta_k \end{pmatrix} = 0, \qquad A = \begin{pmatrix} \partial_{\beta_i \alpha_j} & \partial_{\beta_i \beta_j} \\ -\partial_{\alpha_i \alpha_j} & -\partial_{\alpha_i \beta_i} \end{pmatrix} \mathcal{H}. \tag{1.12}$$

Here A is the $2n \times 2n$ matrix of the second derivatives of the Hamiltonian with respect to α_k, β_k, and n is the number of spins in the unit cell. We can now obtain the entire spectrum of the system by solving the eigenvalue problem, Eq. (1.12), thus obtaining the frequency (energy) of the magnons as a function of the momentum $\mathbf{k}$. In the next section we will show how to compute the response of the system to an external beam of neutrons.

1.6 Unpolarized inelastic neutron scattering

In the previous section we have built a general Hamiltonian of the system under study, expanded it around its ground state and showed how to obtain the magnon frequencies from the Hamilton equations. We now utilize this procedure to simulate INS spectra in the case of monopolar and toroidal orders, so that we can compare the results from our model with experimental data.

Neutrons are a powerful probe to investigate the inner magnetic structure of a material. As they possess no electric charge, they can travel through matter without being disturbed by atomic electric fields. They possess a magnetic moment μ_N that is responsible for the magnetic interaction with the spins in the material. Due to the small size of the nucleus compared to the neutron de-Broglie wavelength, the atomic part of the interaction is described by a delta-function, leading to an isotropic atomic scattering cross-section. Therefore neutrons proved themselves to be a useful and relatively clean probe to measure the magnetic excitations and lattice vibrations of materials. We represent the neutron beam by an oscillating magnetic field $\vec{h}e^{-i\Omega t}$, where the frequency Ω is related to the energy of the beam. When a neutron of frequency Ω interacts with the material it can excite a magnon with the same frequency (if a mode with that frequency is present). When this happens the momentum of the neutron changes. When it is collected by the detector, the comparative difference with the initial momentum gives information on the magnons that have been excited by the neutron. In this way, it is possible to compute the spectral function for the magnons by computing the cross section of the interaction between neutrons and the system. The action of the neutron beam will act as an external force term in Eq. (1.12). We can now reformulate the problem including the external contributions

$$(A - i\omega\mathbb{1}) \begin{pmatrix} \alpha_k \\ \beta_k \end{pmatrix} e^{-i\omega t} = \begin{pmatrix} h_\alpha \\ h_\beta \end{pmatrix} e^{-i\Omega t}, \tag{1.13}$$

with h_α and h_β being the terms in $\vec{S} \cdot \vec{h}$, linear in α_i and β_i, respectively.

We keep the time-dependent exponential terms with ω and Ω to explain in detail the following point: the system will respond to the oscillating magnetic field only if the field associated with the neutrons has the same frequency as one of the magnons in the spectrum. Mathematically this is apparent from the Fourier transform of the system, where the two time-dependent exponential terms give rise to $e^{-i(\omega-\Omega)t}$, that is a highly oscillating integrand for different frequencies. Non-zero contributions result only when $\omega = \Omega$, meaning that the neutron beam excites a magnon only if it has the frequency (energy) matching one of the magnons.

Solving Eq. (1.13) for all ω gives expressions for α_k and β_k as functions of ω; if we substitute α_k and β_k in the spherical coordinate expression for $\mathbf{S}$, we can express the spin response to the external magnetic field as an ω and k dependent quantity. To obtain the magnetic cross section we need to compute the magnetic susceptibility tensor, which, for

the uniform spiral in the xy plane takes the form:

$$\chi_{ij}(\omega, k) = \frac{g\mu_B}{V} \frac{\partial S^{(i)}(\omega, k)}{\partial h^{(j)}(\omega, -k)}, \tag{1.14}$$

where V is the volume of the unit cell.

In the experiment [15] a non-polarized neutron beam is used, therefore we must average over all possible spin polarizations of the neutrons. The expression for the INS cross section due to magnetic dipole-dipole interactions of spins with neutrons in a non-polarized neutron beam is given by [16]

$$\frac{d^2\sigma}{dEd\Omega} \sim \sum_{ij} \left(\delta_{ij} - \frac{k_i k_j}{k^2}\right) \chi_{ij}. \tag{1.15}$$

Equation (1.15) can be easily generalized to the polarized neutron scattering case by introducing operators that project onto one of the spin polarizations.

We have defined the theoretical framework to simulate an INS experiment. The only undefined quantities are now the parameters that appear in the model (1.5). We use the parameter values of $J = 2.8$ meV, $|J'| = 0.3$ meV, $H_x = 2$ T, $K' = 0.3$ meV, $|K| = 0.68$ meV/Å^2 $\alpha_{DM} = 0.05$ meV/Å^2. These values are chosen to reproduce the experimental inelastic neutron scattering data (Fig. 1.8) [15]. The values for J and K were chosen according to published values [15], while we adopted the above values of the remaining parameters to better match the simulated spectra with the experimental ones. Particular attention was given to the gap at the Γ point in the spectrum and the energy of the plateaux between A and B points. We tuned the parameters of the model to describe these experimental features.

INS spectra for toroidal and monopolar orders A1 and A2 are reported in Fig. 1.9. We see from panels (a-b) that the differences between the two spectra in the plane $[k_x, k_y]$ are present but small. As we did not observe in-plane non reciprocity, we suppose that even if these non-reciprocal magnons are allowed in monopolar state the actual non-reciprocal contribution to the magnon dispersion is negligible. In panel (e) non-reciprocity along k_z is evident, consistent with the expectations from our symmetry analysis.

A more extensive study of the different phases is portrayed in Figures 1.10 and 1.11. We plotted the simulated INS spectra for all four orders under the same parameters as used for Fig. 1.9. Additionally, we verified the effect of DM interaction on the spectrum. We show that the observed non-reciprocity in A1 is independent of the presence of DM interaction. The state B2 displays non reciprocal behaviour only for high valued DM, highlighting a weak non-reciprocal character of the magnon.

1.6.1 Magnetic quadrupole contribution

In our study so far we did not consider the possible presence of magnetic quadrupole moments. Monopoles and toroidal moments are terms of multipole expansion of the general vector potential $\mathcal{A}$. As is common in this kind of expansions, higher order terms give small corrections with respect to lower-order terms. Monopoles and toroidal moments appear in this expansion, respectively, as zero-order and second-order terms [17] (first order terms are magnetic dipoles that are absent in our system). The second order expansion also includes a quadrupole moment. This is why, in principle, the magnetic

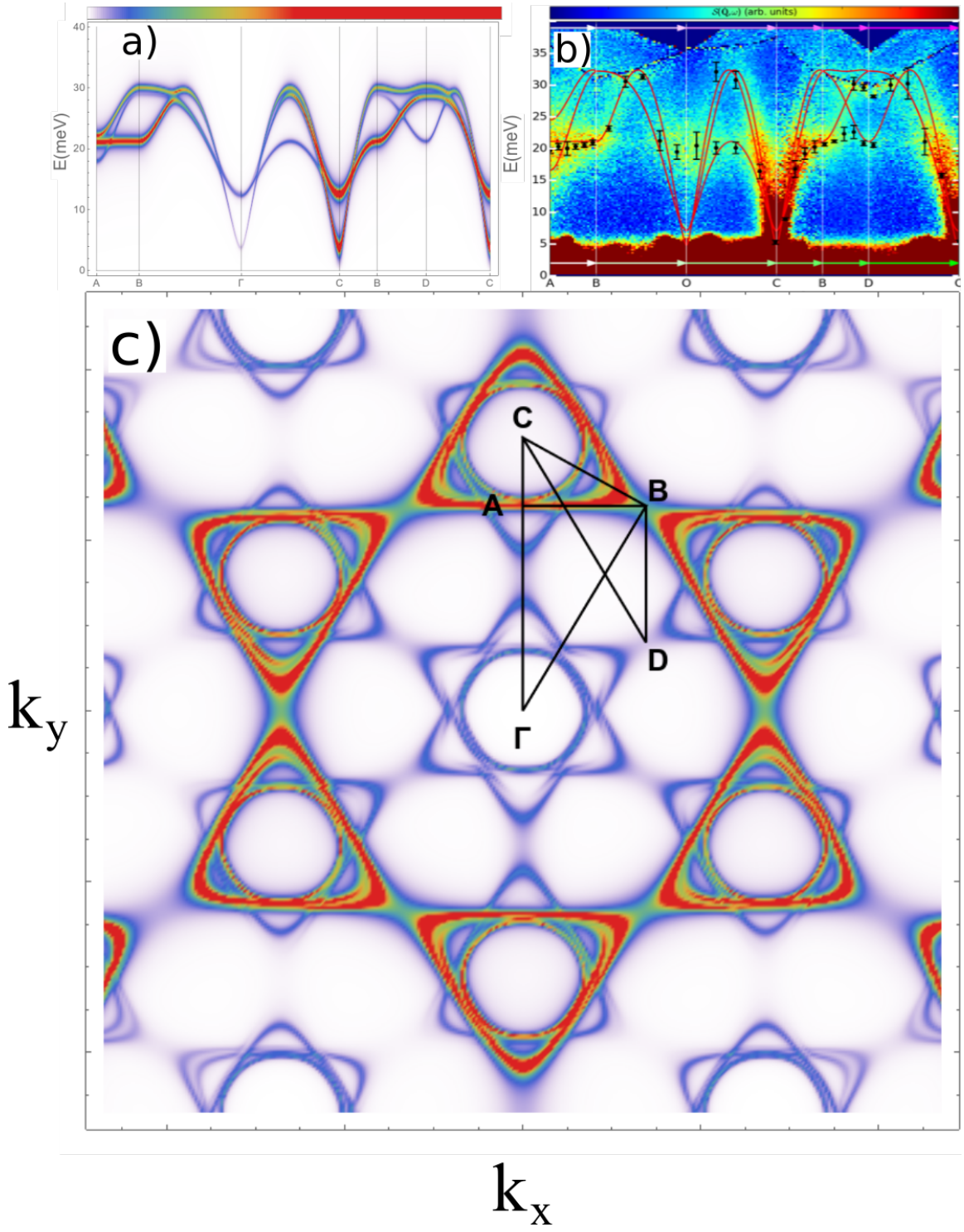

Figure 1.8: INS simulation: (a) simulated neutron scattering cross-section for $LuFeO_3$, color scale encodes INS cross section. The values of the parameters used in the simulation are chosen to match the features of the experimental data from [15] (that are shown in Panel (b)). (c) Constant energy cut $E = 20$ meV of the simulated neutron scattering cross-section. The path used in (a) and (b) is indicated with black solid lines.

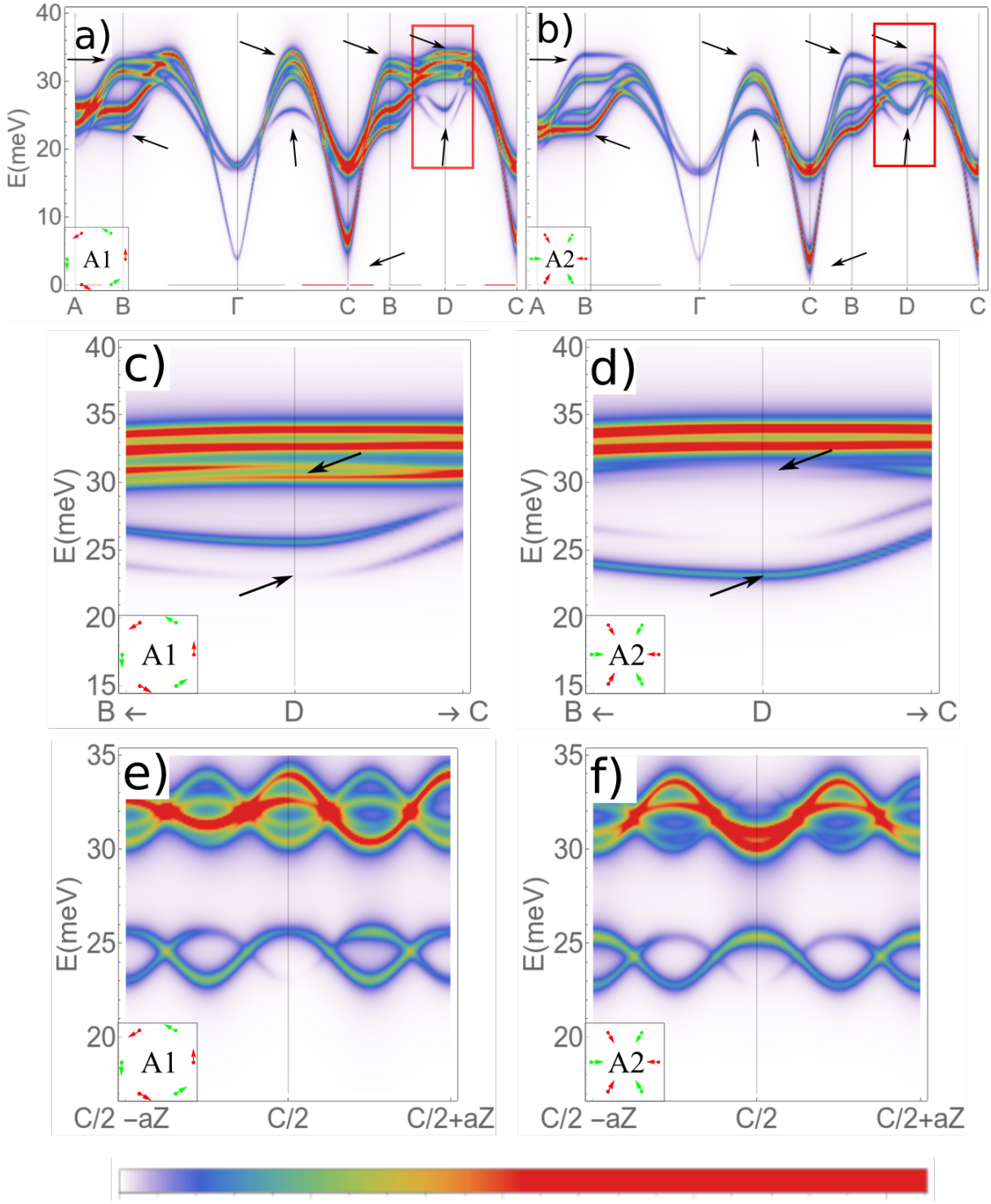

Figure 1.9: INS computed for A1 (toroidal) and A2 (monopolar) phases, shown in insets. Color scale encodes INS cross section. (a-b) inelastic neutron scattering intensity computed along the k-path defined in Fig. 1.8(c). Arrows point to the differences between the two phases. The red box highlights the region that is enlarged in panels (c-d). (e-f) Close-up on a midpoint of C-Γ interval: INS intensity along k_z direction. "aZ" refers to a small deviation from C/2 along k_z direction. Non-reciprocal magnon excitation is evident in panel (e), where the excitation intensity is not symmetric.

quadrupole moment could give contributions as important as the toroidal moment. The second-order contributions to the vector potential are

$$\begin{aligned}\langle \mathcal{A}^{(2)}_{quad}(R)\rangle_i &= -\epsilon_{ijk} q_{kl} \partial_j \partial_l \frac{1}{R}, \\ \langle \vec{\mathcal{A}}^{(2)}_{tor}(R)\rangle &= \nabla(\vec{t}\cdot\nabla)\frac{1}{R} + 4\pi\, \mathbf{t}\, \delta(\vec{R}),\end{aligned} \tag{1.16}$$

where $\langle ... \rangle$ represents the time average and q_{kl} and $\mathbf{t}$ are the quadrupolar and toroidal moments:

$$\mathbf{t} = -\frac{1}{2} g\mu_B \sum_\alpha \mathbf{r}_\alpha \times \mathbf{S}_\alpha, \tag{1.17}$$

$$q_{ij} = -\frac{g\mu_B}{2} \sum_\alpha (S_{\alpha i} r_{\alpha j} + S_{\alpha j} r_{\alpha i}), \tag{1.18}$$

where the index α runs over the different spins that contribute to $\mathbf{t}$ or q_{ij}.

As the symmetry analysis in Table 1.1 shows, in the presence of a toroidal moment a non-reciprocal magnon is generated. We want to verify if the quadrupolar moment contributes to non-reciprocity too, i.e. if there exists an invariant, linear in $\mathbf{k}$, that contains q. We can greatly simplify the expression for q by taking into account that q is invariant under 120° rotation around the z axis

$$\begin{pmatrix} -\frac{\sqrt{3}}{2} & -\frac{1}{2} & 0 \\ \frac{1}{2} & -\frac{\sqrt{3}}{2} & 0 \\ 0 & 0 & 1 \end{pmatrix} \cdot \begin{pmatrix} q_{11} & q_{12} & q_{13} \\ q_{21} & q_{22} & q_{23} \\ q_{31} & q_{32} & q_{33} \end{pmatrix} = \begin{pmatrix} q'_{11} & q'_{12} & q'_{13} \\ q'_{21} & q'_{22} & q'_{23} \\ q'_{31} & q'_{32} & q'_{33} \end{pmatrix}. \tag{1.19}$$

By imposing $q_{ij} = q'_{ij}$ it follows that only the q_{33} component of the quadrupole moment can be non-zero. If no external fields are present, the tensor q_{ij} can only be contracted with the vectors $\mathbf{k}$ and $\mathbf{P}$ in a term like $k_i q_{ij} P_j$. In our case, the vector P is along the c axis and, given the form of q from Eq. (1.19), the only possible term is $k_z q_{33} P_z$.

Therefore, in principle, the quadrupole moment can contribute to the non-reciprocity of the magnon. However, calculating the quadrupolar moment using Eq. (1.18), we find it to be much smaller than that of the toroidal moment. This reveals that our analysis is not affected by having neglected the quadrupole term in the expansion.

1.7 Conclusions

In this Chapter we discussed a mechanism through which a toroidal or monopolar order emerges in a 2D triangular lattice. The particular order arises from a combination of the 120° spin order (due to the frustrated AFM interaction) and the structural trimerization. These two elements are present in general in hexagonal manganites and ferrites, suggesting a generalization of our model for the entire class of materials.

A realistic microscopic model has been used to simulate INS experiments. Good agreement with experimental data is found and validates the reliability of the model. A general symmetry analysis is provided in order to help identify the cases where elusive magnon non-reciprocity is induced by monopoles and toroidal moments. We hope that the predicted magnon non-reciprocity, associated with the presence of toroidal order, will help identify that order in the future experiments.

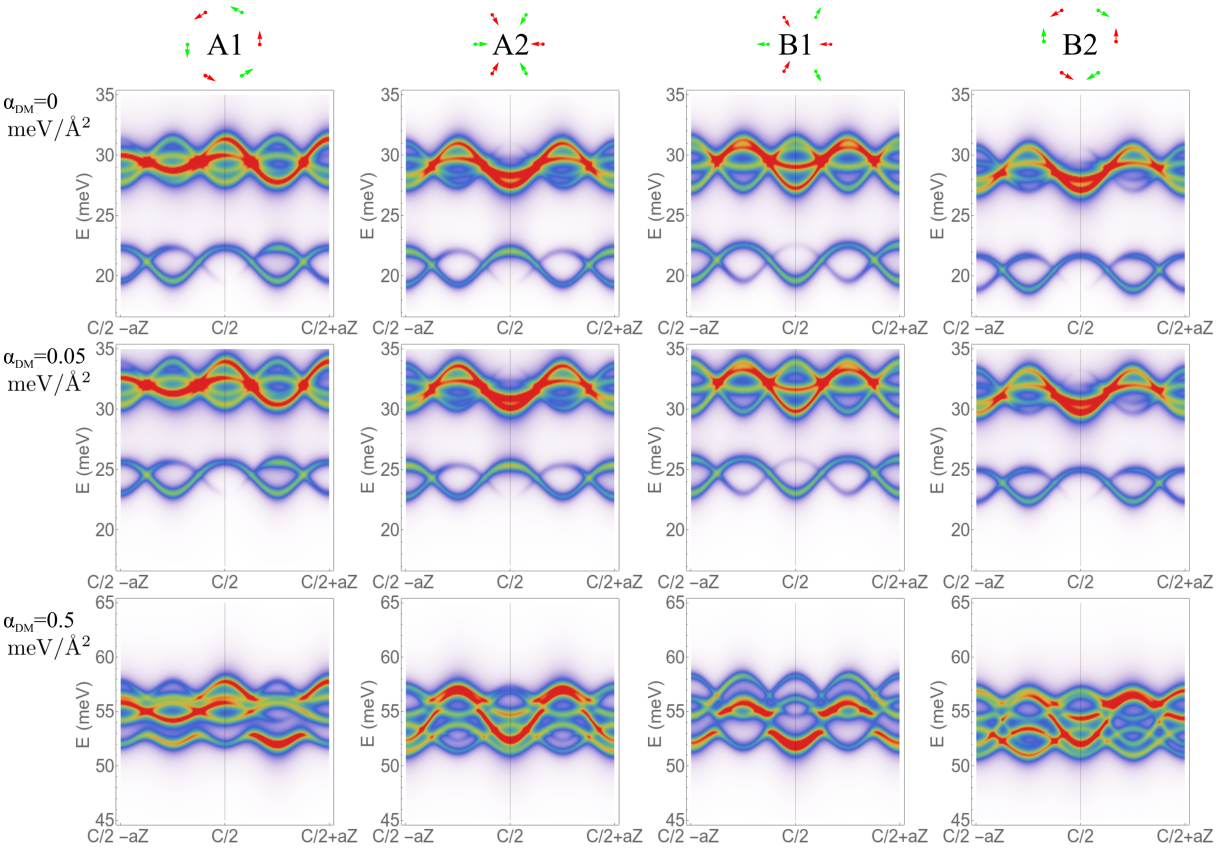

Figure 1.10: INS cross-section plotted near a midpoint of C-Γ interval along k_z for different magnetic phases and for different values of DM interaction. Color scale encodes the INS intensity.

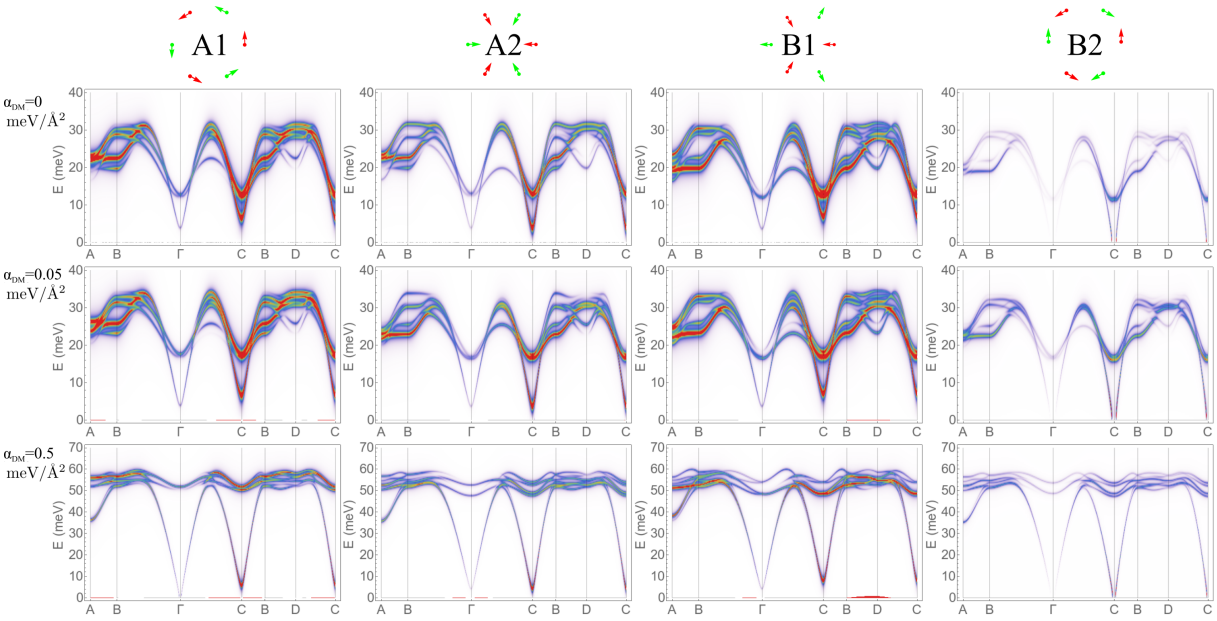

Figure 1.11: Simulated INS spectra along the path shown in Fig. 1.8 for different magnetic phases and different values of DM interaction. "aZ" refers to a small deviation from C/2 along k_z direction. Color scale encodes the INS intensity.

Chapter 2

Study of excitations in spin spiral systems

2.1 Introduction

In the previous Chapter we discussed a layered system in which geometrically frustrated magnetic interactions gave rise to monopolar and toroidal orders. In this Chapter we are going to discuss another frustrated system. However, in this case, the frustration is not caused by the geometry but from the competition between nearest and next nearest neighbor exchange interactions, as often encountered in orthorhombic manganites, e.g. $TbMnO_3$. In this case magnetic frustration often results in a configuration where the spins all rotate along the same angle with respect to each other, forming a spin spiral. We focus our attention to the interesting physical properties that arise in a spin spiral, for example the inversion symmetry breaking due to the presence of the spiral induces a ferroelectric polarization [1]. This feature alone opens a wide range of possibilities for multiferroic phenomena. The interaction between magnetic and electric degrees of freedom is a topic of major interest in the field of condensed matter physics as it paves the way for the technological development in controlling magnetic order and magnetic excitations through electric fields [18, 19].

In this Chapter we start with the simplest model for a spiral: a one-dimensional spin chain with competing nearest neighbor (NN) and next nearest neighbor (NNN) interactions. We then discuss the presence of domain walls (DWs) in the spiral. We can describe a DW as the boundary between two regions of the system for which the spirals exhibit different spin rotation sense. DWs are spontaneously formed inside a material during a phase transition.

The spiral configuration, in conjunction with the presence of the DW, sets the proper conditions for the emergence of interesting and non trivial modes inside the material. Among these modes, soft and polar modes are found and they potentially contribute to the dielectric properties of the material. Such modes can affect the system as a whole or can be active only in the single domains or locally on the DW. Our analysis is concentrated on the particular class of chiral DWs. In general we define a system as chiral (from the Greek for *hand*) if it presents two different configurations that are mirror images of each other and are energetically inequivalent. In the case of a spin spiral, a spiral is chiral if one rotation sense of the spins is preferred over the other. A chiral domain is then a region identified by a well defined spin rotation sense; a chiral DW separates two opposite chiral domains. DM interaction, described also in the previous Chapter, favors a rotation sense

for the spin, and thus is a chiral interaction. Furthermore DM interaction relates the rotation sense of the spin to electric polarization, hence chiral DWs are also ferroelectric.

The structure of this Chapter is the following: in the first sections we describe the spiral Ansatz and the compatibility of this configuration with the presence of DWs. We then generalize the case by introducing a quasi 1-D model Hamiltonian. This model includes DM interaction, anisotropy terms and external field terms. With this choice the model may be used to describe real materials that exhibit spiral order, such as $TbMnO_3$ and $MnWO_4$. The Hamiltonian is studied for the particular case of a spiral with a single chiral DW. By analysing the excitation spectrum we infer magnetoelectric properties of the spiral magnet [20]. Among the full set of modes we identify a number of low frequency dielectric anomalies that may be the primary cause of hybrid magnon-polar phonon excitations.

The Chapter concludes with a discussion on how the presence of a DW alters the phonon and magnon spectra. A separate section is dedicated to the ME properties of the spiral and the dynamics of the spin texture.

2.2 The spiral configuration

The causes for the emergence of a non collinear spin structure inside a material are numerous and quite diverse. It is not possible to write an extensive list for such causes at this level, but significant examples are the following:

- frustrated spin interactions (e.g. DM interactions or competing Heisenberg exchanges);
- geometric constraints bound to the symmetries of the material (as the geometric frustration of the previous Chapter, AFM interaction on triangles);
- non linear effects and high order terms absent in low energy effective theories (4-spins interactions [21, 22]);
- interplay between electric and magnetic degrees of freedom in the material (e.g. DM interaction favors non-collinear states [23]).

In this section the attention is focused on a rather simple spin configuration, a quasi-1D spin spiral. We study this case in order to better understand the generalized model that we will introduce in the next section and that can be use to study real material that exhibit the spiral order ($TbMnO_3$, YMn_2O_5, $MnWO_4$, CuO [24, 25, 26, 13])

We now describe how a spiral arises as a ground state of a simple interacting spin Hamiltonian where magnetic frustration is present in the form of competing NN and NNN interactions. The Hamiltonian is

$$H = \sum_i J_1 \mathbf{S}_i \cdot \mathbf{S}_{i+1} + J_2 \mathbf{S}_i \cdot \mathbf{S}_{i+2}, \tag{2.1}$$

here we consider $J_1 < 0$ and $J_2 > 0$ as respectively the NN and NNN Heisenber exchange constants, while $\mathbf{S}_i$ describes the spin at site i of the chain. We will refer to this Hamiltonian as the J_1-J_2 model. We are looking for a solution that describes a spiral in a plane, therefore we consider the vectors $\mathbf{S}$ as 2D vectors of unitary length. In polar coordinates

$$\mathbf{S}_i = \{\cos\phi_i\,, \sin\phi_i\}, \tag{2.2}$$

with this choice of coordinates the scalar product is

$$\mathbf{S}_i \cdot \mathbf{S}_j = \cos(\phi_i - \phi_j). \tag{2.3}$$

We can obtain a spiral solution with the following ansatz: we assume that the spin angle follows the relation $\phi_n = n\phi_0$, where we determine the value of ϕ_0 through minimization. This choice is also motivated by the translational invariance of the Hamiltonian, we then expect all the spins to rotate the same amount. It follows that Eq. (2.1) becomes

$$H = N(J_1 \cos\phi_0 + J_2 \cos 2\phi_0) \tag{2.4}$$

where N is the number of spins in the chain. By minimizing the energy with respect to ϕ_0 we obtain

$$-J_1 + \sin\phi_0 - 2J_2 \sin 2\phi_0 = 0, \tag{2.5}$$

and, simplifying for $\sin 2x = 2\sin x \cos x$, we have

$$\cos\phi_0 = -\frac{J_1}{4J_2}, \tag{2.6}$$

which gives the expression for the angle ϕ_0 in terms of the parameters of the model

$$\phi_0 = \arccos\left(-\frac{J_1}{4J_2}\right). \tag{2.7}$$

This expression gives the value of the fundamental angle of the spiral, but also sets the condition for the spiral solution to appear. For the spiral to exist, the condition $|J_1/4J_2| < 1$ must be verified. This condition imposes constraints on J_1 and J_2 for the spiral to appear, otherwise the system would stabilize in a FM or AFM pattern. We obtained the angle for the spiral solution, but the rotation verse of the spins is not fixed, the spins can rotate either of ϕ or $-\phi$. This happens because the J_1-J_2 does not define a preferred chirality. If, for example, we introduce a DM term, a preferred rotation sense of the spins will be selected.

Another important detail is that J_1 and J_2 depend on the material and, in general, Eq. (2.7) does not result in a rational fraction of π. Therefore the spins will never complete a full rotation in correspondence of a site, i.e. there is no integer number n such that $n\phi_0 = 2\pi$. We define this scenario as *incommensurate* magnetic order.

2.2.1 Chiral Domain and Domain Walls

In the previous section we obtained the spiral as a solution of J_1-J_2. We expect for a material with frustrated magnetic interactions to have a spin spiral configuration as a ground state, but the situation in real materials is more complex.

We refer to spiral order we just described as the "perfect spiral". In real materials that exhibit spiral order, the spin configuration may differ significantly from the perfect spiral.

The first trivial deviation from the perfect spiral is due to the higher dimensionality of real systems. In a 3D material spins can rotate along the three major directions defined by the lattice vectors. This is not a problem for our case because we are considering materials that shows a modulated magnetic order along only one of the lattice directions (e.g. $TbMnO_3$) and for which a quasi-1D model can be used. We call our model a "quasi-1D" model because we are considering a 1D chain where the spins can move in a plane.

In the spiral state, the spins rotate along the direction of the wave vector $\mathbf{q}$ of the spiral, and they do not rotate along the directions perpendicular to $\mathbf{q}$. Therefore, we can select $\mathbf{q}$ as the direction of our x axis, and describe the spiral state with only one coordinate. For example, let us consider a slightly more complex case: a 2D square lattice with competing J_1-J_2 interactions along the two axes. The periodicity of the system allows for a Fourier analysis, and so we can express the Hamiltonian in Fourier space as

$$H_{\mathbf{q}} = J_1(\cos q_x + \cos q_y) + J_2(\cos 2q_x + \cos 2q_y), \tag{2.8}$$

which is minimized for a certain direction of the vector $\mathbf{q} = q_x, q_y$, with $q_x = q_y$. We define a coordinate system such that $\mathbf{x} \parallel \mathbf{q}$. In this way a 2D spiral configuration is described with a quasi-1D model. Another reason for the system to not have a perfect spiral order is the presence of impurities and defects. In the vicinity of an impurity or a defect, the effective interactions between the spins may be different, thus altering the local spin order in that region.

Finally, the temperature also plays a fundamental role. If a material displays spiral order at low temperature, the system needs to be cooled down to reach the spiral state. The cooling rate across the transition controls the number of chiral domains: a rapid quenching of the temperature leads to higher DW density while a slower cooling allows the coalescence of chiral domains and the DWs to be removed.

Due to these effects is not uncommon for the ground state of a real material to be driven away from the perfect spiral we described. On the contrary, a more "fragmented" spiral order is reached. Fig. 2.1 shows two different spin configurations: the regular spiral (a) with the angle ϕ_0 that we obtained in Eq. (2.7) and a "fragmented" spiral (b). In the first all the spins rotate in the same sense around the spiral axis (perpendicular to the plane of the page) while in the latter the spiral changes rotation sense multiple times.

We mentioned in the introduction of this Chapter the concept of *chirality*, Fig. 2.1 provides an example of a pefect spiral (a) and a spiral with chiral domains (b). Two domains of opposite chirality are regions of the spiral where the spin rotate of the same angle but in the opposite sense. Fig. 2.1 (b) shows the rotation angle of the spiral to be either ϕ_0 or $-\phi_0$. The region of separations between two chiral domains is a chiral DW. We see from our Hamiltonian 2.4, that both angles ϕ_0 and $-\phi_0$ are minima of the same energy, thus in a material without preferred chirality the two rotation senses are equivalent.

In the beginning of this section we stated that the perfect spiral is altered in real materials. A more realistic configuration is, in fact, a multi-domain spiral. We can justify this configuration over the perfect spiral with the following argument: we consider a material that possesses two possible phases, a spiral phase and a non-spiral phase. We do not explore the details of the phase transition but we suppose that it can be properly described in terms of a certain control parameter A. The phase transition happens at a certain value A_0 of the parameter. The material is in the non spiral phase and $A \neq A_0$, as A gets close to the value A_0 small ordered spiral domains start to appear in random places in the material. As A approaches A_0 these domains grow, nucleating into bigger domains. We showed that the possible spiral angles ϕ_0 and $-\phi_0$ are energetically equivalent so in different domains the value of this angle is randomly chosen between the two possibilities. When two domains that have different spiral angles merge the boundary region that connects the two forms a DW. As the phase transition happens the material enters the spiral phase and all domains merge. where the spiral angles are different DWs appear inside the material.

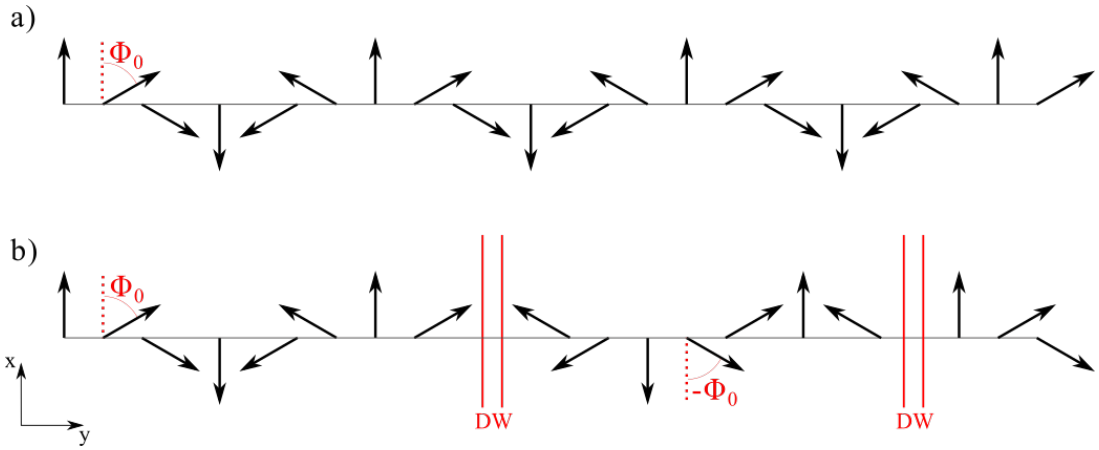

Figure 2.1: (a) "perfect spiral" solution. All spins rotate around the spiral axis ($\hat{z}$ perpendicular to the page) with the same angle ϕ_0. (b) multiple chiral domains and DWs. Different regions with spin angles ϕ_0 and $-\phi_0$ are present and are connected through their boundaries with chiral DWs.

In the next section we introduce the model suited to study a spiral configuration in presence of a DW, and we use it to analyze the multi-domain configuration that we discussed.

2.3 The model

In section 2.2 we showed how a simple J_1-J_2 model results in a spiral arrangement of spins and later we discussed how DWs arise in the spiral. In this section we build a more realistic microscopic model. We generalize a J_1-J_2 model by introducing additional terms describing polar displacements of oxygen ions (e.g. in $TbMnO_3$) that change the angle of Mn-O-Mn bonds. Therefore, we write the Hamiltonian

$$\begin{aligned} H = \sum_i & J_1 \mathbf{S}_i \cdot \mathbf{S}_{i+1} + J_2 \mathbf{S}_i \cdot \mathbf{S}_{i+2} + K_h (S_i^z)^2 + \alpha_{\mathrm{DM}} (\mathbf{r}_{12} \times \delta\mathbf{r}_i) \cdot (\mathbf{S}_i \times \mathbf{S}_{i+1}) \\ & + \frac{1}{2m} \boldsymbol{\pi}_i^2 - V_{uc} \mathbf{P}_i \cdot \mathbf{E} + \frac{m\bar{\omega}^2}{2} \delta\mathbf{r}_i^2 + \frac{\gamma}{2} (\delta\mathbf{r}_{i+1} - \delta\mathbf{r}_i)^2, \end{aligned} \tag{2.9}$$

where $\mathbf{S}_i$ is the classical spin ($|\mathbf{S}| = 1$) at site i, and J_1 and J_2 represent competing Heisenberg interactions, as described in Section 2.2. K_h is the strength of a hard $c-$axis anisotropy that forces the spins into a the ab plane as observed e.g. for $TbMnO_3$ [24]. The term with α_{DM} describes the DM interaction and is responsible for the coupling between spins and electric dipoles. $\mathbf{P}_i = Z\delta\mathbf{r}_i$ is the polarization due to the polar mode (electric dipole per unit cell volume V_{uc}), directly related to the shift $\delta\mathbf{r}_i$ of oxygen and Mn ions in the unit cell i. Z is the mode effective charge. When in the following we refer to oxygen shifts we will consider $TbMnO_3$ as a reference.

The DM term is responsible for an effective force on the polar mode $\delta\mathbf{r}_i$

$$\boldsymbol{F}_i^{\mathrm{DM}} = -\partial H / \partial \delta\boldsymbol{r}_i \sim [\boldsymbol{S}_i \times \boldsymbol{S}_{i+1}]. \tag{2.10}$$

This force results in a finite shift $\delta\mathbf{r}_i$, and generates a ferroelectric polarization. In particular, the sign of the polarization is determined by the product $[\boldsymbol{S}_i \times \boldsymbol{S}_{i+1}]$, which is

positive or negative depending on the spin rotation sense, i.e. the chirality of the spiral. Therefore chiral DWs are ferroelectric. $\mathbf{E}$ is the external electric field. The term with $\boldsymbol{\pi}_i$ is the kinetic energy associated with the momentum of oxygen ions, $\boldsymbol{\pi}_i = \{\pi_i^x, \pi_i^y, \pi_i^z\}$ and $\delta\mathbf{r}_i = \{\delta x_i, \delta y_i, \delta z_i\}$ are in fact canonical variables and and $\bar{\omega}$ is the frequency of the polar optical mode [27], γ is the stiffness of the polar mode. Finally, m is the mode effective mass divided by the square of the mode effective charge Z.

Although more complex than the simple J_1-J_2 model, the solution for this Hamiltonian is still a spiral, as described in more detail in the next Section. However, we will first explain the physics behind the extra terms. The term with K_h is the hard c-axis anisotropy. As we are considering $TbMnO_3$ as an example, in order to capture its ground state we need the spiral to be confined in the ab plane of the crystal. This is achieved with the anisotropy term, introducing an energy penalty on the z components of spins. This forces the ground state spiral to be contained in the ab plane.

The DM term is introduced to describe the ME effect in the system. Other common sources of ME effect, such as Heisenberg exchange striction, are not considered here. The spin texture is coupled to oxygen shifts $\delta\mathbf{r}_i$. In fact, as the magnetic ions interact and the spin arrange themselves into the spiral pattern, polar distortions are induced in the lattice [27, 28, 29]. By coupling the magnetic (spins) and electric (oxygen shifts) degrees of freedom, the DM term introduces the ME effect into the model.

The harmonic oscillator term defines the oscillation frequency of the polar modes at $\bar{\omega}$, confining the oscillations of $\delta\mathbf{r}_i$ into a parabolic potential. The stiffness term, described by the parameter γ, introduces an energy penalty for spatial changes of polarization. It also couples oscillations at different unit cells that would otherwise be only weakly affected by each other through the DM term.

2.4 Solution and properties

In Section 2.2 we were able to find analytically a ground state of the Hamiltonian, Eq. (2.1), by imposing a simple spiral ansatz. However the general model that we introduced in the previous section with Eq. (2.9) is more complex and spins are not constrained to the plane

$$\mathbf{S}_i = \{\sin\theta_i \cos\phi_i, \sin\theta_i \sin\phi_i, \cos\theta_i\}. \tag{2.11}$$

It is less straightforward to analytically minimize Eq. (2.9). We are particularly interested in the local minima with DWs. In this regard we minimize the Hamiltonian (2.9) by numerical methods, and find a possible ground state for the system. Periodic boundary conditions are set on a chain of 50 spins and, in this phase, no external electric field is used. The values of the parameters used in the calculations are $J_1 = 0.3$ meV, $J_2 = 0.1$ meV, $V_{uc} = 230$ Å^2 (similar to those in $TbMnO_3$ [25, 24]), $\bar{\omega} = 21$ meV$= 5$ THz [30], $K_h = 0.1$ meV, $m \approx 3m_O/V_{uc}$ with m_O being the mass of oxygen, $\alpha_{\mathrm{DM}} = 1$ meV/Å^2, $c = 0.3$ meV/Å^2.

As we explained before, a physical system will likely have different chiral domains connected by DWs. Therefore we select proper initial conditions for the minimization process to obtain a ground state with a single DW in the middle of the chain.

Fig. 2.2 compares the ground state of the J_1-J_2 model, for which the spiral angle ϕ_0 is obtained from Eq. (2.7), and the ground state of the generalized model. The figure shows the dependence of the azimuthal angle of spins on the site number. We can compare the 2D solution from Eq. (2.1) with the 3D solution of the generalized model as we have

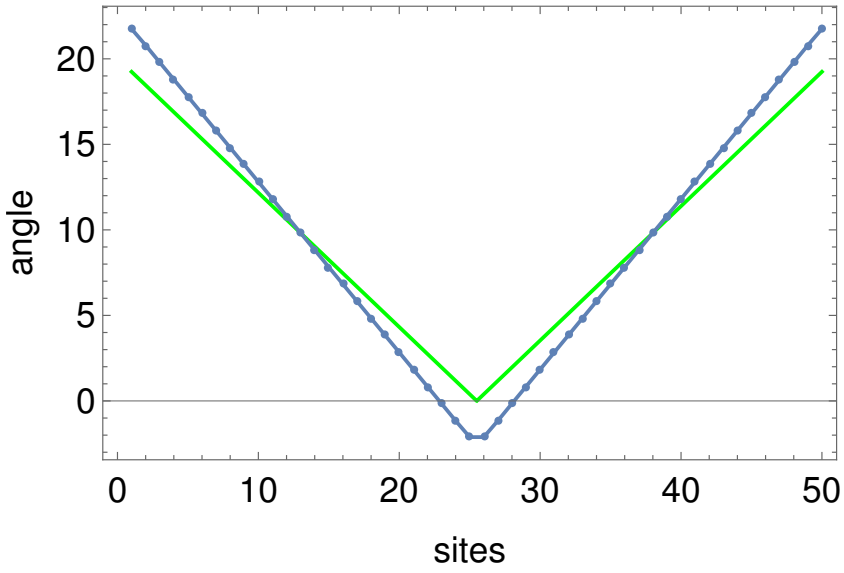

Figure 2.2: The profile of azimuthal angle of spins ϕ_n at site n along the chain in presence of a DW. (green) angle profile computed within the J_1-J_2 model from Section 2.2. (blue) ground state of the general Hamiltonian (2.9). The V-shape in the center indicates the reversal of spin rotation sense due to the presence of a DW. The solution of the general Hamiltonian has a different slope due to the additional terms introduced in the model. The angle is expressed in radians and is not reported in modulus 2π for a simpler visual comparison of the two solutions.

imposed the generalized spiral solution to lie in the ab plane through the anisotropy term in the Hamiltonian. The DM term couples the spins with the polarization, this causes the spiral pitch (rotation angle between the two adjacent spins) to be different from the J_1-J_2 case. The green curve corresponds to the spiral pitch $\pm\phi_0$ (cf. Eq. (2.7)). The change of the slope in the V-shaped fashion is due to the presence of a chiral DW in the center of the chain. The DW connects two different chiral domains with the opposite spin rotation. This results in an increase or decrease, respectively, of the azimuthal angle in the two domains.

We point out that the increase of the azimuthal angle in the generalized solution is close to a perfect linear behaviour. The slight misalignment in the figure is a numerical effect. Inside domains spins rotate by the same angle, as the Hamiltonian 2.9 is translationally invariant, and a constant pitch is expected along the chain.

2.4.1 Modelling magnetic and electric susceptibilities

After introducing the model and describing the ground state of the system, we are now ready to perform an analysis of magnetic and lattice excitations in the spin spiral state.

We will utilize a method akin to the one used in Chapter 1: we start from the minimum of the Hamiltonian and we perform a second order expansion around the ground state, then we solve the associated eigenproblem to get the excitations. We use a different method to compute the response functions (electric, magnetic and ME susceptibilities). To show how to compute the susceptibility, we first consider a simple case: an electric charge q oscillating with a frequency $\bar{\omega}$ around an equilibrium position ($x_0 = 0$). An

external electromagnetic wave with frequency Ω and electric field amplitude E is applied and interact with the charge. The motion happens along the x direction, aligned with the field,

$$m(\ddot{x} + \bar{\omega}^2 x) = qEe^{-i\Omega t}. \tag{2.12}$$

We Fourier transform the previous equation into

$$\int m(\ddot{x} + \bar{\omega}^2 x)e^{-i\omega t}dt = qE \int e^{i\Omega t}e^{-i\omega t}dt, \tag{2.13}$$

and, by integrating in t, we get

$$-\omega^2\tilde{x} + \bar{\omega}^2\tilde{x} = qE\delta(\Omega - \omega), \tag{2.14}$$

from which we obtain an expression of the Fourier transform of the displacement $\tilde{x}$ as a function of the driving frequency Ω and the Fourier frequency ω

$$\tilde{x}(\omega) = -\frac{qE\delta(\Omega - \omega)}{m(\omega^2 - \bar{\omega}^2)}. \tag{2.15}$$

In a crystal instead, the charges are arranged periodically and the electric polarization is defined as a density of electric dipoles. The dipole associated with the charge q is, in Fourier space, $\tilde{d} = q\tilde{x}$. It follows that the polarization $\tilde{P}$ in Fourier space is

$$P(\omega) = \frac{q\tilde{x}(\omega)}{V}, \tag{2.16}$$

with V being the unit cell volume. Finally we can compute the electric susceptibility,

$$\alpha^e(\omega) = \frac{dP(\omega)}{dE(\omega)} = \frac{1}{V}\frac{q\tilde{x}(\omega)}{E(\omega)} = \frac{q^2}{mV(\bar{\omega}^2 - \omega^2)}, \tag{2.17}$$

where $E(\omega) = E\delta(\Omega - \omega)$. To summarize, electric susceptibility is proportional to the oscillating component of the polarization, induced by the external field, $\alpha^{\mathrm{e}}(\omega) \propto \tilde{P}(\omega)$. in the following, we generalize this calculation to the case of the model we are studying. Despite the bigger complexity, the result still takes the form of a sum of Lorenzians, cf. Eq. (2.17), with the characteristic denominator, which for a static susceptibility $\alpha^e(\omega = 0)$ is proportional to $1/\bar{\omega}^2$. Similar consideration can be repeated for the magnetic susceptibility, proportional to the oscillating component of the magnetization, and with the ME susceptibility, that depends on both the magnetization and polarization components.

2.4.2 Susceptibility from eigenmodes

To compute the susceptibility from the Hamiltonian, Eq. (2.9), we proceed in a similar way as in Chapter 1. We start by identifying a local minimum of the Hamiltonian in the spiral configuration with a DW in the center. For brevity, we introduce a generalized variable $\boldsymbol{\xi}$, so that $\xi_i = (\theta_i, \phi_i, \boldsymbol{\pi}_i, \delta\boldsymbol{r}_i)$. We call $\boldsymbol{\xi}_0$ the values of variables in the ground state. We now introduce a small deviation $\tilde{\boldsymbol{\xi}}$ so that, close to the ground state, we obtain $\boldsymbol{\xi} = \boldsymbol{\xi}_0 + \tilde{\boldsymbol{\xi}}$. As in Chapter 1, by substituting this expression for $\boldsymbol{\xi}$ in H and taking derivatives up to the second order with respect to the different components of $\tilde{\boldsymbol{\xi}}$, we build a Hamiltonian matrix,

$$\mathcal{H} = \begin{pmatrix} \partial^2_{\phi\theta} & \partial^2_{\phi^2} & \partial^2_{\phi\pi} & \partial^2_{\phi\delta r} \\ -\partial^2_{\theta^2} & -\partial^2_{\theta\phi} & -\partial^2_{\theta\pi} & -\partial^2_{\theta\delta r} \\ -\partial^2_{\delta r\theta} & -\partial^2_{\delta r\phi} & -\partial^2_{\delta r\pi} & -\partial^2_{\delta r^2} \\ \partial^2_{\pi\theta} & \partial^2_{\pi\phi} & \partial^2_{\pi^2} & \partial^2_{\pi\delta r} \end{pmatrix} H, \tag{2.18}$$

from which it is possible to obtain the equations of motion for all the variables in a harmonic approximation. ∂^2_{xy} means that we are considering partial second order derivatives in the variables x and y. We omit the $\sim$ for simplicity of notation. The minus sign is due to the relation of conjugation between the two couples of canonic variables, $(\delta\boldsymbol{r}, \boldsymbol{\pi}), (\theta, \phi)$, while the the form of the matrix is chosen so that the Hamilton equations can be rewritten in the compact form:

$$\dot{\boldsymbol{\xi}} = \mathcal{H}\boldsymbol{\xi}, \tag{2.19}$$

where here $\boldsymbol{\xi}$ absorbs the $\sin\theta_i$ terms that would be required as in Eq. (1.7). In Fourier space, we obtain an equivalent to an eigenvalue problem

$$\mathcal{H}\boldsymbol{\xi} = i\omega\boldsymbol{\xi}. \tag{2.20}$$

As stated in the previous section, we need the Fourier transform of polarization and magnetization to compute the susceptibilities of the system. In Section 2.2 we discussed how the spiral periodicity is in general incommensurate with the lattice. The absence of an exact periodicity makes difficult the use of an analytical Fourier transform. To obtain the quantities needed for the computation of susceptibilities, we compute eigenvectors and eigenvalues of $\mathcal{H}$ in real space. In order to obtain the polarization in Fourier space we perform a discrete Fourier transform on the components of $\boldsymbol{\xi}$, that are related to the electric polarization

$$\mathbf{P}(k,\omega) = \sum_{n}^{N-1} Z\delta\mathbf{r}_n(\omega)e^{i\frac{2\pi}{N}k\,n}, \tag{2.21}$$

where N is the total number of spins in the chain. Note that $\delta\mathbf{r}$ is a function of ω, because $\boldsymbol{\xi}$ is a solution of Eq. (2.20).

In order to obtain the Fourier transform of the magnetization we first expand it to the first order in the components $\tilde{\theta}$ and $\tilde{\phi}$ of $\boldsymbol{\xi}$ around the ground state:

$$\mathbf{M}_i = g\mu_B\left(\mathbf{S}(\theta_{i0},\phi_{i0}) + \frac{d\mathbf{S}(\theta_{i0},\phi_{i0})}{d\theta_i}\tilde{\theta}_i + \frac{d\mathbf{S}(\theta_{i0},\phi_{i0})}{d\phi_i}\tilde{\phi}_i\right), \tag{2.22}$$

where $\mathbf{M}_i$, θ_i and ϕ_i are all functions of ω. The discrete Fourier transform of the magnetization is then

$$\mathbf{M}(k,\omega) = \sum_{n}^{N-1} \mathbf{M}_n(\omega)e^{i\frac{2\pi}{N}k\,n}. \tag{2.23}$$

In the previous section we showed that, in Fourier space, the electric susceptibility is proportional to the oscillating component of the polarization. A similar argument can be made for the magnetic susceptibility. Fig. 2.3 shows the electric and magnetic susceptibilities computed from Equations (2.21) and (2.23). It is possible to see the effects of ME coupling by looking at the different components of the electric and magnetic susceptibilities. There is a close resemblance between components α^m_{11} (or α^m_{22}) magnetic susceptibility with component α^e_{33} of the electric one. This is due to the particular shape of the DM interaction, which couples only perpendicular components of magnetization and polarization. For the same reason, α^{e}_{11} resembles α^{m}_{33}. Instead, α^{e}_{22} only has one single mode and does not resemble any other component of the susceptibility. This is due to the vector $\mathbf{r}_{12}$ in the DM term being parallel to the b axis. There is no coupling with the polarization along that direction hence the associated components of the susceptibility are zero.

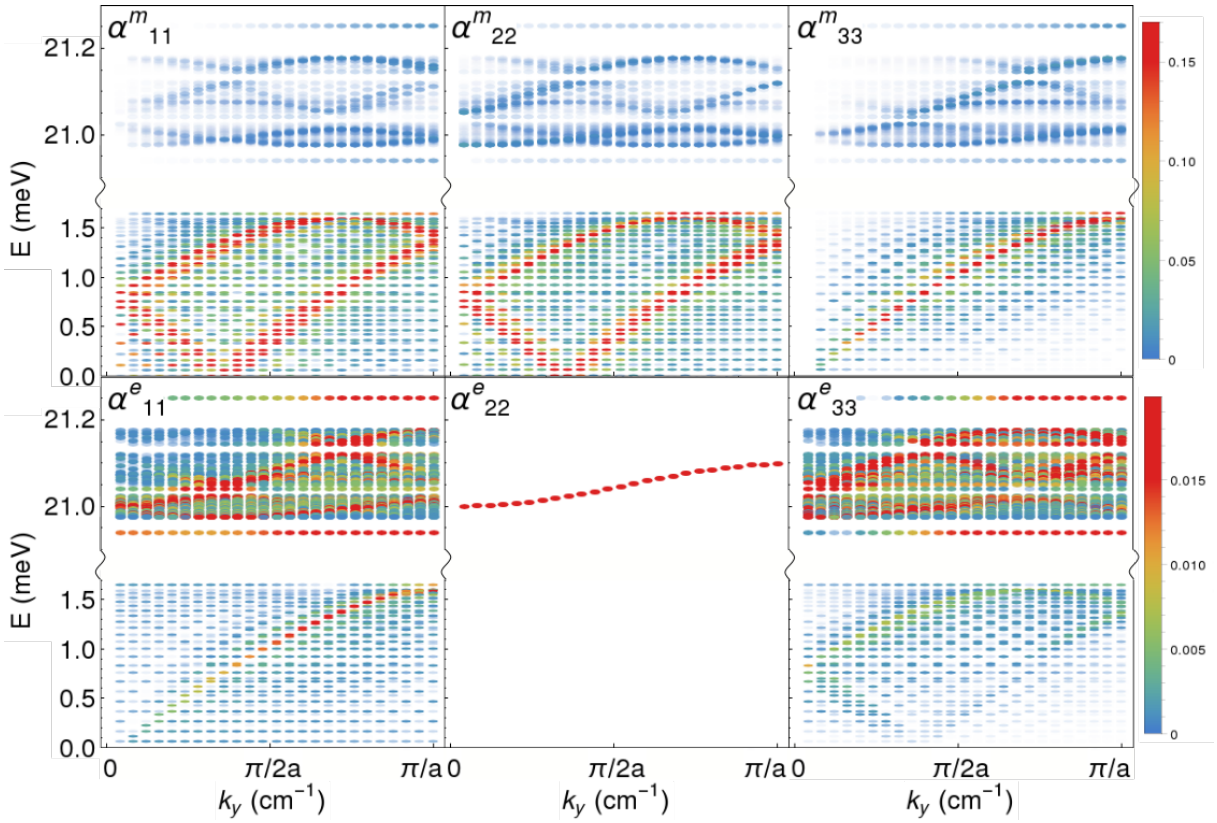

Figure 2.3: Diagonal components of magnetic (top row) and electric (bottom row) susceptibility tensors, computed in a spiral state with a DW. Colorscale encodes the intensity of the signal in arbitrary units. An energy cut is made in the graphs between 1.6 and 20 meV as there are no excitations in that range. Excitations below the energy cut originate from acoustic magnons while the excitations above are related to polar modes. Similarities between components 11, 22 of magnetic (electric) susceptibility and component 33 of electric (magnetic) susceptibility are present and are due to the ME coupling in the form of DM interaction.

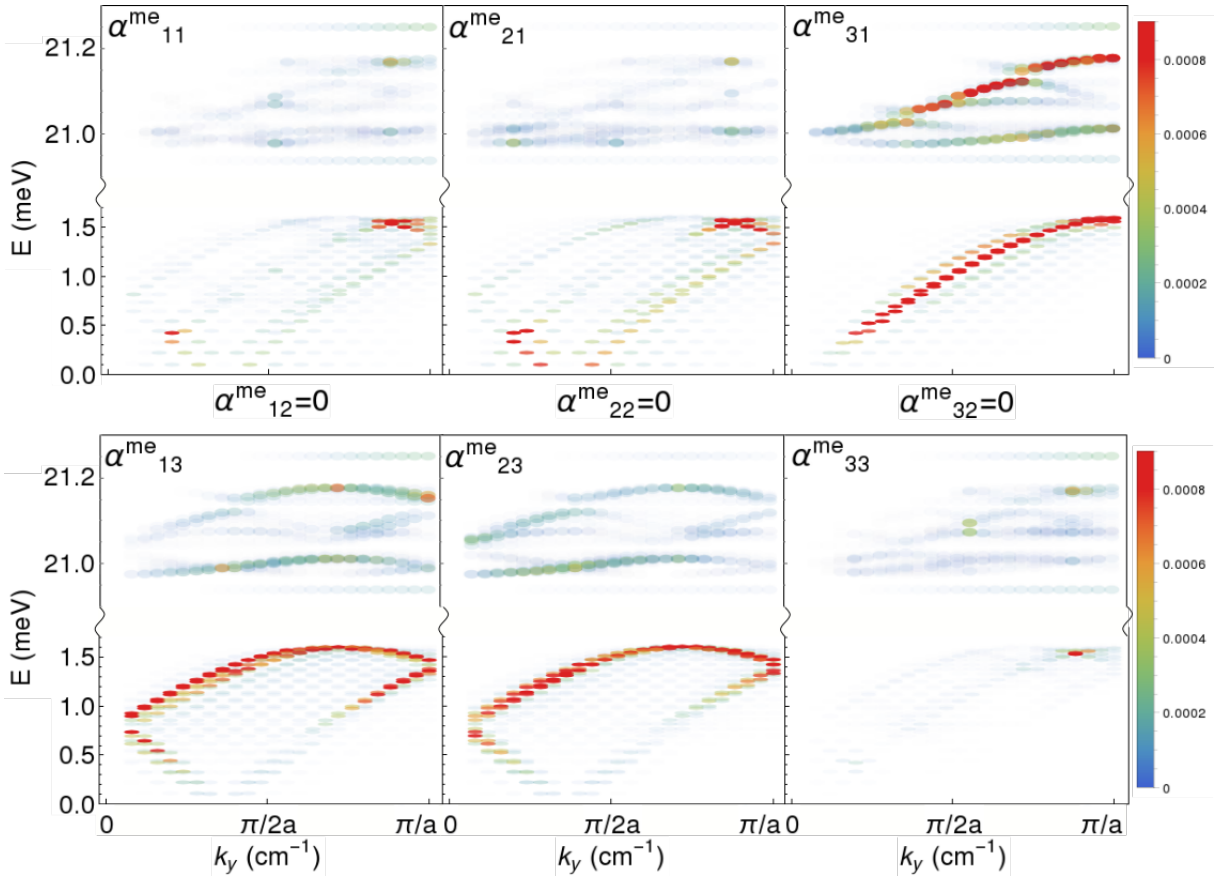

Figure 2.4: Magneto electric susceptibility computed with Eq. (2.24). Colorscale encodes the intensity of the signal in arbitrary units. All components α^{me}_{i2} are zero due to the particular shape of ME coupling, discussed in the text.

We can distinguish in the susceptibilities two kinds of excitations: low energy ones which are more intense in the magnetic susceptibility, and high energy ones which are more intense in the electric susceptibility. Low energy modes are "acoustic" magnetic modes while high energy ones are "optic" polar modes. The fact that they are present in both magnetic and electric susceptibility is again due to the ME coupling.

We can compute the resonant part of the ME susceptibility α^{me} from the magnetization $\tilde{M}$ and polarization $\tilde{P}$ of every mode. It is possible to show that, with spin and polar mode damping neglected, the $\alpha^{\text{me}}(\omega, q)$ is related to the magnetization and polarization profiles of the mode, or more precisely, to their Fourier components at the wave vector of the external probe field, $\tilde{M}(\omega, k)$ and $\tilde{P}(\omega, k)$, as the product of the two

$$|\alpha^{\text{me}}(\omega, k)| \propto |\tilde{M}(\omega, k)\tilde{P}^*(\omega, k)|, \tag{2.24}$$

Fig. 2.4 reports the ME susceptibility, where all the terms $\alpha^{\text{me}}_{i,2}$ are zero due to the peculiar ground state we are analyzing. The spiral is confined into the ab plane and the wave vector k being parallel to $\hat{y}$ causes the spin deviations to not couple to the polarization P_y through the DM term. Thus the term $\mathbf{r}_{12} \times \delta\mathbf{r}_i$ has $\mathbf{r}_{12} \| \hat{y}$, which enforces the shifts $\delta\mathbf{r}_i$ to be bounded into the ab plane. It follows that DM interaction couples the spin deviations only to the polarization in the spiral plane, thus leading to zero $\alpha^{\text{me}}_{i,2}$ terms of the ME susceptibility.

2.5 Role of the domain wall

Throughout the course of the present chapter we described how a spiral solution arises from the generalized Hamiltonian, Eq. (2.9), and how to extract information about the electric and magnetic responses through the calculation of susceptibilities. We also mentioned that the solution that we studied, as well as the real material that we are modelling, is characterized by the presence of chiral domains and the DWs between them. In this section we are going to describe in detail the effect of a DW on the dynamics of the excitations in the material. With the presence of a DW, new sliding and twisting modes are possible in the spectrum. As the DW is not pinned, this results in low frequency modes. The presence of DW broadens magnons that, in a pure cycloidal configuration, would be sharp. A coupling between DW-localized modes, and the bulk ones, potentially allows for the access and manipulation of these otherwise unreachable modes.

The presence of DW-localized modes is a crucial feature of the system we are studying. The DW acts as a barrier and as region of separation between two chiral domains. When a perturbation of any kind (i.e. thermal fluctuations, external fields, excitations...) acts on the domains and changes their shape or volume, there are repercussions on the DW.

This kind of phenomena is described through DW-related modes. For example, if one domain grows in size while the adjacent one shrinks, the DW wall between them will move, which is described by a DW sliding mode. Another possible DW-localized mode is a DW breathing mode, that represents the oscillations of the DW width. Other less intuitive DW-related modes exist. For example, an excitation of a breathing mode of a head-to-head wall will be accompanied by surface charge oscillations at the wall. In an analogous manner, magnons can interact with the wall, scattering off it, pushing or twisting the wall.

With these premises is it possible to realize the importance of a ME coupling for the DW-related modes. As discussed in Section 2.3, the DM interaction induces a ME coupling of magnetic and electric degrees of freedom (spins and polarization). The immediate consequence of this coupling is the mixing between polar modes and magnons and the possibility to dynamically control e.g. magnetic excitations with electric fields or vice versa.

We are interested in magnons that can be excited with the electric field, which we refer to as electromagnons [20]. In particular, an electromagnon is a hybrid magnon-phonon excitation that can be excited with a long-wavelength electric field (e.g electric field of light or of an oscillating electric dipole). Fig. 2.5 gives an example of a high-energy hybrid magnon-phonon mode. This particular mode is not localized at the wall. Nevertheless, the spin and polarization textures at the DW enter the equations of motion for magnons, and create a potential that may scatter magnons and preclude their propagation from one domain to another. This could be consistent with the mode amplitude in Fig. 2.5 having a node at the DW. In fact, in this particular mode the oscillations of spins and electric dipoles near the wall are diminished.

Interesting DW-localized modes can be found at the lowest frequencies, as seen in Fig. 2.6. In particular, Fig. 2.6 (a,b) shows DW-localized modes with the polarization profile that are even with respect to the position of the wall. These modes mix with even bulk magnons. The overall action of these modes is that of a sliding of the DW. The peak results from subtracting the polarization profiles of two DWs, shifted with respect to each other by a small distance,

$$\delta P(x) \sim \tanh(x+\delta)/\lambda - \tanh x/\lambda. \tag{2.25}$$

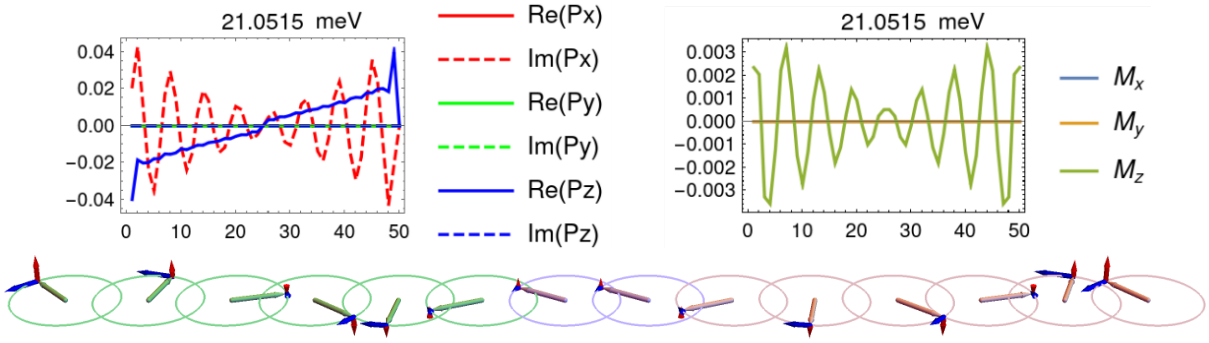

Figure 2.5: (Top row) Oscillating ferroelectric polarization profile (left) and spin deviations (right) for the excitation at E$\sim$ 21 meV. On the x axis is the site number and on the y axis the oscillation amplitude (a.u.). In this particular mode only Im[P_x] and Re[P_z] are non-zero while only M_z is non-zero in the magnon part. The resemblance of M_z to Im[P_x] is due to the DM interaction. (Bottom row) visual representation of the spin deviations induced by the mode. Green and orange arrows represent spins belonging to different chiral domains, while purple spins are at the DW. Red and blue arrows represent tilting of spins induced by the mode. Arrows are magnified for better visualization. The decrease of arrows near the wall shows that the mode does not affect the DW.

The DW wall is ferroelectric, thus the mode changes the electric polarization and is, in fact, an electromagnon. The bands of such low-energy hybridized modes are present in the lower part of the spectrum, seen in Fig. 2.3, and describe wall sliding at $k = 0$ and DW wobbling at $k \neq 0$. The magnons with an odd polarization, as seen in Fig. 2.6(c-d), are practically unaffected by the presence of the DW.

The interaction between DW-localized modes and bulk modes paves the way for possible DW-based technology. DWs could act as filters or gates for certain modes, blocking or allowing their propagation. Moreover, due to ME coupling, DW manipulation could help access otherwise unreachable bulk modes.

The frequencies of the modes may be overestimated, since DWs in our simulations were rather narrow, owing to a strong hard axis anisotropy. In $TbMnO_3$ and in general in other spiral magnets, the electromagnon is much softer. A soft electromagnon leads to a large contribution to the static dielectric constant of the material $\epsilon = 1 + 4\pi\alpha^{\mathrm{e}}$. In fact the electric susceptibility at zero frequency is, from Eq. (2.17),

$$\alpha^{\mathrm{e}}(0) = \frac{q^2}{mV\bar{\omega}^2}, \tag{2.26}$$

which is large for soft modes ($\bar{\omega} \to 0$). This is a possible explanation for the enhancement of the dielectric constant in MHz range in spin spiral systems [31, 32]. Domain walls have already been blamed for the dielectric constant enhancement in a proper ferroelectric: rhombohedral $BaTiO_3$, where it appears in the vicinity of the Bloch- to Ising-type DW phase transition [33], where a polar DW-localized phonon softens near such transition.

2.5.1 Effects of DWs on the excitation spectrum

The presence of a DW in the spin spiral order does not only introduce a different kinds of DW-related modes (i.e. DW sliding, breathing, tilting), but it also affects the shape of the magnon bands. The susceptibility of a single-domain spin spiral state only contains

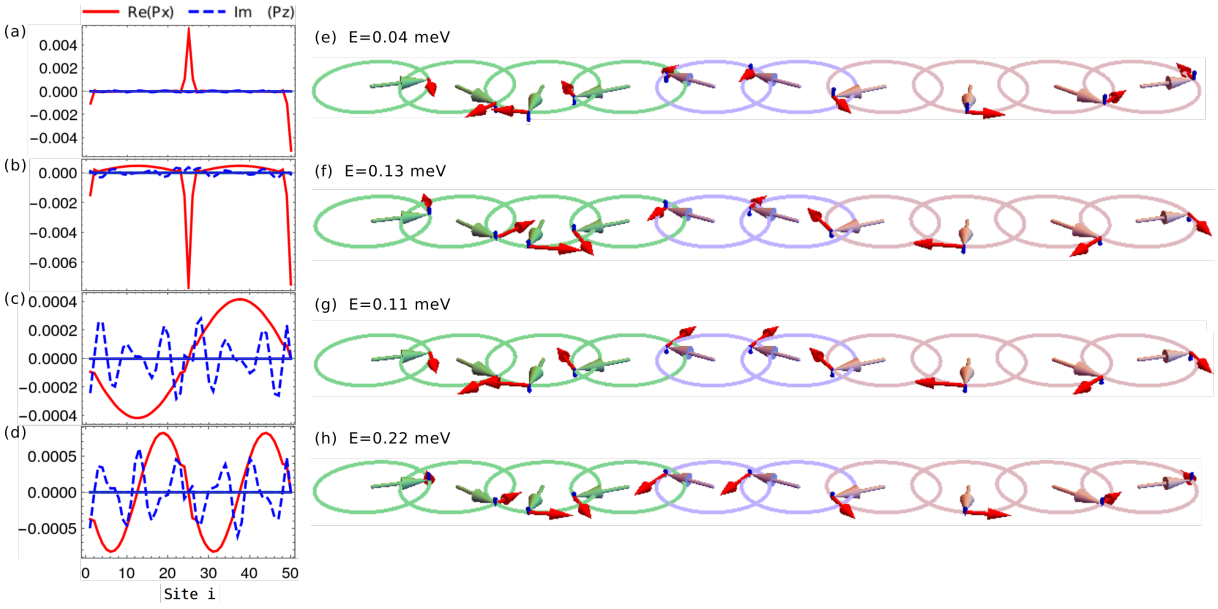

Figure 2.6: Soft modes, localized at the chiral DW. (a-b) Non-zero polarization components of the lowest-energy modes. These even modes are a mixture of DW sliding and bulk modes. Site number is reported on the horizontal axis and the polarization profile of the modes in arbitrary units is on the vertical axis. (e-f) Spin deviations corresponding to the modes shown in (a-b). The energies of the modes are indicated by the labels. Spins in green and orange belong to domains of opposite chirality, while purple spins are localized at the wall. In-plane spin deviations are indicated by red arrows, tangent to the circles, and the (much smaller) perpendicular components are in blue. (c-d) DW-odd bulk modes with a node at the DW position. This symmetry causes the modes to not mix with the DW-localized modes (sliding and tilting). (g-h) are the corresponding spin deviation.

sharp bands, both for magnetic and electric excitations due to translational symmetry, as seen in Fig. 2.7 [34]. In contrast, Fig. 2.3, shows the spectrum of spiral state with a chiral DW. The magnon bands are broadened due to the scattering of the wall.

In Fig. 2.8 we report the electric susceptibility (α^{e}_{11}) of two spiral configurations, with and without the DW. The presence of the DW breaks the translational symmetry and broadens the bands, localizing the modes in one or another particular domain or, in the case of DW-localized modes, in the proximity of the DW. This broadening of the modes makes it easier to excite some of them. The broadening occurs for both acoustic (magnons) and optical (lattice) modes but its contribution is of greater importance in the acoustic part as the excitations of the wall are mostly low-energy ones. The consequent broadening of the polar modes is due to the DM interaction that mirrors for polar modes the broadening of the magnons.

2.6 Conclusions

This chapter has been devoted to the study and characterization of a most basic non-collinear spin configuration, the spin spiral. The importance of such a state is both due to the unique modes that a spin spiral configuration naturally hosts, and to the presence of DWs in the spiral. In particular, the presence of DWs enriches the spectrum with new modes, domain-confined or DW-localized modes. DM interactions tie the spin rotation

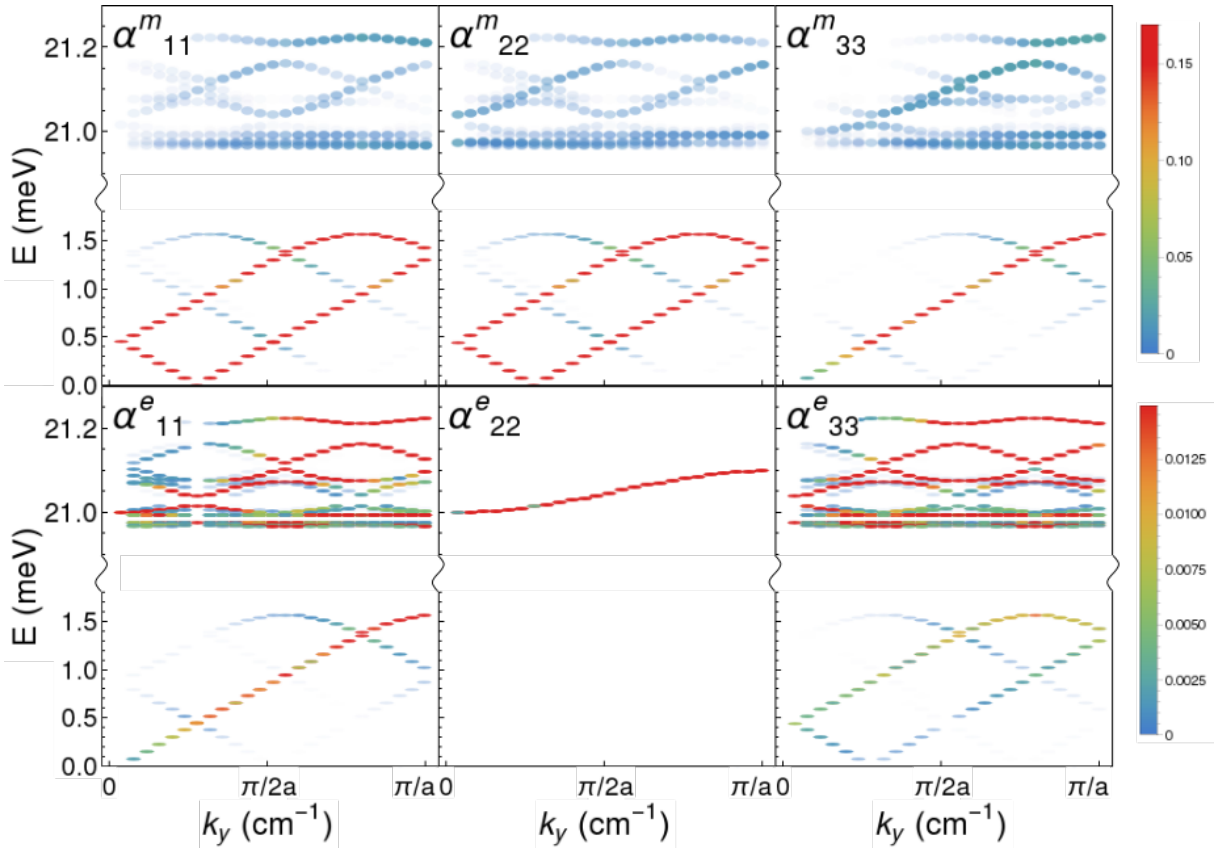

Figure 2.7: Magnetic (top) and electric (bottom) susceptibilities for a pure spiral. In absence of DW the excitation are delocalized along the whole spiral, resulting in sharp lines in the Fourier space. An energy cut along the y-axis is made due to absence of any modes in the removed region.

sense (spin chirality) to the ferroelectric polarization. Therefore chiral DWs in cycloidal spiral magnets are also ferroelectric.

The main findings of this chapter are in the description of hybrid magnons and phonon excitations that are mixed by the DM interactions. Particularly, a soft DW localized sliding mode is identified as an electromagnon. This suggests that the dielectric constant may be tuned via changing DW density, for instance, through poling. This could pave a way to the new types of tunable dielectrics. The interplay of magnetic and electric degrees of freedom, coupled with the presence of DWs, contributes to explain the presence of high-valued dielectric constants in real materials that host spin order akin to the spiral system we discussed. A study of the ME effect has been carried out. Unique modes related to the presence of the DW have been identified, that mix bulk modes with DW-localized ones, opening the way for the manipulation of bulk modes through DW interaction.

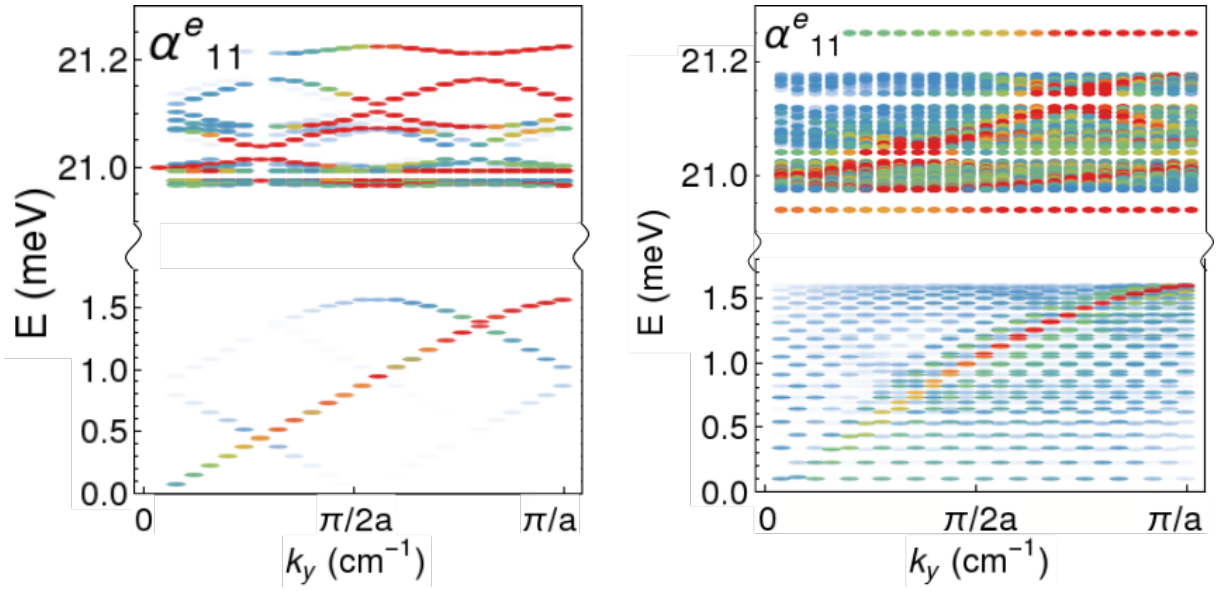

Figure 2.8: Comparison of electric susceptibility component α^e_{11} for (left) a single-domain spiral state and (right) a spiral state with a DW in the center. Both acoustic, primarily magnetic, and optical modes, lattice modes, are broadened due to the presence of the DW. An energy cut along the y-axis is made due to absence of any modes in the removed region.

Chapter 3

Magnetic excitations and skyrmion dynamics in GaS_4V_8

3.1 Introduction

In the previous Chapter we described the peculiar spiral order originating from frustrated exchanges. This Chapter makes use of a fairly general model, not too different from the models in chapters 1 or 2, but with all exchanges being ferromagnetic. Remarkably, as we will see, the Hamiltonian results in spiral and even skyrmionic lattice states at non-zero temperature. To simulate these states and their dynamics we make use of Monte-Carlo simulations in combination with the Landau-Lifshitz-Gilbert (LLG) dynamics, capturing the dynamics of the spin texture that characterizes the system. This allows for additional insights into thermal conductivity and photoexcited dynamics in the materials as described by this rather general model. This approach makes it possible to reproduce the experimentally measured thermal conductivity and transient magnetization oscillations seen in ultrafast optical experiments [35].

The material that we study in this Chapter is GaV_4S_8 (GVS), a multiferroic semiconductor of recent interest belonging to the lacunar spinel family that hosts a fascinating phase diagram. For different temperatures and external magnetic fields, cycloidal (Cyc), skyrmionic (SkL) and ferromagnetic phases are observed [36]. This rich phase diagram motivates the study of GVS because when a peculiar spin order is present the response of spin excitations to external perturbations (e.g. to photoexcitations, strains, and external electric and magnetic fields) is altered significantly. GVS, which can easily switch between different phases, provides a powerful test-case to study the general behaviour of excitations on the background of really diverse magnetic orders.

This Chapter is structured in the following way: we start by discussing the recent literature on GVS, describing the material and providing an explanation on how the phase diagram arises. We then focus on the recent experimental work of our collaborators (group of Paul H.M. van Loosdrecht, Univ. of Cologne), with particular attention on time-resolved magneto-optical Kerr effect (trMOKE) measurements on GVS. This will serve as a starting point for our theoretical description and simulations. Finally, we discuss the results of our simulations that address coherent collective modes and thermal conductivity, inferred from the magnetization recovery following transient photoexcitation. The aspects in which simulations agree with the experimental results are outlined, and the reasons behind the discrepancies are discussed.

3.2 The material

GaV_4S_8 (GVS) is a multiferroic semiconductor of the lacunar spinel family [37, 38]. It exhibits cubic non-centrosymmetric structure at room temperature 3.1, while at 42 K [39] a transition to a polar rhombohedral structure occurs. In comparison with the common spinel structure AB_2X_4, the fundamental unit of GaV_4S_8 has one Ga for every two positions, resulting in an alternating Ga not-Ga structure. This defect causes a non uniform distribution of the V_4 atoms that arrange in alternating larger and smaller tetrahedra [40]. The V_4 tetrahedra, that are arranged in a face-centered cubic lattice, are responsible for the magnetic properties of GVS as the molecular orbitals of V_4S_4 each host a spin-1/2. In this configuration a magnetic easy axis anisotropy is observed along the [111] direction [36, 41] of the cubic V_4 lattice. Along this direction a Jahn-Teller distortion is responsible for the transition from cubic to rhombohedral.

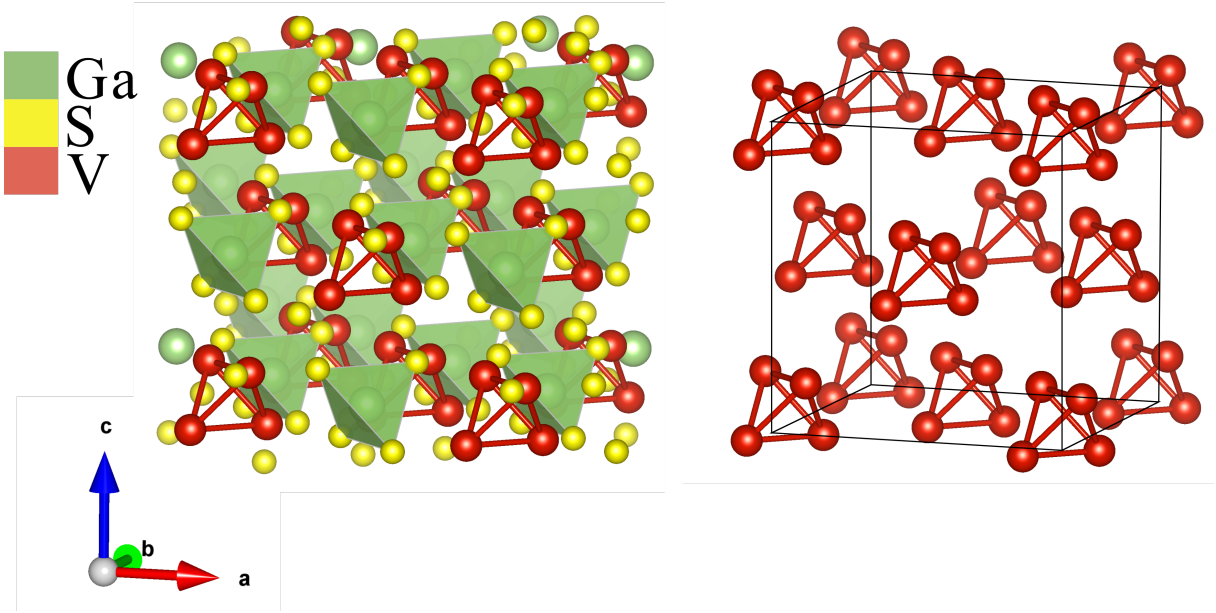

Figure 3.1: Cubic phase of GaV_4S_8. Comparative visualization of GVS structure (left) with the V_4 cubic lattice (right). Solid lines in the cubic in V_4 lattice are a guide for the eye.

In its rhombohedral phase GVS has been observed to have interesting magnetic properties. In fact, below the Curie temperature of 13 K [41], the phase diagram of GVS features a rich plethora of magnetic phases, as shown in Fig. 3.3. Below the Curie temperature the system displays either a ferromagnetic phase (FM), Néel-type skyrmion lattice phase (SkL) or a cycloidal phase (Cyc). In the Néel-type skyrmion, spins rotate around radial planes (Fig. 3.2) along the radial direction. It is possible to rationalize the appearance of different phases of the phase diagram in terms of general energy considerations. Let F be the free energy of the system,

$$F = E - T\mathcal{S}, \tag{3.1}$$

where E is the total energy, T the temperature and $\mathcal{S}$ the entropy of the system. The entropy contribution is null at $T = 0$ or negligible at low temperatures. The dominant interaction being the FM Heisenberg exchange $J\mathbf{S}_1 \cdot \mathbf{S}_2$, with $J < 0$, between nearest neighbor spins S_1 and S_2 results in a FM state. As the temperature is increased, the FM phase, where spins have maximal exchange field from the neighbors and thus form

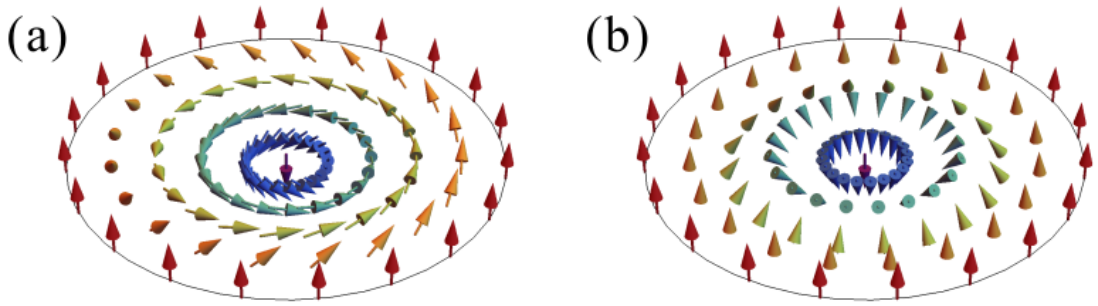

Figure 3.2: (a) Bloch type skyrmion: the spins rotate perpendicular to radial directions. (b) Neel type skyrmion: the spins rotate along the radial direction.

hard magnons, becomes less favorable compared to the spiral state, in which the canted neighboring spins produce lower exchange field. This is due to the free energy gain on the entropic term in non-collinear states like Cyc or SkL, where non-collinearity of the neighbors results in a lower effective field and hence softer magnons. To illustrate this statement, we consider a mean-field decoupling $J\boldsymbol{S}_1 \cdot \boldsymbol{S}_2 \to J\boldsymbol{S}_1 \cdot \langle \boldsymbol{S}_2 \rangle$, and compute the entropy of spin $\boldsymbol{S}_1$ in the effective magnetic field $\boldsymbol{H} = J\langle \boldsymbol{S}_2 \rangle$. This results in, up to a constant,

$$\mathcal{S} = \log\left[\frac{\sinh x}{x}\right] - x\coth x, \qquad x = \frac{HS_1}{T}. \tag{3.2}$$

Thus the entropy is a monotonically decreasing function of $S_1 H/T$. This reflects larger gain of the free energy on $-T\mathcal{S}$ term in a spiral phase with softer magnons, compared to the ferromagnetic phase with harder magnons. Eq. (3.2) is derived in appendix C. The presence of an external magnetic field $\mathbf{H}_{ext}$ introduces a Zeeman term in the free energy,

$$E_Z = -\mathbf{M} \cdot \mathbf{H}_{\text{ext}} \tag{3.3}$$

where $\mathbf{M}$ is the magnetization. Even at higher temperatures and for non-collinear states, the presence of the Zeeman term requires the average magnetization of the phase to be aligned with the field. For low fields at sufficiently high temperatures, the system undergoes a phase transition from FM to Cyc, exhibiting a phase with zero average magnetization at zero field. Thus, Cyc does not gain energy linearly on the Zeeman term. However, it has a larger entropy contribution than FM, as well as a large contribution from the DM interaction due to the rotation of the spins. In fact the energy due to DM interaction $\sim \mathbf{S}_1 \times \mathbf{S}_2$ is zero for the FM phase while it has a finite value in the Cyc phase. Higher values of the field will ultimately dominate over the entropy term, bringing the system back to FM even at high temperatures, but before that an intermediate SkL phase is stabilized. The SkL phase can be considered as a FM phase with isolated magnetic bubbles dispersed through it. Therefore the overall magnetization value is close to that of the FM phase, as favored by the Zeeman term. However, the inner structure of the skyrmions allows an energy gain thanks to the DM term and the entropy term.

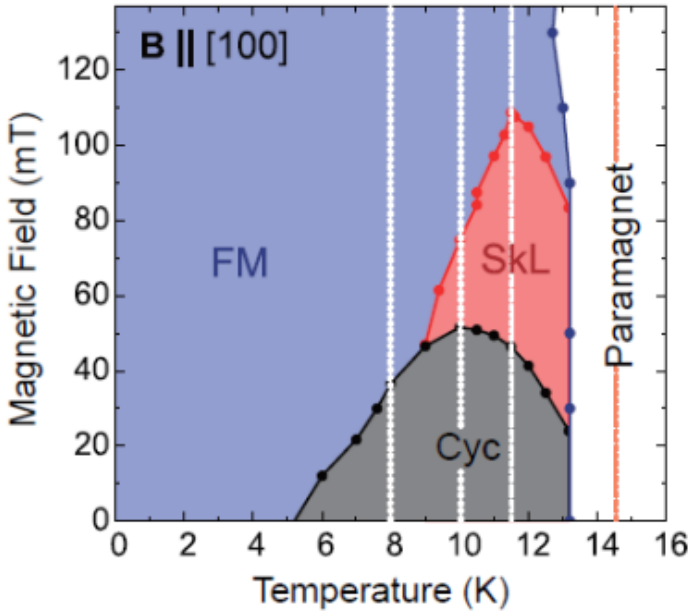

Figure 3.3: Phase Diagram of GVS in an external magnetic field applied along the cubic [100] direction. The vertical line at 10 K indicates the conditions of the measurements, that we interpret in the sections 3.2.1 and 3.4. Data from [35].

3.2.1 Experimental data

In this Chapter, the motivation for the analysis of the properties of GVS came from an experimental study of the material via time-resolved magneto-optical Kerr Effect (trMOKE, a review: [42]). When light is reflected from a magnetized surface, the intensity and polarization of the reflected beam changes due to the presence of the magnetization. Thus, by analyzing the reflected light from a material, it is possible to characterize its magnetization texture.

Besides being a non invasive and powerful tool to provide a detailed description of the magnetic properties of GVS, trMOKE is also ideal to study the response of the system to photoexcitations. Spins interact with the electromagnetic field of light: a spin in a magnetic field is subject to precession. In fact, a precession of the magnetization is observed in GVS as a consequence of photoexcitation. Additionally an excitation of skyrmion breathing modes [43] is observed, opening an interesting opportunity to study skyrmion dynamics. These studies lay the groundwork for a better comprehension, and ultimately a realization, of skyrmion-based devices. Furthermore, once the system is excited it is possible to study the thermalization process, which offers the possibility to comprehend how the various degrees of freedom (i.e. electrons, spins and the lattice) interact and exchange energy, how the excitations scatters and what role the background magnetic structure plays in the dynamics of these entities.

Fig. 3.4 shows trMOKE data [44] at 10 K, while the external magnetic field runs from 30 to 120 mT, spanning through the Cyc, SkL and FM phases as seen in Fig. 3.3. The figure represents the measured change in the polarization of light after it reflects on the magnetized surface of GVS. The phase of the reflected light changes after the reflection on a magnetized surface and is directly proportional to the magnetization of the material. When magnetization changes due to photoexcitation, the change is observed in the phase

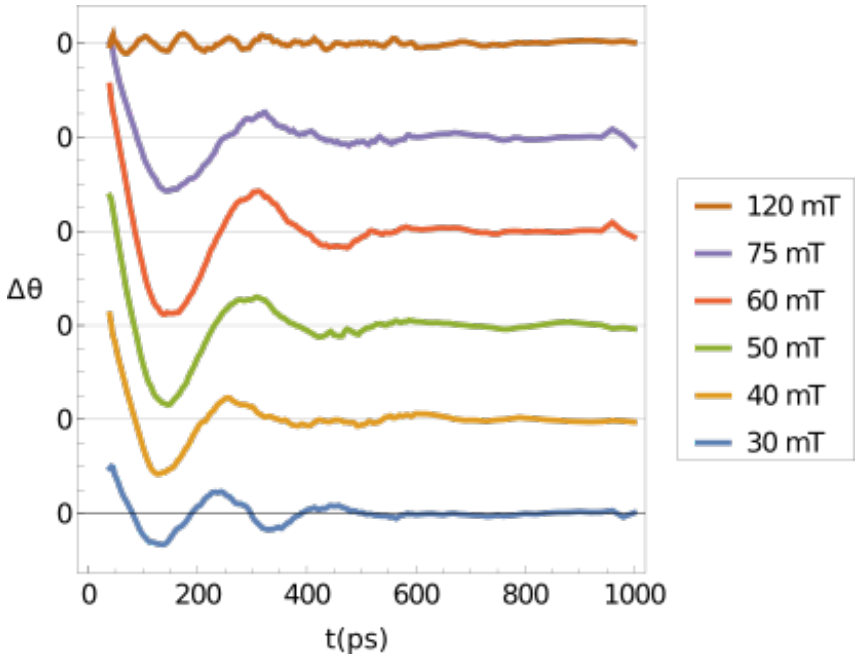

Figure 3.4: Experimentally observed coherent oscillation of the magnetization component along the direction of the external magnetic field [44]. The polarization change ($\Delta\theta$) in the reflected light is directly related to the magnetization inside the material. Measurements are taken at 10 K, different magnetic fields (highlighted with different colors) are applied to select different phases along the phase diagram. Plots are rescaled vertically, horizontal lines added for reference

of the reflected light. A damped mode with frequency in the GHz range is visible from the experiment. The oscillation of the magnetization can be interpreted as the result of coherent spin precession around the direction of the external magnetic field. The observed modes have been excited through interaction with the light. It has been suggested earlier [35], that such a coherent spin precession may be triggered by a photo-induced quench of the anisotropy .

This response arises from the competition between external magnetic field and anisotropy. Let $\mathbf{a}$ and $\mathbf{b}$ be the unitary vectors in the direction of the magnetic field and the anisotropy, respectively. In the equilibrium state, the preferable spin direction will be some intermediate direction between the direction of the field and the anisotropy, i.e. $\alpha\mathbf{a} + \beta\mathbf{b}$. The magnitude of the coefficients α and β depends on the strength of the two competing terms. If a sudden quench of the anisotropy happens, a new direction $\alpha'\mathbf{a} + \beta'\mathbf{b}$, with $\alpha' > \alpha$ and $\beta' < \beta$, is preferred and therefore spins tilt more towards the direction of the magnetic field. The perturbation of the spin order forces a magnetization precession around the axis of the field, thus exciting the magnons responsible for the precession. As time passes, the energy pumped into the system through photoexcitation gets transferred to the rest of the material through magnon-phonon coupling, re-establishing the local equilibrium before the excitation, and bringing the magnetization back to the initial state. The time necessary for the magnetization to be restored to the initial value (recovery time) has also been measured and is shown in Fig. 3.5, and is directly related to the thermal conductivity of GVS.

As it is evident from Fig. 3.5, different phases correspond to different recovery times, and thus to different thermal conductivity values. The reason behind this difference

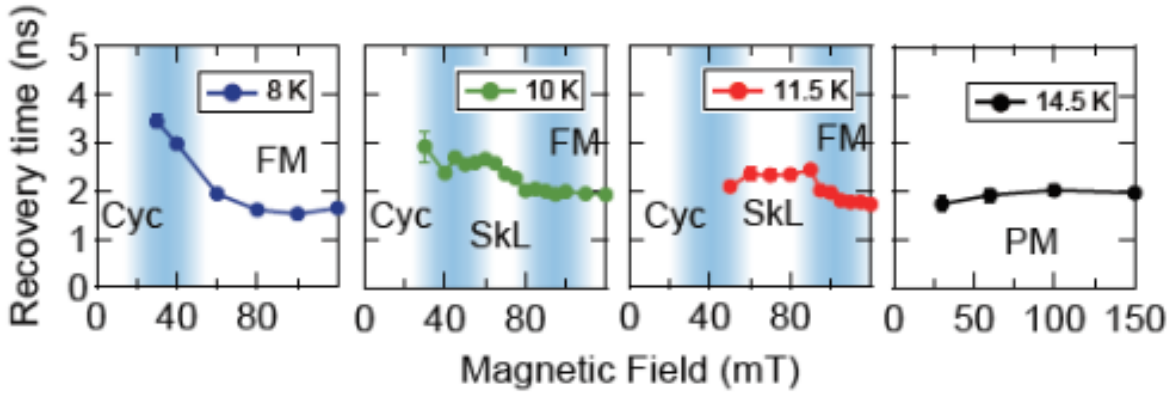

Figure 3.5: Recovery time in GVS measured for different temperatures [44]. After the photo-excitation, the material relaxes to the previous value of the magnetization, the recovery time differs from phase to phase.

lies in the mechanism of thermalization, i.e. the transfer of energy through magnon-phonon coupling and the scattering of magnons along the magnetic texture of the material. Fig. 3.5 shows that the the Cyc and SkL phases have higher recovery time, i.e. lower thermal conductivity, than the FM and paramagnetic phases. This is due to the magnon scattering.

The photoexcitation induces magnetic excitations in the system. The excess energy stored in the magnons is then distributed to the rest of the system via thermalization. Therefore the magnon scattering plays a major role in this.

When the heat that has been introduced in the system from the photoexcitation is carried away by the magnons the magnetization returns to its initial value. For this to happen, magnons need to efficiently carry away the heat from the excited region. The ability to transfer heat away from the excited region is related to the mean free path of magnons. For example, a magnon that scatters off a magnetic defect exchanges heat at the scattering site, exciting another magnon or eventually transferring energy to the lattice. If the magnetic defect is close to the excited region, the local temperature does not decrease significantly, and the thermalization process requires more scattering events to dissipate the heat. To summarize, if magnons scatter more, their mean free path is lower, and thus the thermalization is slowed down. This happens in the Cyc and SkL phases due to the complex magnetic order of the structures. As we discuss in the following, upon the transition to the Cyc phase abundant chiral DWs appear which likely limits the magnon mean free path.

In the Cyc phase the spins arrange into a cycloidal configuration, but it is common for DWs to arise at the phase transition. These DWs separate regions where the cycloidal order is different, e.g. the spin rotation verse or the direction of the wave vector are different. DWs are objects whose presence alters the magnetic properties of the material and hence the magnon dynamics. In this scenario they act as magnetic defects that scatter magnons. The great number of DWs in the cycloidal phase (cf. Fig. 3.6) alters the magnon dynamics, slowing down the process of thermalization and explaining the high recovery time observed in this phase. The SkL phase shows a more regular magnetic structure that can be pictured as follows: a uniform magnetic texture similar to a FM state with magnetic bubbles. The skyrmions, uniformly distributed in the FM background, as seen in Fig. 3.6. In regard to the magnon dynamics, skyrmions also act as magnetic defects and

scatter off the magnons slowing down the thermalization process. It must be considered that the more regular distribution of skyrmions and the overall magnetic order outside them provides a better environment for the diffusion of heat through magnons, hence explaining a recovery time lower than that in the Cyc phase, but still higher than the FM one. Finally, as the FM and paramagnetic (PM) phases do not show this kind of magnetic defects, the magnon dynamics are not altered. In fact the two phases show similar values of the recovery time.

In the next section we will introduce and describe the model that provides the theoretical framework on which our analysis is based.

3.3 The model

In the beginning of the previous section we described the properties and the structure of GVS. We stated that the magnetic properties of the material are due to the V_4 tetrahedra and that, due to the lacunar spinels lacking every other A atom in the common spinel structure AB_2X_4, the V_4 are not uniformly distributed but are arranged in larger and smaller tetrahedra. The V atoms are in different oxidation states; nominally a V_4 tetrahedron contains three V^{3+} and one single V^{4+} and all the atoms hybridize to form a V_4 cluster with a total spin of 1/2.

We model the magnetic structure of GVS by considering the sublattice formed by V_4 clusters. The effective spin-spin interaction is described with a semiclassical approach. While semiclassical treatment would not usually be justified for $S = 1/2$, GVS is long range ordered and the spin texture is locally ferromagnetic, which makes the effect of quantum fluctuations negligible. More detail is given in Section 3.4. We thus approximate our system with a classical Hamiltonian

$$\mathcal{H} = -\sum_{i,j} J_{ij}\mathbf{e}_i \cdot \mathbf{e}_j - \mathbf{D}_{ij}\mathbf{e}_i \times \mathbf{e}_j + K_i(\mathbf{e}_i \cdot \mathbf{n}_K)^2 - \mu_{\mathrm{B}}\mathbf{B}^{ext} \cdot \mathbf{e}_i. \tag{3.4}$$

The Hamiltonian is written in terms of unitary vectors $\mathbf{e}_i$ that represent the direction of the spin $\mathbf{S}_i$ at site i. J_{ij} is the exchange coupling between in-plane or out-of-plane neighboring spins i and j, $\mathbf{D}_{ij}$ is the DM vector, K_i is the easy axis anisotropy constant related to the distortion along the direction $\mathbf{n}_K$, the [111] direction of the cubic lattice on which the V_4 sit, $\mathbf{B}^{ext}$ is the external magnetic field.

In order to describe the excitations and the time-dependent dynamics in GVS we make use of the Landau-Lifshitz-Gilbert (LLG) equation [45]:

$$\frac{d\mathbf{m}_i}{dt} = -\frac{\gamma}{1+\alpha^2}\mathbf{m}_i \times [\mathbf{B}_i + \mathbf{b}_i(t)] - \frac{\gamma}{m}\frac{\alpha}{1+\alpha^2}\mathbf{m}_i \times (\mathbf{m}_i \times [\mathbf{B}_i + \mathbf{b}_i(t)]). \tag{3.5}$$

The LLG equation describes the precessional motion of the magnetic moment $\mathbf{m}_i$, with modulus m, inside a material. In our case the magnetic moment is related to the total spin $\mathbf{S}_i$ of the V_4 cluster by the relation $\mathbf{m}_i = g\mu_B/\hbar\mathbf{S}_i$. The coefficient γ is the gyromagnetic ratio. $\mathbf{b}_i(t)$ is a stochastic magnetic field that mimics the effect of finite temperature by introducing Gaussian fluctuations into the dynamics of the magnetization, which has the following properties

$$\langle b_{i\mu}(t)\rangle = 0, \qquad \langle b_{i\mu}(t)b_{j\nu}(s)\rangle = 2D\delta_{\mu\nu}\delta_{ij}\delta(t-s), \tag{3.6}$$

where $\langle ... \rangle$ represents the time average, μ and ν select the Cartesian components of the vector $\mathbf{b_i(t)}$. δ_{ij}, $\delta_{\mu\nu}$ are Kronecker deltas and $\delta(t-s)$ is the Dirac delta. D is the amplitude of the stochastic field $\mathbf{b_i(t)}$ [46]

$$D = \frac{\alpha}{1+\alpha^2}\frac{k_B T}{\gamma m}. \tag{3.7}$$

and α is a damping parameter. Finally $\mathbf{B}_i$ is the effective magnetic field acting on the single magnetic moment $\mathbf{m}_i$, and responsible for the precessional motion of the magnetic moment. Its expression is obtained from the previously defined Hamiltonian (3.4),

$$\mathbf{B}_i = -\frac{\partial \mathcal{H}}{\partial \mathbf{m}_i} = -\frac{1}{m}\frac{\partial \mathcal{H}}{\partial \mathbf{e}_i}. \tag{3.8}$$

where in Hamiltonian (3.4) $\mathbf{e}_i = \mathbf{m}_i/m$. With Eqs. (3.4) and (3.5) we are able to model the real material. We begin by inserting experimental information such as interaction strength, geometry, symmetries etc. in Eq. (3.4). In particular, exchange coupling J and DM vectors $\mathbf{D}_{ij}$ are taken from [47]. We then use the Hamiltonian to describe, for every spin, the effective magnetic field that produces the evolution of the system, and use the LLG equation to describe such evolution.

In the next section we show in detail the simulation we performed for GVS, highlight the commonalities and differences with the experimental data that we described in section 3.2.1, and discuss the results.

3.4 Simulations and results

In this section we report and discuss the results of our theoretical work and simulation for GVS. Our analysis makes use of the atomistic spin dynamics approach [48], that is implemented in the UppASD program [46]. It has been mentioned that the model which we base our study on is a classical one, even if the spins of the V_4 tetrahedra have a total value of 1/2. A classical model can be used in this case because of the particular spin texture of GVS. As the different magnetic orders are stabilized, the total order is reached on a long length scale compared to the single unit cell length (for example the periodicity of Cyc and SkL phase is of the order of 20 nm). This means that the change in magnetization is smooth through the cells, and that the spin direction varies slowly along the lattice resulting in short scale ferromagnetism that can be well described even with a classical model, such as the one implemented in the UppASD software [46].

Fig. 3.6(a-f) shows the simulated phases of GVS, the temperature in the simulation is different from the real material. We use the simulated phase diagram to rescale the temperature in the software to the equivalent real one. We present different snapshots of the simulated phase diagram at an equivalent temperature $T = 12$ K. For each snapshot we plot the relative dispersion relations for magnons. The simulation successfully reproduces the phase diagram, as the magnetic field is increased a Cyc phase, a SkL phse and a FM phase are obtained As we will discuss later on, there are some caveats about the aforementioned results. The finite size of the simulation cell, as well as the use of a classical model, causes a change in the value of the critical temperature and of the coupling with the external magnetic field. The temperatures and fields we report are rescaled to match the experimental observations.

Fig. 3.6(a'-f') shows the computed magnon branches that are crucial in the understanding of the thermal properties of GVS. The magnon branches are obtained from the magnon

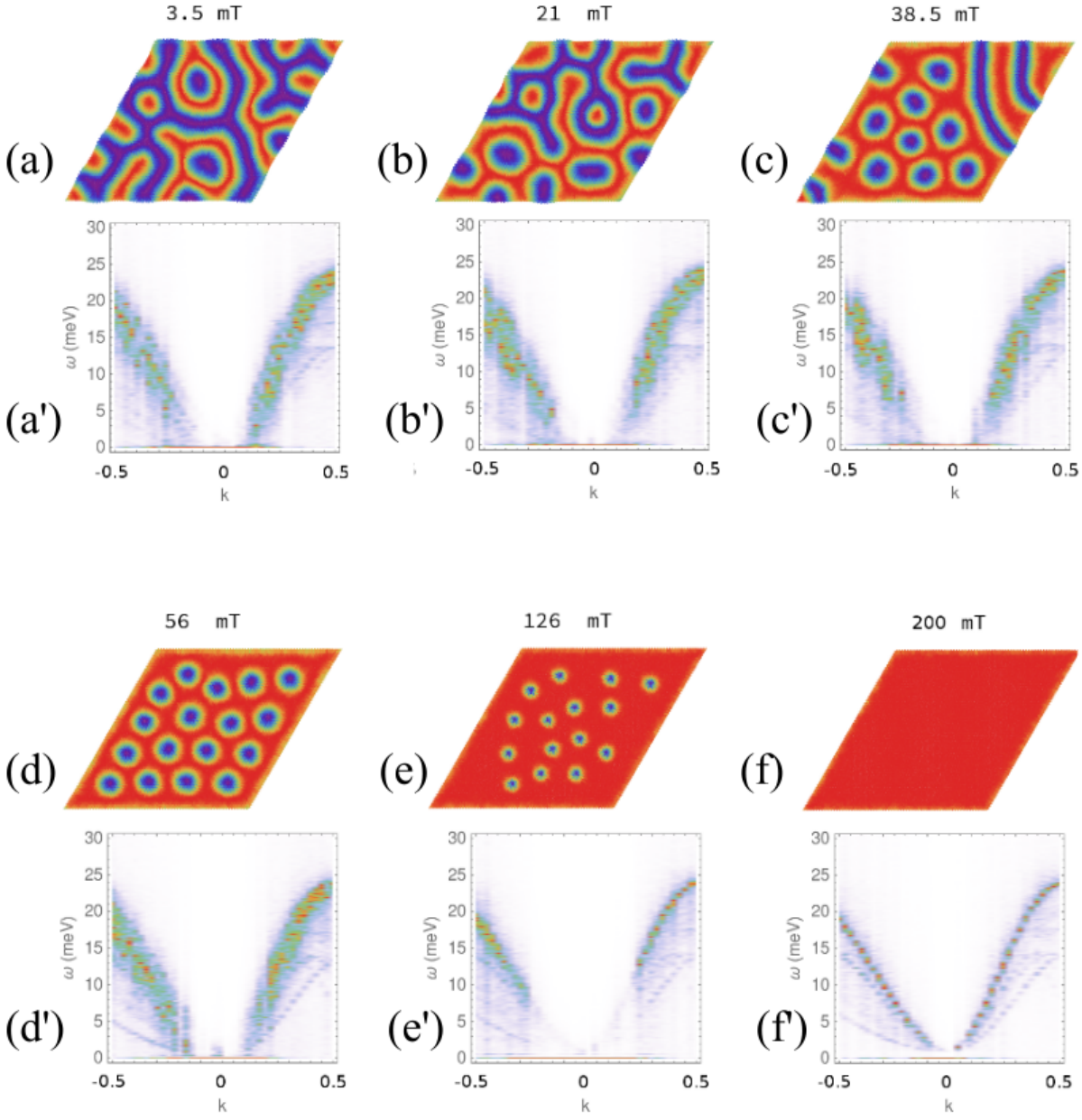

Figure 3.6: (a-d) Phase diagram simulated with UppASD for increasing values of the external magnetic field computed at an equivalent temperature of 12 K. A disordered spiral state is visible at the lowest magnetic fields. As the field increases the magnetic domains order and nucleate creating the magnetic texture typical of the SkL phase. Finally as the field further increases, the skryrmions become smaller until they disappear and the FM phase is reached. Color scale reflects the directions of spins, red are spin up and blue are spin down in the direction perpendicular to the page. (a'-d') Magnon spectral functions corresponding to top row phases. The more disordered the phase the broader the spectral function. The combination of disorder, and the presence of defects and magnetic DWs, results in the scattering of magnons, and hence introduces a change in their wave vector k. The smearing in the magnon branches is inversely proportional to the mean free path of the magnons. A lower mean free path results in a lower thermal conductivity, explaining the measurements of recovery time reported in Fig. 3.5. Color scale encodes the intensity of the spectrum.

spectral function. It is possible to compute this quantity through the time-dependent correlation function $C^j(\mathbf{r}-\mathbf{r}',t)$ of the Cartesian component j of the magnetization $\mathbf{m}_\mathbf{r}^j(t)$ at position $\mathbf{r}$ and time t:

$$C^j(\mathbf{r}-\mathbf{r}',t) = \langle \mathbf{m}_\mathbf{r}^j(t)\mathbf{m}_{\mathbf{r}'}^j(0)\rangle - \langle \mathbf{m}_\mathbf{r}^j(t)\rangle \langle \mathbf{m}_{\mathbf{r}'}^k(0)\rangle , \tag{3.9}$$

whose Fourier transform gives the dynamical structure factor, $S^j(\mathbf{q},\omega)$.

$$S^j(\mathbf{q},\omega) = \frac{1}{\sqrt{2\pi}N}\sum_{\mathbf{r},\mathbf{r}'} e^{-i\mathbf{q}\cdot(\mathbf{r}-\mathbf{r}')}\int_{-\infty}^{+\infty} e^{i\omega t}C^j(\mathbf{r}-\mathbf{r}',t)dt. \tag{3.10}$$

This quantity is directly computed by the software from the average values of the magnetization that have been sampled during the simulated time evolution. As we discussed in Section 3.2.1, the thermal conductivity changes considerably in the different phases. We see in Fig. 3.6 that the magnon branches for the different phases have similar shapes however the more "disordered" a phase appears, i.e. the farther is from the FM state, the broader the magnon branches are. The reason behind this broadening is due to the magnons scattering off the DWs or magnetic features that characterize the Cyc and SkL phases. The broadening is then inversely proportional to the magnon mean free path, that is approximately given by the distance between defects. The contribution of the single magnon to the thermal conductivity, κ_i, is given by

$$\kappa_i = c_i v_i \rho_i \tag{3.11}$$

where c_i is the specific heat of this particular magnon mode i, v_i is the velocity and ρ_i is the mean free path of the magnon. The total thermal conductivity is the sum over all the channels that contribute to the heat transport. In this case it will be only over the magnons that are excited. In order for the magnetic order to affect the thermal conductivity of the system at least one of the quantities on the RHS of Eq. (3.11) must change. It is evident that only the mean free path of the magnon will be affected by the presence of magnetic DWs that are distributed in the Cyc or SkL phase and are absent in the FM phase. Thus the broadening of the magnon branches in k-space and the change of thermal conductivity are both consequences of the same scattering mechanism and the simulated broadening provides an indication for the experimentally observed thermal conductivity.

We now move to the study of the light-induced precession motion of the magnetization in GVS, as it is portrayed in Fig. 3.4. This particular task has been revealed to be quite challenging as the quenching mechanism induced by the laser excitation is not still fully understood. Our simulation provides a qualitative tool to support considerations on the quenching mechanism, but fails to exactly reproduce the experimental data. The reasons behind this discrepancy are diverse and will be discussed later.

The hypothesis we wanted to test is that the laser excitation triggers a quench of the anisotropy in GVS [35]: the laser would locally heat the material and change the geometric structure, a change that has repercussions for the anisotropy of the heated region. The spins precess to adjust to the new magnetic Hamiltonian: magnon modes are excited and are responsible for the change in the magnetization that is observed. In order to imitate this we manipulate the model parameters. We initialize the system with a set of physical quantities and let the magnetization evolve according to the LLG equation for a certain amount of time, then we change the anisotropy constant K_i in Eq. (3.4) to mimic the

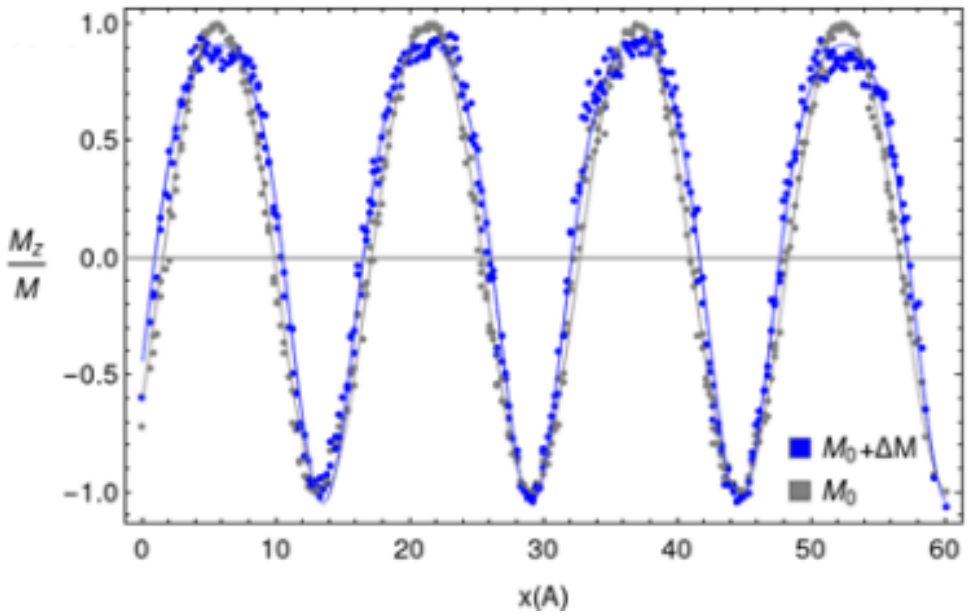

Figure 3.7: Photo-induced mode on the Cyc phase. Projection of the magnetization along the excited magnon mode before (grey) and after (blue) quenching. The excited mode slightly couples to the Cyc phase resulting in a weak decrease of the peaks of magnetization; the excited mode effectively "presses on" the spiral.

excitation and let the evolution proceed again. We simulated the response in the three phases, Cyc, SkL and FM (Figures 3.7, 3.8 and 3.9).

Figures 3.7 and 3.8 show the effect of the simulated quenching on the Cyc and the SkL phases. The effects on the FM phase are discussed later on. The response of the different phases to the excitation is qualitatively and quantitatively different. The laser photo-induced excitation has little effect on the Cyc phases; as Fig. 3.4 shows, the excitation amplitude in the Cyc phase (that is for the smallest external magnetic field) is smaller than in the SkL phase (around 50 mT in the figure).

It is not easy to see a change in the magnetic texture of the Cyc phase. In order to highlight it, we project the magnetization for the Cyc phase onto the main Fourier mode $e^{(i\omega t)}$ before and after the quenching. We see only a small variation of the projected

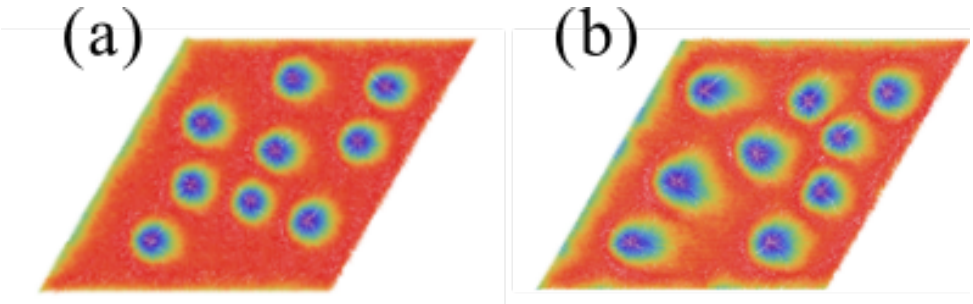

Figure 3.8: Breathing mode excitation in the SkL phase for (a) unquenched and (b) quenched SkL phase. The anisotropy is set in the plane for easier visualization of the effect of the mode. The skyrmions deform in the direction of the anisotropy, the excited mode is a breathing mode for the skyrmions. The color scale reflects the directions of spins, red are spin up and blue are spin down, in the direction perpendicular to the page.

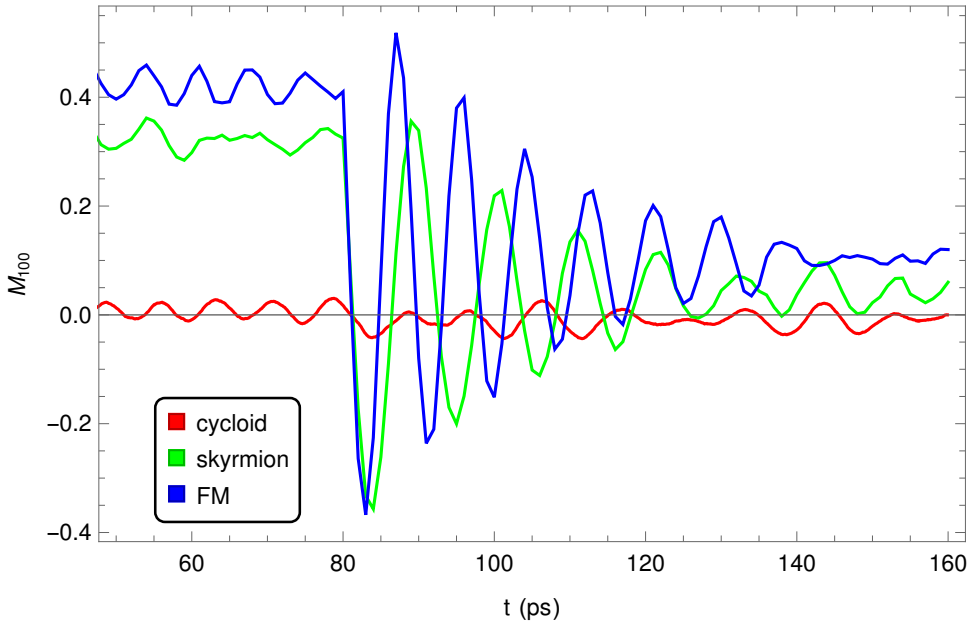

Figure 3.9: The simulated dynamics of the magnetization along [100] cubic direction in the three phases following the anisotropy quench. The anisotropy is quenched at 80 ps. The state was prepared using LLG dynamics with high Gilbert damping.

magnetization: the excited mode affects the Cyc phase by slightly "squashing" it, thus making the spiral more "square-shaped".The measurements and the simulations show that the effect is minute, thus indicating small coupling of the excitation to the squashing mode. Magnetization oscillations are stronger in the SkL phase. Fig. 3.8 shows that skyrmions are significantly deformed by the excited mode and this is consistent with the higher oscillation amplitude of the magnetization in the SkL phase in Fig. 3.4.

The last part of our analysis concerns the coherent dynamics of magnons that we showed in Fig. 3.4. As we mentioned earlier our simulation does not reproduce the experimental results in their entirety but still provides valuable information that can help understand, or rule out, the proposed anisotropy quenching mechanism. Fig. 3.9 shows the simulated oscillation of the magnetization, projected on the direction of the magnetic field, that is the [100] direction of the cubic V_4 lattice. To proceed we select one of the three magnetic phases (Cyc, SkL or FM) by setting the temperature and the external magnetic field to appropriate values according to the simulated phase diagram (Fig. 3.6) and let the system stabilize by evolving it under LLG dynamics, first with large damping, and then with regular damping.

At 80 ps we manually quenched the anisotropy of the system and we observe a strong response of the magnetization for FM and SkL phase, but only a small response in the Cyc phase. Comparing the simulation with the experimental plot we identify a number of inconsistencies:

- the oscillation frequency is not reproduced: the experimental oscillations are in the GHz range, while the simulated ones are of the THz range. In Fig. 3.4;
- the response of the FM phase is greatly different: in the simulated scenario the magnetization in the FM phase strongly oscillates after the quenching of the anisotropy, while the measured magnetization is hardly affected by the excitation;

- the oscillation in the Cyc phase is also quite different in the two cases: the overall shape is different, but simulation and experiments agree with the Cyc phase being weakly excited.

3.5 Conclusions

In this Chapter we have addressed recent experiments on the dependence of thermal conductivity in GVS on the magnetic phase. The decrease of the thermal conductivity in the SkL and especially Cyc phase is suggested to result from DWs scattering magnons, and thus reducing the magnon mean free path. We have also simulated the coherent oscillations of magnetization following the anisotropy quench, which was proposed earlier as the major effect of the photoexcitation on the magnetic subsystem. We also analyzed the result of anisotropy quench coherent magnetization precession have inconsistencies with the experiment, suggesting that anisotropy quench may not be the adequate way to mimic the photoexcitation. A solution could be related to the anisotropic g-factor, resulting from Jahn-Teller distortions. Heating may reduce the distortion amplitude, thus changing the g-tensor. We plan to test this hypotesis in a future work as the change in the g-tensor may be modelled, in our simulations, by a magnetic field rotation.

Chapter 4

Improper ferroelectricity in metal-organic frameworks

4.1 Introduction

In the previous chapters we encountered a number of recurring elements. We have shown how even simple models based on symmetry considerations or experimental input of the ground state can give valuable insights into the properties of materials. In this Chapter, group theory analysis will be the cornerstone used to build a theory of ferroelectricity in metal-organic frameworks (MOFs). They are hybrid organic-inorganic compounds, that can be easily synthesized without resorting to high-temperature growth and expensive rare earth cations [49]. A major challenge, up to date, is still that of synthesizing chemically and mechanically stable MOFs.

The reason why hybrid compounds are attracting great attention in the last decade [50] are numerous. Although less stable, organic-based perovskites are reported to host similar functionalities to their inorganic counterparts, resulting in possible devices that are both cheaper and, in some cases, more performant than their inorganic counterparts (e.g. methylammonium-based perovskite solar cells significantly surpass traditional ones in efficiency). The presence of organic molecules can enable novel properties, not replicated by any inorganic-based compounds, such as mechanical softness driven exciton trapping leading that makes broad emission bands in white LEDs possible [51].

In this Chapter we study $NH_2(CH_3)_2Fe^{II-III}(COOH)_3$ (Fe-MOF), with a perovskite-based structure, similar to the usual ABX_3, but where the A-site cation is substituted with a large organic molecule, in our case dimethylammonium (DMA), $NH_2(CH_3)_2$, while Fe cations in the B site are linked by formate COOH. While initial studies in DMA-based MOFs reported antiferroelectric states related to toroidal ordering of DMA [52, 53, 54], later studies found ferroelectric polarization connected to the canting of DMA cations and associated hysteresis loops were observed in Mn, Co, Fe, Ni, [55]. $(DMA)Fe^{II-III}(COOH)_3$ has $R\bar{3}c$ space group below 155 K [54]. In this phase DMA, molecules that are organized in a hexagonal structure, arrange themselves in a toroidal pattern. Magnetic ordering of Fe ions and their different oxidation states leads to a ferrimagnetism below 40 K.

The main focus of this Chapter is to identify the origin of ferroelectricity that has been observed in $(DMA)Fe^{II-III}(COOH)_3$. Since DMA molecules are polar we can assume that the antiferroelectric molecular ordering is related to the observed electric polarization. In fact, molecular ordering is the only observed transition in these materials and ferroelectricity in molecular compounds has recently been observed [56].

This Chapter is dedicated to test this hypothesis. The structure of the Chapter is the following: we start by first describing the material, its crystal structure, and its properties. We then analyze the structure of the material above and below the ordering temperature. Next we perform the symmetry analysis, which identifies the distortive modes active at the phase transition and provides the understanding of interactions between different modes. A Landau theory of the phase transition is formulated. Finally, the phase diagram of the model is investigated and results are compared with experimental data and Density Functional Theory (DFT) simulations to contextualize and give physical meaning to the model parameters we introduced.

4.2 The Material

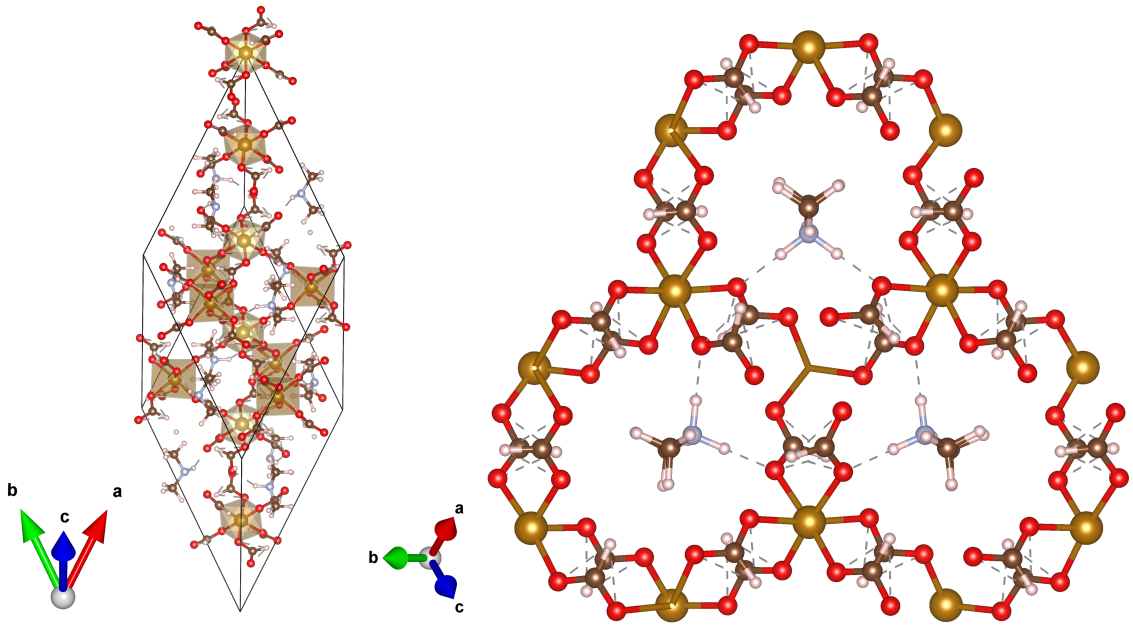

Figure 4.1: (left) Rhombohedral unit cell of (DMA)$Fe^{II-III}(COOH)_3$ in the low temperature phase with the space group R3c (#161 in the international tables). (Right) View on a single layer along the threefold axis, with DMA molecules filling the voids between FeO_6. The cell orientation is indicated by the directions of translation vectors at the bottom left. Dashed lines show the hydrogen bonds between the molecules and the neighboring oxygens.

As introduced in the previous section, MOFs attract great interest, as many different materials can be used to fill the ABX_3 perovskite structure, giving a large variety of possible MOFs. As a starting point, we consider (DMA)$Fe^{II-III}(COOH)_3$ where Fe cation is at the perovskite B-site in ABX_3, and an organic linker X generates a scaffold where the DMA cation is accommodated at the A-site of the structure. A widely used choice for an organic linker is the formate ion $(COOH)^-$. With an approximate length of 4.5 Å it generates structures large enough to accommodate large organic cations such as DMA. Additionally, the formate ion and the organic cation can form hydrogen bonds, thus introducing new modes, and their behaviour depends on the choice of different organic cations.

The presence of Fe in $(DMA)Fe^{II-III}(COOH)_3$ makes this material one of the most interesting among the formate-MOF family and among multiferroic MOFs in general. Fe ions contribute to the materials magnetic properties, while the organic cation provides the electric dipoles. In fact, the magneto-electric (ME) effect has already been observed in this class [57, 58]. Usually ME coupling in this class of MOFs is weak due to weak superexchange interaction mediated by organic linkers. Furthermore, the ground state is usually AFM and ME control of polarization with a magnetic field is not possible.

$(DMA)Fe^{II-III}(COOH)_3$ is a hybrid organic-inorganic multiferroic material that at room temperature has a non-polar $P\bar{3}1c$ space group [54].

Below 155 K the unit cell triples as DMA molecules order in a toroidal fashion in the non-polar $R\bar{3}c$ structure, as seen in Fig. 4.1. However, there are indications that the structure may actually be polar, as a low ferroelectric polarization of $\approx$0.7 nC/cm^2 at 2 K has been observed [59] and a lower-energy polar structure R3c was later predicted from first principles [60].

To summarize, MOFs display an appealing variety of multiferroic properties. Even though the low temperature ME effect may not be the most appealing for applications, the observed high-temperature ferroelectricity and ferroelasticity [61] make this class of materials very attractive.

4.3 Symmetry Analysis

As discussed in the previous section, first-principles calculations indicate the polar space group R3c (#161 in the International Tables) [62] as the low-temperature polar structure of $(DMA)Fe^{II-III}(COOH)_3$. To construct an effective theory that explains the appearance of a ferroelectric polarization, we need to look for a parent group of R3c. To do this, we suppose that the distortions in the real material are due to the orientation of the molecules (that are disordered at a higher temperature state) hence, if the orientation of molecules is related to the distortions, we can remove the DMA molecules from the structure and look only at the distortions of the scaffold.

The search for a pseudosymmetric parent group proceeds in the following way: we call H the space group for which we need to find a parent group and G a possible parent candidate that contains all symmetry operators of H. If g_i are symmetry operators of G that do not belong to H we can write

$$G = H + \sum_i g_i H \tag{4.1}$$

where various $g_i H$ are called *left cosets* of H [63]. So, in order to find a proper parent structure for the group R3c we look for groups that contain all symmetries of R3c plus others (g_i). We apply the g_i transformation to the structure of our material and look at how the cell is transformed. If the difference between the original and the new structure does not exceed a certain threshold (i.e. the displacement is not big compared to the dimensions of the cell) then the new structure can be identified as a possible parent pseudosymmetric structure. We find the group $P\bar{3}_1c$ (#163 in the International Tables) to be an adequate parent group for the analyzed structure.

Now that we have identified the parent group of our structure, we want to find the order parameters that describe the phase transition between the two groups. In this regard it is necessary to know the *irreducible representations* or *irreps* of the highly symmetric

group, the transformation properties of the order parameters are in fact defined by some particular irrep that we will call "active irrep".

Let τ be an active irrep, g a symmetry of the low-symmetry phase, and X a possible order parameter of the phase transition. The irrep τ associates to g an $(n \times n)$ matrix $T_\tau(g)$ that leaves unchanged the n-dimensional order parameter X

$$T_\tau(g)X = X. \tag{4.2}$$

In general, if we repeat the previous procedure with a symmetry operation h that belongs to the highly symmetric group, and not to the low one, we obtain

$$T_\tau(h)X = X', \tag{4.3}$$

with $X \neq X'$. We understand from this case that X cannot be an order parameter as it is not invariant under the symmetries of the parent group. It is possible though to combine the different components of X to obtain invariant quantities. We later provide an example with the space groups of the system we are analyzing.

The problem of finding the active irreps when the high and low-symmetry groups are given is known as the "inverse Landau problem" [64] and the procedure is know as "mode decomposition" of the distorted structure. We find two irreps responsible for the phase transition from the group R3c to P$\bar{3}1c$ to be Γ_2^- and the 2-dimensional P_2. The transformation properties of Γ_2^- and P_2 under the generators of the group P$\bar{3}1c$ are reported in Table 4.1.

	1	3^+_{001}	$2_{1\bar{1}0}$	$\bar{1}$
Γ_2^-	1	1	-1	-1
P_2	$\begin{pmatrix} 1 & 0 \\ 0 & 1 \end{pmatrix}$	$\begin{pmatrix} 1 & 0 \\ 0 & 1 \end{pmatrix}$	$\begin{pmatrix} \cos\frac{\pi}{3} & -\sin\frac{\pi}{3} \\ -\sin\frac{\pi}{3} & -\cos\frac{\pi}{3} \end{pmatrix}$	$\begin{pmatrix} -1 & 0 \\ 0 & 1 \end{pmatrix}$

Table 4.1: Transformation properties of Γ_2^- and P_2 under the generators of the group P$\bar{3}1c$ (#163).

	1	3^+_{001}	3^-_{001}	$2_{1\bar{1}0}$	2_{120}	2_{210}
$\mathbf{Q_x}$	Q_x	Q_x	Q_x	$\frac{1}{2}Q_x - \frac{\sqrt{3}}{2}Q_y$	$\frac{1}{2}Q_x - \frac{\sqrt{3}}{2}Q_y$	$\frac{1}{2}Q_x - \frac{\sqrt{3}}{2}Q_y$
$\mathbf{Q_y}$	Q_y	Q_y	Q_y	$-\frac{\sqrt{3}}{2}Q_x - \frac{1}{2}Q_y$	$-\frac{\sqrt{3}}{2}Q_x - \frac{1}{2}Q_y$	$-\frac{\sqrt{3}}{2}Q_x - \frac{1}{2}Q_y$
	$\bar{1}$	$\bar{3}^+_{001}$	$\bar{3}^-_{001}$	$m_{1\bar{1}0}$	m_{120}	m_{210}
$\mathbf{Q_x}$	-Q_x	-Q_x	-Q_x	$-\frac{1}{2}Q_x - \frac{\sqrt{3}}{2}Q_y$	$-\frac{1}{2}Q_x - \frac{\sqrt{3}}{2}Q_y$	$-\frac{1}{2}Q_x - \frac{\sqrt{3}}{2}Q_y$
$\mathbf{Q_y}$	Q_y	Q_y	Q_y	$\frac{\sqrt{3}}{2}Q_x - \frac{1}{2}Q_y$	$\frac{\sqrt{3}}{2}Q_x - \frac{1}{2}Q_y$	$\frac{\sqrt{3}}{2}Q_x - \frac{1}{2}Q_y$

Table 4.2: Transformation properties of Q under all the symmetries of space group P$\bar{3}1c$ (translations are not reported for simplicity).

Let $\mathbf{Q} = \{Q_x, Q_y\}$ be the 2-dimensional order parameter that transforms according to the P_2 irreducible representation. We write the transformation properties of this order parameter under all the symmetries of the group P$\bar{3}1c$ in Table 4.2. The single components of $\mathbf{Q}$ are not invariant under the symmetries of P$\bar{3}_1c$. However, by considering appropriate combinations of Q_x and Q_y we can construct objects that are invariant under the symmetries of the group. Two easy-to-check cases are $Q_x^2 + Q_y^2$ and $3Q_x^2Q_y - Q_y^3$.

We verify the invariance of $Q_x^2 + Q_y^2$ under $2_{1\bar{1}0}$. Let us call $\mathbf{Q}'$ the transformed order parameter, therefore

$$\begin{aligned} Q'_x =& 2_{1\bar{1}0} Q_x = \frac{1}{2} Q_x - \frac{\sqrt{3}}{2} Q_y \\ Q'_y =& 2_{1\bar{1}0} Q_y = -\frac{\sqrt{3}}{2} Q_x - \frac{1}{2} Q_y, \end{aligned} \tag{4.4}$$

so that

$$Q_x'^2 + Q_y'^2 = \frac{1}{4}Q_x^2 + \frac{3}{4}Q_y^2 + \frac{3}{4}Q_x^2 + \frac{1}{4}Q_y^2 - \sqrt{3}Q_xQ_y + \sqrt{3}Q_xQ_y = Q_x^2 + Q_y^2. \tag{4.5}$$

In the same way it is possible to show that $Q_x^2 + Q_y^2$ is invariant with respect to all the other symmetries of $P\bar{3}1c$. The same holds for $3Q_x^2Q_y - Q_y^3$.

To summarize, we identified P_2 and Γ_2^- as the active irreps that describe the modes responsible for the phase transition from $P\bar{3}_1c$ to R3c. Now we choose $\mathbf{Q}$ as an order parameter that transforms according to P_2. Let us define P_z as the order parameter that transforms as Γ_2^-. From this point on we refer to $\mathbf{Q}$ simply as Q. We now combine P_z and the components of Q to obtain all possible terms, up to the 6^{th} order in Q and P_z, that are invariant under the group $P\bar{3}1c$. They are reported in Table 4.3.

Degree	Invariants
2	$Q_x^2 + Q_y^2,\ \ P_z^2$
3	$3Q_x^2Q_y - Q_y^3$
4	$P_z^4,\ \ Q_x^4 + 2Q_x^2Q_y^2 + Q_y^4,$ $P_z^2(Q_x^2 + Q_y^2),\ P_z(Q_x^3 - 3Q_xQ_y^2)$
6	$(3Q_x^2Q_y - Q_y^3)^2,\ \ P_z^6,\ \ P_z^4(Q_x^2 + Q_y^2),\ \ P_z^2(Q_x^2 + Q_y^2)^2$ $(Q_x^2 + Q_y^2)^3,\ \ P_z^3(Q_x^3 - 3Q_xQ_y^2),\ \ P_z(Q_x^2 + Q_y^2)(Q_x^3 - 3Q_xQ_y^2)$

Table 4.3: Invariants for symmetry group $P\bar{3}_1c$ (#163). Q_x and Q_y are the components of the P_2 mode while P_z refers to Γ_2^- mode.

We will show in the next sections how these invariant quantities enter the free energy of the system and how they can be used to describe the phase transition.

4.4 The model

In the previous section we described how to build invariant quantities in order to construct a theory of phase transitions for the studied system. The terms we found can now be used to write an expression for the free energy. Energy is a scalar quantity, thus it is invariant under all the symmetries that we considered. We want to write an expression for the free energy that describes the behavior of the system close to the phase transition from the group $P\bar{3}1c$ to R3c; we achieve that by writing a linear combination of the invariant quantities we just derived.

Instead of using the invariants in the form reported in Table 4.3, we adopt a change of variables. We rewrite the Q-mode in such a way that $\{Q_x, Q_y\} = \{Q\cos\phi, Q\sin\phi\}$, this will also be useful to better identify the symmetric structure of the energy. We report the

transformation properties of P_z and ϕ under the generators of the high-symmetry group in Table 4.4. We are now able to write the free energy F in the general form

$$F = \gamma P_z^2 - AQ^2 - BQ^4 + CQ^6 + \alpha Q^3 \sin 3\phi + \eta Q^6 \sin^2 3\phi + V(P_z, Q, \phi), \tag{4.6}$$

all parameters, as well as P_z and Q are dependent by the temperature T. We discuss the temperature dependence of F later in this section, and we omit it here for simplicity. P_z is the ferroelectric polarization component, and Q is the lattice distortion induced by toroidal molecular orientation. The first term describes the stable polar mode with ferroelectric polarization component P_z. We included all the interactions between P_z and Q in the potential

$$V(P_z, Q, \phi) = \beta P_z Q^3 \cos 3\phi + \mu P_z Q^5 \cos 3\phi. \tag{4.7}$$

Before discussing the terms in the expression of F we point out that we did not use all the terms of the 6^{th} order from Table 4.3. We did not include terms with powers of P_z higher than 1. The reason for this choice is that, as we will show in the following, P_z is confined in a parabola-like potential and is small close to the phase transition, therefore higher order terms in P_z will only add small corrections to F. The term $P_3^3(Q_x^3 - 3Q_cQ_y^2) = Q^3P^3 \cos 3\phi$ appears less trivial, but it has also been neglected. It is possible to show that it does not change the azimuthal angle of the minima of the free energy. We now discuss the terms

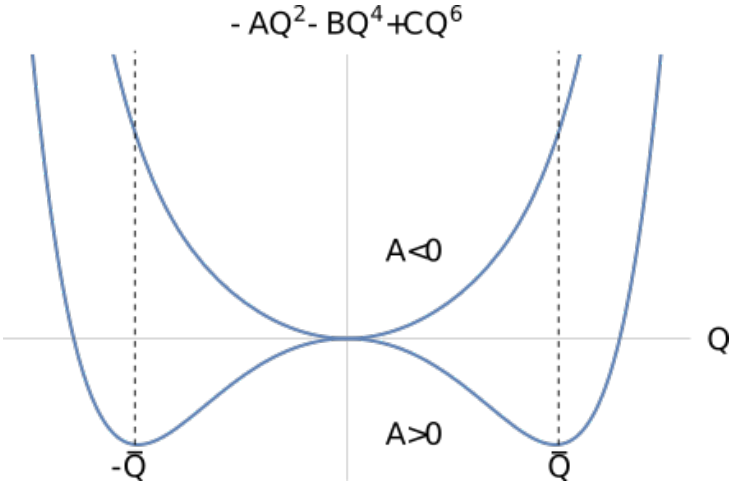

Figure 4.2: Q-dependence of the potential $-AQ^2 - BQ^4 + CQ^6$ for positive and negative A. If $A > 0$, the potential has two minima and the order parameter can assume finite values $\pm\bar{Q}$. If $A < 0$, the potential has only one minimum in $Q = 0$.

in the expression for F. The terms with coefficients A, B and C represent a Mexican hat-like potential for the Q-mode. Fig. 4.2 shows a simplified version of the potential.

The change of variables that we performed on Q highlights the 3-fold symmetric character of the mode (cf. Table 4.4). The mode is related to the hexagonal structure of the material, in particular to the distortions that induce the phase transition. We mentioned before that we consider the molecular order the cause of the distortions, therefore Q is the mode that describes the molecular ordering during the phase transition. In particular the terms with α and η account for the 3-fold symmetric anisotropy and are related to the symmetry of the scaffold that contains the molecules. The terms with β and μ describe an anharmonic interaction between the polar mode and the molecular order, which leads

to an improper ferroelectricity. The most important information about the coefficients is the following: the condition $\gamma > 0$ is required so that a stable polar mode with finite polarization P_z can exist. In the Mexican Hat term $C > 0$ is required to have a bounded Q mode. The coefficient A must be positive in the low temperature phase, i.e. before the phase transition, which ensures $Q \neq 0$ in the ground state. There are no constraints on the coefficient B, thus we select it to be positive for simplicity. No constraints are imposed on the coefficients α, β, η and μ. We find the value of polarization by minimizing the Landau free energy F with respect to P_z:

$$P_z|_{\min} = -\frac{\beta Q^3}{2\gamma}\cos 3\phi - \frac{\mu Q^5}{2\gamma}\cos 3\phi. \tag{4.8}$$

At this value of P_z the free energy takes the form:

$$F = -\frac{Q^6(\beta + Q^2\mu)^2}{4\gamma}\cos^2 3\phi + \alpha Q^3 \sin 3\phi + \eta Q^6 \sin^2 3\phi - AQ^2 - BQ^4 + CQ^6. \tag{4.9}$$

In principle, the substitution of P_z generates a term $-Q^{10}\mu^2/4\gamma$ in the free energy, where $\mu^2/4\gamma$ is positive. Thus, the introduction of an additional term DQ^{10}, $D > \mu^2/4\gamma$ would be required to keep the free energy bounded. However, we will not introduce such a term. There are two main reasons for this choice: first, μ, as a parameter of an higher order term with respect to β, should be comparable to β, if not smaller. Second, the order parameter Q, close to the phase transition, should assume small values, and therefore high powers of Q will provide small corrections in the first term of the free energy. We consider this a more adequate choice than expanding the free energy up to the 10^{th} order.

The term $\eta Q^6 \sin^2 3\phi$ has an important effect on the free energy. If $\eta < \eta_c = -\beta^2/4\gamma$, the $\sin^2 3\phi$ term dominates over the $\cos^2 3\phi$ one. This causes a different disposition of maxima and minima in the free energy. Figures 4.3 and 4.4 show the differences between the energy landscape when $\eta < \eta_c$ or $\eta > \eta_c$ for different values of the parameter α. A detailed discussion of the role of the η term is provided in Section 4.5.

Finally, we rewrite the free energy as follows:

$$F = -Q^6 \cos^2 3\phi + \alpha Q^3 \sin 3\phi + \eta Q^6 \sin^2 3\phi - AQ^2 - BQ^4 + CQ^6, \tag{4.10}$$

where the term in μ has been neglected and the other coefficients have been rescaled in order to have $\beta^2/4\gamma = 1$, thus $\eta_c = -1$. We notice that, aside from the coefficient dependence, the free energy F depends only on the magnitude of the distortive mode Q and the angle ϕ. Before moving to the next section we need to clarify the temperature dependence of the coefficients in the free energy. We will then proceed to describe the phase diagram of the system in the following section.

4.4.1 T-dependence of the coefficients

It is of fundamental importance for a phase transition theory that the order parameters behave correctly with the change in temperature, i.e. the order parameters shall be

	1	3^+_{001}	$2_{1\bar{1}0}$	$\bar{1}$
P_z	P_z	P_z	$-P_z$	$-P_z$
ϕ	ϕ	$\phi + \frac{2}{3}\pi$	$-\phi + \frac{3}{2}\pi$	$\phi + \pi$

Table 4.4: Transformation properties of P_z and ϕ under the generators of the group $P\bar{3}1c$ (#163).

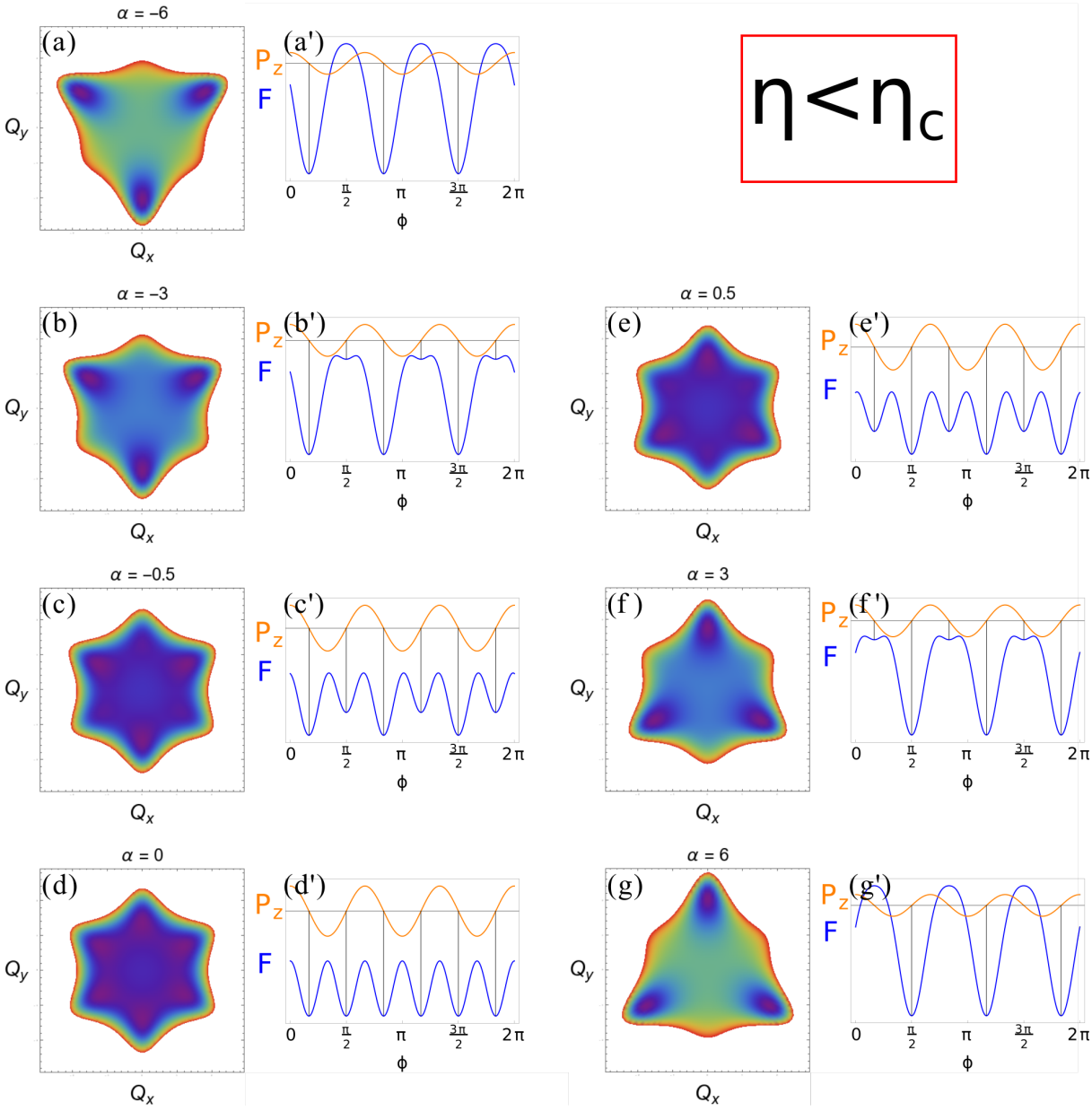

Figure 4.3: Free energy computed with $\eta < \eta_c$, in arbitrary units. (a-e) The potential energy landscape for different values of the parameter α. (a'-e') Free energy and polarization dependence on ϕ. The value of α is the same as in the left panel. Solid lines connect the minima of F with the corresponding value of P_z for easier visualization. The explicit dependence of P_z on α is not taken into account here but is portrayed in Fig. 4.5.

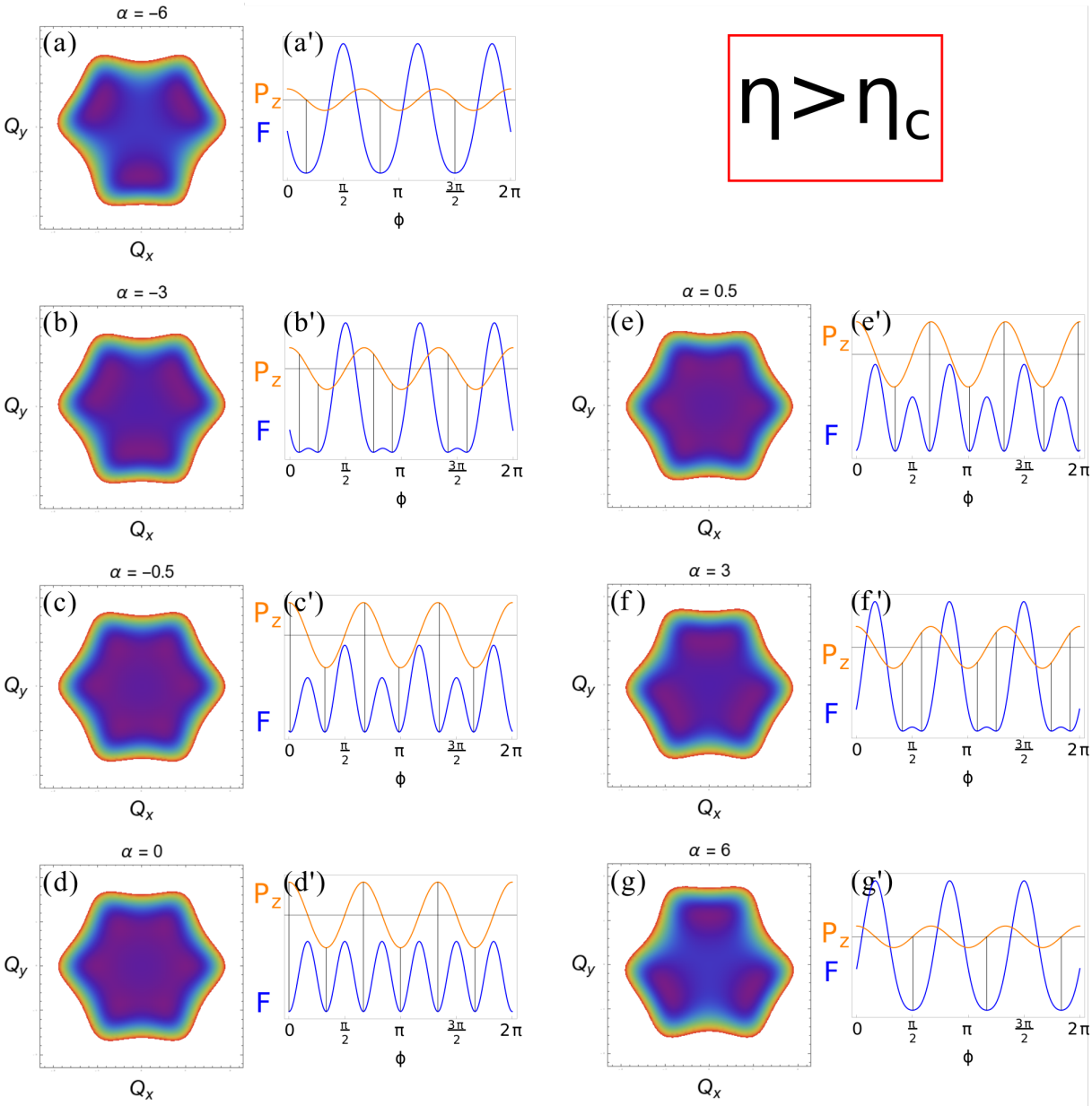

Figure 4.4: Free energy computed with $\eta > \eta_c$, arbitrary units. (a-e) The potential energy landscape for different values of the parameter α. (a'-e') Free energy and polarization dependence on ϕ, the value of α is the same as the panel on the left. Solid lines connect the minima of F with the corresponding value of P_z for easier visualization. The explicit dependence of P_z from α is not taken into account here but is portrayed in Fig. 4.5.

identically zero for temperatures above the critical temperature T_c at which the phase transition happens, and "condense" to non-zero values when the system undergoes the transition from the high-symmetry to the low-symmetry phase. In this regard we now explore in detail the temperature dependence of the coefficients of the model, as it has been formulated in Eq. (4.6). The temperature dependence is the same for the rescaled coefficients of Eq. (4.10).

As mentioned before, the coefficients $\gamma(T)$, $B(T)$ and $C(T)$ must be positive for the energy to have a minimum. In principle B may be negative if C is big enough, but we have selected $B > 0$ for simplicity. We assume these coefficients to be constant. Although more general considerations may require these coefficients to be T-dependent, it must be considered that the expression for the free energy is an expansion for temperatures close to the phase transition temperature T_c. In particular, we are considering an an expansion of the free energy for $T < T_c$ because for greater temperatures the order parameters will be zero, and the free energy will assume a constant high-temperature value that we can fix to zero. This means that in this theory γ will not change sign and thus a constant value is a well justified assumption.

The coefficient A is of critical importance in the expression of the free energy because it controls the shape of the bounding potential. Fig. 4.2 shows a simplified 2D case of the two possible shapes of the term $-AQ^2 - BQ^4 + CQ^6$ for positive and negative A. In the low temperature case, when $A > 0$, we observe the presence of two minima and the energy assumes a so-called "Mexican Hat" shape. In this case the Q-mode has a finite amplitude and, from Eq. (4.8), also a finite polarization. In the high temperature phase, when $A < 0$, the Mexican Hat turns into a parabola-like curve and, as there is only one minimum in $Q = 0$, the polarization is also zero.

We described how A must be positive in the ordered state for the potential to assume the Mexican hat shape. When the phase transition occurs the toroidal order must disappear and the ordering mode Q must become zero. These conditions are all realized if the coefficient A changes sign at the phase transition. As a consequence of the disappearing of the ordering mode the polarization also becomes null, because there is no longer a gain from a finite P_z through the P_z-Q coupling term.

To summarize, A must be a coefficient that changes sign with the phase transition. This constraint is enough to ensure the consistency of the model. A can be expressed as a Taylor expansion around the critical temperature T_c and has the form

$$A(T) = A_0(T_c - T). \tag{4.11}$$

Finally we consider the coefficients α, β and η. Formally the coefficients may have some kind of T-dependence. Here we will consider them to be constant and related to the properties of the material. Moreover, the α, β and η energy terms will vanish above the transition temperature due to the factor of $Q = 0$ in these terms. Therefore, in the vicinity of the phase transition, choosing these coefficients to be constant is the an adequate choice.

4.5 Phase diagram and composite domain walls

In the previous section we derived a model to describe the phase transition, related to molecular ordering, in $(\mathrm{DMA})\mathrm{Fe}^{\mathrm{II-III}}(\mathrm{COOH})_3$ from the highly symmetric $\mathrm{P\bar{3}1}c$ to the low-symmetry R3c structure. In this section, we will discuss the phase diagram of the model.

In the expression for the free energy, Eq. (4.10), the parameters α and η are not constrained. The two terms have different effects on the energy landscape, Figures 4.3 and 4.4 show this in detail. The α term is responsible for changing the minima structure of the free energy, it controls the transition from six to three minima. Figures 4.3 and 4.4 (d,d') both show a six minima structure in $\alpha = 0$ and both reduce to three minima for high values of α (arbitrary units are used), panels (a,a') and (g,g') of both figures. Figures 4.3 and 4.4 show that, for $\eta > \eta_c$ and $\eta < \eta_c$, the way the six minima reduce to three is different. The $\eta Q^6 \sin^2 3\phi$ term competes with the $-Q^6 \cos^2 3\phi$ term in Eq. (4.10), and the value of η selects if either the sine or cosine term dominates. Therefore, the role of the parameter η is to select between the two possible mechanisms for the six minima to be reduced to three.

We study the two cases $\eta > \eta_c$ and $\eta < \eta_c$. In particular we notice that, for high values of α, the case $\eta < \eta_c$ has sharp minima and smoother, or more rounded, maxima and *vice versa* for the case $\eta > \eta_c$. We can understand how six minima coalesce into 3 from panels (b,c,e,f) and (b',c',e',f') of both figures. In the case where $\eta < \eta_c$, three minima start rising (see, for example, panels (b',c') of Fig. 4.3) until they become flat maxima. In an analogous matter in the case $\eta > \eta_c$, three maxima grow while the other three maxima shrink (panels (b',c') of Fig. 4.4) until the situation with three flat minima and three sharp maxima is reached. In both cases when α changes sign the position of the minima is rotated by 30° (see, for example, Fig. 4.3(a,g)).

Only one of these two cases corresponds to a ferroelectric state. Fig. 4.3 shows that in the case $\eta < \eta_c$ the polarization is zero at the energy minima, while the case $\eta > \eta_c$ (Fig. 4.4) instead is compatible with the presence of ferroelectric polarization. Therefore, in the material of our study, $(\mathrm{DMA})\mathrm{Fe}^{\mathrm{II-III}}(\mathrm{COOH})_3$, non-zero experimentally measured polarization implies $\eta > \eta_c$. The case $\eta < \eta_c$ still deserves to be discussed, even if the polarization is zero at the minima. We do not have a ferroelectric polarization in this state, however, $P_z \sim Q^3 \cos 3\phi$ implies a non-trivial polarization texture at the DW where the polarization changes sign.

In the case $\eta > \eta_c$ the ϕ-dependence of the polarization P_z from Eq. (4.8) and of the free energy is illustrated in panels (a'-e') of Fig. 4.4. We observe that the free energy minima correspond to a finite polarization, depending on the value of α. At $\alpha = 0$, the free energy has six equivalent minima, corresponding to the maximal polarization amplitude, with signs of P_z alternating between the adjacent minima. When α is increased, three maxima become lower in energy, until they disappear and the six minima merge into three. At a certain critical value α_c the polarization at the minima (inside domains) becomes zero. At a negative α the opposite polarization domains are favored instead. Therefore, the phase diagram of the model has a ferroelectric phase for $|\alpha| < \alpha_c$ and a paraelectric phase at $|\alpha| > \alpha_c$. The sign change of α is only changing the sign of polarization, associated with the domains. The dependence of polarization on α is shown in Fig. 4.5.

We now consider DWs in the material, described by the free energy Eq. (4.10). For inhomogeneous order parameter configurations we complement Eq. (4.10) with the energy penalty for spatial order parameter variations. In this regard we suppose the parameter Q and P_z to be space dependent. The free energy in terms of the free energy density of a uniform state $F(Q)$ is:

$$\tilde{F} = \int d^3r \left[\frac{c}{2} \partial_i Q_j \partial_i Q_j + F(Q) \right]. \tag{4.12}$$

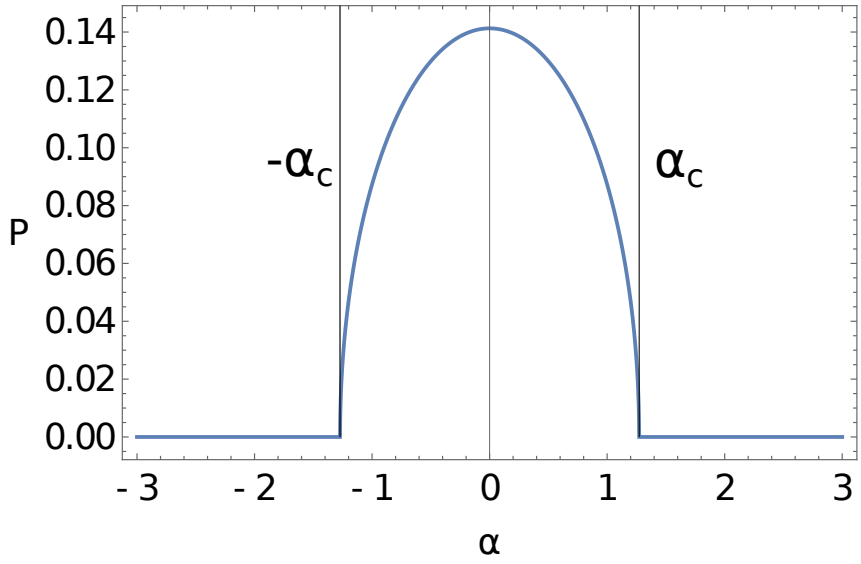

Figure 4.5: Dependence of the ferroelectric polarization on α computed for $\eta > \eta_c$ (arbitrary units). The value of polarization decreases with $|\alpha|$. For $|\alpha| > \alpha_c$ it is identically zero.

This form is similar to the action of a particle with mass m, moving in a potential $V(x)$:

$$\mathcal{L} = \int dt \left[\frac{m}{2}(dx/dt)^2 - V(x) \right], \tag{4.13}$$

which is minimized by the physical trajectory $x(t)$. The two expressions are related by the substitution $r \to t$, $Q(r) \to x(t), c \to m, -F(Q) \to V(x)$.

Therefore, the order parameter texture at the DW can be thought of as a trajectory $Q(r)$ of a particle in a flipped potential $-F(Q)$, that is connecting the hills of $-F(Q)$ (corresponding to domains = minima of $F(Q)$), as seen in Fig. 4.6(a) and Fig. 4.8(a,b). We discussed above that the structure of the minima in the free energy is affected by the value of the parameter η. The analogy with the classical particle in the flipped potential is useful to understand the case $\eta < \eta_c$, and the following discussion refers to that case.

At $\alpha = 0$, all the barriers along the rim of the Mexican hat have the same height (Fig.4.8(c)) and hexagonal vortex defects with six domains meeting at a vortex line are expected [65]. When $\alpha \neq 0$, three hills of the flipped potential become lower than the other three (cf. Fig. 4.3(c',e') and Fig. 4.6(a)), and the particle starting from the highest hill (minimum of $F(Q)$) arrives at the lower adjacent hill still having positive kinetic energy. Before moving to the next hill it spends some time above the lower one, for example the trajectory with $\alpha = 0.5$ in Fig. 4.8(d). This results in the equivalent particle trajectory $Q(r)$ passing through the intermediate minimum of the free energy (Fig. 4.8(a)). Therefore it leads to an intermediate metastable domain that is as wide in r as the "time" that the classical particle spends above the hill. The result is a wide DW with internal structure that hosts the metastable state inside. The width of the wall critically depends on $|\alpha|$, that determines the energy penalty of the metastable state. Lower values of α result in higher intermediate hills of the equivalent potential (lower intermediate minima of the free energy). The width of the DW decreases with α (Fig. 4.9(b)) until it disappears, resulting in a free energy with only three minima. In these simulations, the minimization was performed on a discrete lattice of 500 elements. As α grows, the minima in the free energy become maxima. This is equivalent to saying that the width of the composite DW

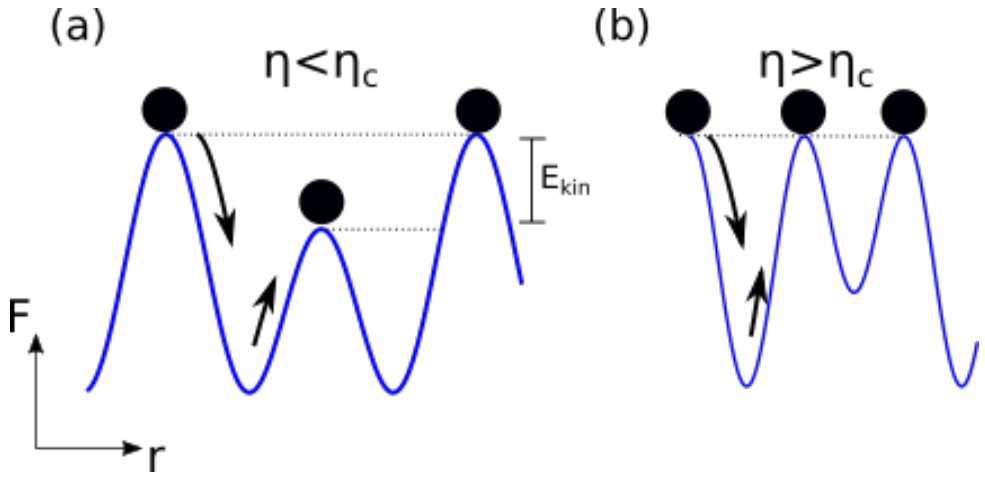

Figure 4.6: Classical particle in a flipped free energy potential in the case (a) $\eta < \eta_c$ (flipped version of Fig. 4.3(c')) and (b) $\eta > \eta_c$ (flipped version of Fig. 4.4(c')). In the (a) case the particle spends a certain amount of time at the top of the low hill, equivalently Q stays in a metastable state. In the (b) case all hills have the same height and so no equivalent metastable state is present.

decreases. Fig. 4.9 shows how the metastable state shrinks as α grows.

In the case with $\eta > \eta_c$, the flipped potential has all the hills of the same height, and if we think in terms of a classical particle rolling down the potential curve, we realize there are no intermediate metastable states. The trajectories between the minima appear to be highly asymmetric as α grows (Fig. 4.10). In this case the domains are ferroelectric, according to Eq. (4.8).

High and low barriers along DW trajectories correspond to high and low DW surface energy. At the phase transition both domain walls may appear, but at lower temperatures the polarization switching will likely be mediated by the nucleation of the domain, separated by a lower barrier. Therefore DWs will form only between minima separated by higher barriers. For example, the pie chart in Fig. 4.7 (b) shows that only DWs between minima 1 and 2 and, by symmetry 3-4 and 5-6, are formed in that phase. In an analogous matter DWs between minima 2-3 and, by symmetry, 4-5 and 6-1 will be formed in the phase (d). At low α (area in green in Fig. 4.7) the six states become degenerate and six-fold vortices are possible. At $\eta < \eta_c$, in a non-ferroelectric state, the three domains become metastable for α away from zero, which results in 3-fold vortices, connecting the deeper energy minima.

Finally, in order to determine the parameters of the model for $(DMA)Fe^{II-III}(COOH)_3$, we perform first-principles calculations. We are primarily interested in the energy surface along the DW trajectories. Therefore, we perform nudged elastic band (NEB) calculations [66] to compute the energy barrier between the neighboring domains, related by the 120° rotation of DMA molecules. Experimental structure [54] was relaxed and used as an initial state, while in the final state the molecules were rotated by 120° around the axis that connects the two Carbon atoms in the molecule.

To connect the initial and final state, we constructed nine intermediate states, in which the molecules were progressively rotated by the same angle, resulting in a total of eleven states, or *images*. This *band* of eleven images is energetically optimized by NEB calculations. During the NEB optimization, the coordinates of ions $\boldsymbol{x}_i$ in the image i, are shifted towards the energy minimum in the direction, normal to the band direction

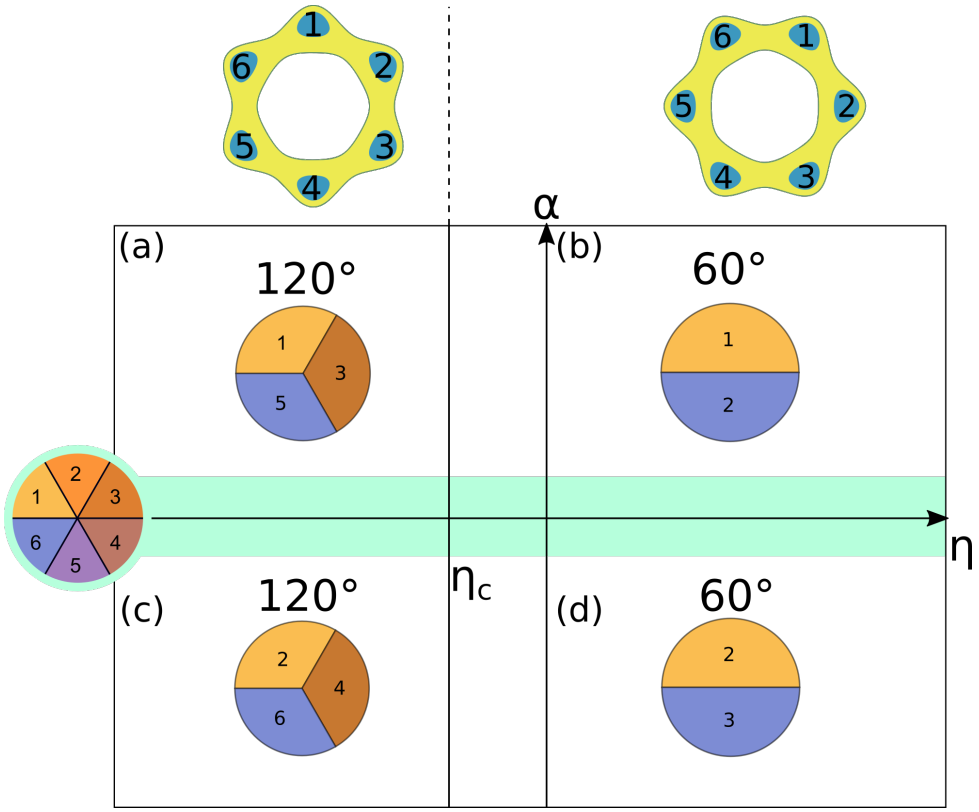

Figure 4.7: The phase diagram of the model Eq. (4.10) and possible topological defects (domain walls and vortices) in the η-α plane. The pie charts indicate the possible defects, with numbers 1-6 referring to the minima, marked on the free energy surfaces at the top. Lines between numbers indicate the energy barrier. Near $\alpha = 0$ the minima are nearly degenerate, leading to 6-fold vortices separated by barriers of the same height. At $\eta > \eta_c$, in states (b),(d), high barriers separate pairs of adjacent pairs of vortices, thus making some DWs very energetically costly. Only one pair is shown in the pie chart for simplicity. The domains are ferroelectric and correspond to 60° rotation of molecules. At $\eta < \eta_c$, in states (a),(c), three of the minima become metastable, thus resulting in three stable domains with zero ferroelectric polarization and 3-fold vortices, corresponding to 120° rotation of molecules.

$\boldsymbol{\tau}_i = \boldsymbol{x}_{i+1} - \boldsymbol{x}_i$. To keep the images from accumulating close to the minima at the endpoints, an energy penalty for separating the neighboring images (breaking the band) is added, $\sim s(\boldsymbol{x}_{i+1} - \boldsymbol{x}_i)^2$, with s the stiffness parameter.

The forces resulting from this energy term are projected on the direction of the band $\boldsymbol{\tau}_i$. This ensures that every image still at the minimum in the direction perpendicular to the band. Therefore, the forces from the neighboring images in the direction perpendicular to the band are removed. Hence, the NEB path does reach the lowest energy points. The force on each image is

$$\begin{aligned} \boldsymbol{f}_i = (\mathbb{1} - |\boldsymbol{\tau}_i\rangle \langle\boldsymbol{\tau}_i|)(-\nabla_{\boldsymbol{x}_i} U(\boldsymbol{x}_i)) + \\ |\boldsymbol{\tau}_i\rangle \langle\boldsymbol{\tau}_i| \, s(\boldsymbol{x}_{i-1} + \boldsymbol{x}_{i+1} - 2\boldsymbol{x}_i), \end{aligned} \tag{4.14}$$

where $|\boldsymbol{\tau}_i\rangle \langle\boldsymbol{\tau}_i|$ is the projector in the direction on the band, and U the energy potential that act on the images. Iteratively descending along this force, we obtain the NEB path that passes through a saddle point between the minima, corresponding to the NEB endpoints.

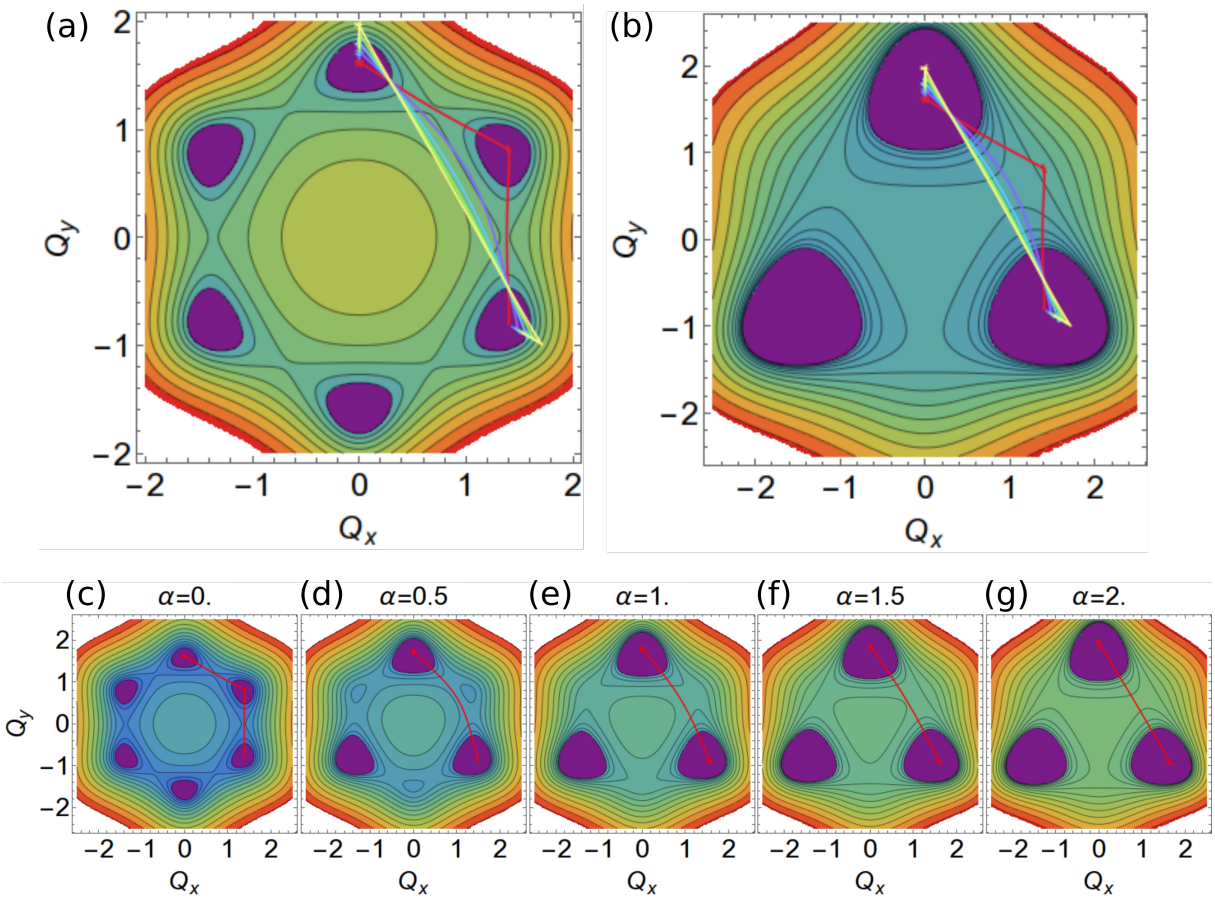

Figure 4.8: The trajectories $Q(\phi)$ for the effective single-particle Lagrangian, shown on top of the energy potential computed in the case $\eta < \eta_c$ (encoded with rainbow color scale).(a,b) Effective classical trajectories (colored lines) reported in panels (c-g) on top of the $\alpha = 0$(a) and $\alpha = 2$(b) energy surface. (c-g) Trajectories (red) computed for different values of α, plotted on top of the respective energy surface.

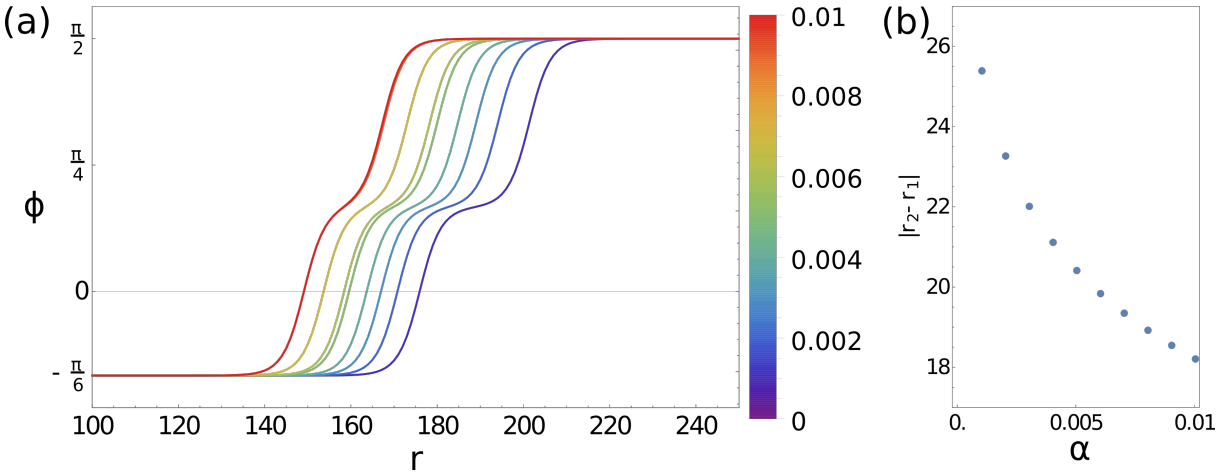

Figure 4.9: (a) The spatial evolution of the trimerization angle $\phi(x)$ across composite DWs. Line colors encode different values of α, as indicated by the color scale on the right. The number on the x axis refers to the discretization elements (sites) used in the simulation. (b) The dependence of the width of the composite DW on the α parameter.

To position one of the images precisely at the saddle point, the "climbing image" method is used: the image j with the highest energy is allowed to move along $\nabla U(\boldsymbol{x}_j)$ so as to reach the local energy maximum. Following the algorithm discussed above we find the lowest energy path for the $Q(r)$.

The NEB calculations were performed using the energy surface $U(x)$ from first-principles, as implemented in the Quantum Espresso code [67, 68], which uses the same lattice parameters for all images. This precludes the unit cell from deforming, while such deformations may lower the energy barrier for molecular rotations. Therefore we expect to obtain an upper estimate for a barrier in the real material.

Since the initial structures were prepared by rigidly rotating the molecules from $\phi = 0$ image around C-C line, the energy of image 11 was initially higher (because in reality the molecules rotate around a slightly different axis). Therefore the rotation we imposed can be though of as a rotation around the correct axis followed by a shift. This shift leads to an increase in energy, but is mostly eliminated during the relaxation. The barrier is estimated at around 0.3 eV per formula unit, and has a strong asymmetry between states $\phi = 0$ and $\phi = \pi/3$, corresponding to images 1 and 7, reflecting the coalescence of minima, seen e.g. in Fig. 4.10(c,d). The asymmetry of the barrier results in an asymmetric path for $Q(\phi)$. This implies $\eta > \eta_c$ in (DMA)$Fe^{II-III}(COOH)_3$. Calculations suggest that the anisotropy strongly disfavors the $\phi = \pi/3$ metastable state, so the DW may not be wide, but the corresponding local minimum does not disappear completely. This suggests an upper estimate of $\alpha = 0.25$ eV for Fe-MOF. Given a large number of atoms in the simulation (222 atoms) and no strain relaxation, the actual barrier is likely lower than our estimate, leaving the possibility for wider DWs. A large α would result in a small polarization.

The presented model describes improper ferroelectricity in (DMA)$Fe^{II-III}(COOH)_3$, driven by the order of the organic molecules. We also discussed topological defects (hexagonal and triangular vortexes) possible in this model.

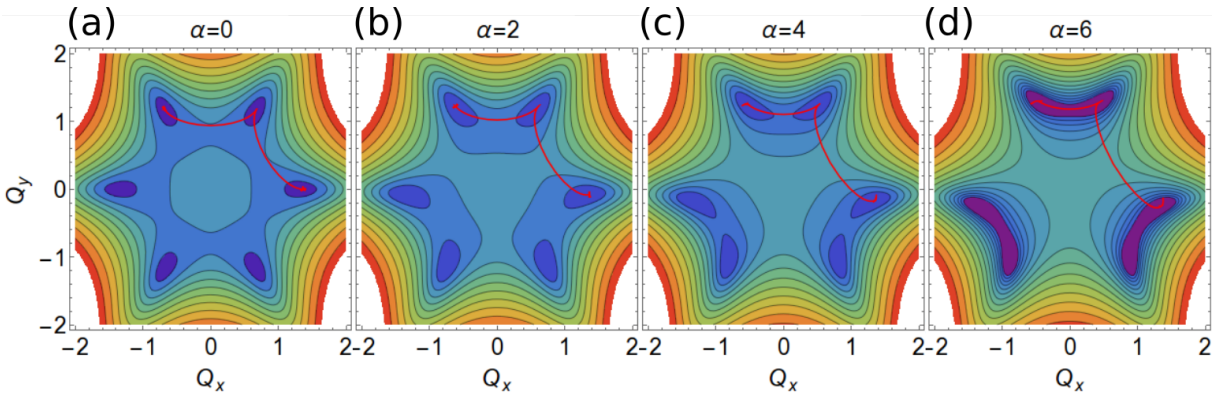

Figure 4.10: The trajectories $Q(\phi)$ for the effective single-particle Lagrangian, shown on top of the energy surface, computed in the case $\eta > \eta_c$ (energy encoded using rainbow colorscale). Trajectories (in red) are computed for different values of α and plotted on top of the respective energy surface.

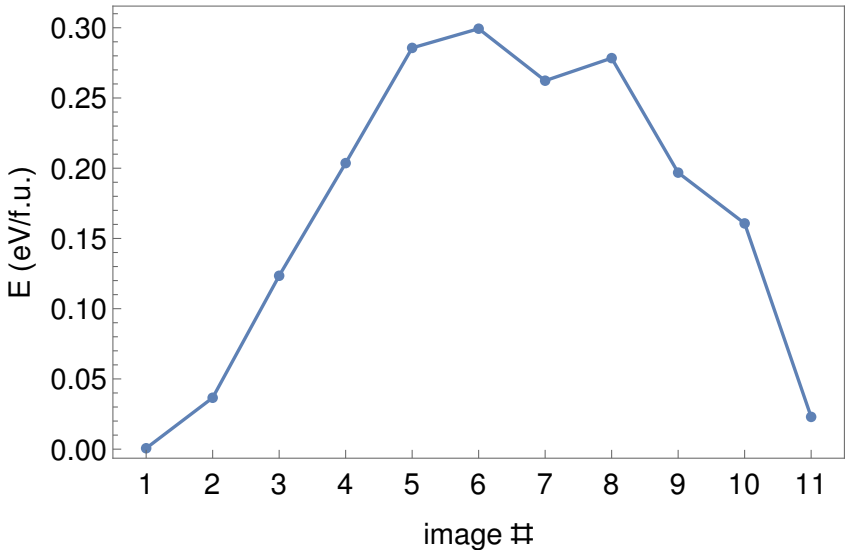

Figure 4.11: Energy barrier for the molecular rotation mode as computed with nudged elastic band method with 11 images using Quantum Espresso code. The first and last images correspond to $\phi = 0$ and $\phi = 2\pi/3$, respectively. The initial structures for the images were prepared by rotating the molecules rigidly around the line connecting two carbon atoms.

4.6 Conclusions

We performed a symmetry analysis and derived a Landau-type theory describing molecular ordering and ferroelectric polarization in perovskite-based MOFs. The results suggest a new mechanism of improper ferroelectricity in these materials, that is related to unit cell tripling molecular order. The symmetry aspects are reminiscent of those in hexagonal manganites and ferrites, but the theory has an additional term that makes domains of opposite polarizations inequivalent. When the term is small, wide composite DWs, hosting the intermediate metastable phase, appear. First-principles estimates suggest high barrier, narrow DWs and small polarization in Fe-MOF.

Chapter 5

Theory of Devil staircase in $IrTe_2$

5.1 Introduction

Throughout this Thesis we described many different systems, usually relating them to real materials. In each case the peculiarities and unique properties of such systems have been studied. Despite the great variety in the objects of our study, a unifying theme of this work has been consistently present in every part of this Thesis: if an order emerges, the properties of the system will be affected. Up to this point the reader may be accustomed to such a notion, but nonetheless, it is important to highlight the relevance of this concept in introducing the following Chapter.

In this work we will investigate an uncommon ordering mechanism that characterizes the transition metal dichalcogenide $IrTe_2$. All materials belonging to this class have the common MX_2 structure, where M represents a transition metal atom and X is an anion from the chalcogen group, the 16th group that is represented by Oxygen (although Oxygen is often considered separately). Typically the most utilized chalcogens are S, Se, and Te.

In our specific case, $IrTe_2$, a striped dimerized structure is observed [69]. Below 280 K the Ir-Ir bonds can shorten up to 20-25% of their length. The resulting dimers are arranged in a regular pattern in the crystal [70].

$IrTe_2$ has attracted interest in the recent years due to its unusual temperature-induced ordering. As well as exhibiting superconductivity upon doping, with the phase diagram reminiscent of high-T_c cuprates [71, 72]. The problem of describing and characterizing the mechanism that generates dimerized states is not fully understood to date and will be the main focus of this Chapter.

The structure of the Chapter is the following: we start with a general overview of the material, highlighting the properties that make $IrTe_2$ a compelling object of study and point out the open questions. We then proceed to discuss our analysis: first-principles calculations on different dimerized states reveal the relation between the total energy of the system and the dimerized states. Rationalizing these results provides useful information about the stability of different dimerized states. By making some general assumptions about the dimer energy, and free energy, and the dimer-dimer interactions, we arrive to a minimalistic model for the free energy that captures the phase transitions and the schematic phase diagram is obtained. Finally we elaborate our conclusions, describing our understanding of the dimerization mechanism and stability of particular dimerized states.

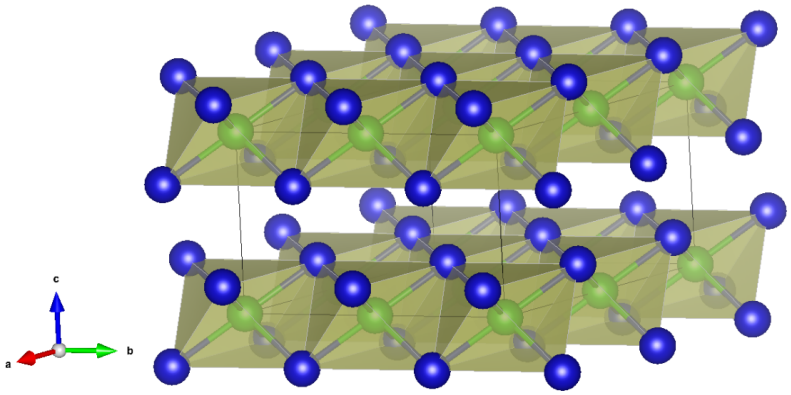

Figure 5.1: Layered structure of $IrTe_2$, Te in blue and Ir in green.

5.2 The material

$IrTe_2$ is a transition metal dichalcogenide. This class of materials is identified by the common structure MX_2, where M is a transition metal atom and X an anion from the chalcogen group. All compounds in this group exhibit a layered structure, with Van der Waals interactions between triple layers. Each triple layer is generally constituted by a triangular lattice of transition metal atoms between two planes of chalcogen atoms ordered accordingly to the particular structure of the material. This macro group attracts attention for many different reasons, for example the great variety of transition metals provides a conspicuous number of interesting and unstudied materials. The layered structure of the compounds allows for the exfoliation and study of separate 2D layers, which often host rich physics and new phenomena. Moreover, strong spin-orbit coupling (SOC) is often present in these materials, and the transition metal-based triangular lattice opens the possibilities for frustrated magnetic interactions, or exotic spin states [73].

$IrTe_2$ in particular exhibits 1T structure, $P\bar{3}m1$ (#164 in the International Tables). In the unit cell the Ir cation is centered in an octahedron formed by 6 Te atoms. Edge-sharing octahedra form a layer and different layers are connected by the Te-Te interactions, which in this material have covalent character (Fig 5.1). At room temperature $IrTe_2$ is a metal with the structure we described above. In this phase the oxidation states of the atoms are nominally Ir^{3+} and $Te^{1.5-}$. As the material is cooled down it is possible to observe dimerization between Ir atoms, resulting nominally in Ir^{4+}-Ir^{4+} dimers and Te^{2+} atoms at the corners of the octahedra. The low temperature phase emerges through the introduction of stripes of Ir-Ir dimers in an originally undistorted layer of high temperature structure. Similar to other transition metal dichalcogenides, $IrTe_2$ has a dome-shaped superconductive phase diagram [74, 75], where the superconductive phase competes against the striped order and may be stabilized by suppressing the striped order with chemical doping or thinning of the sample [72]. While the phase diagram containing dimerized phases has not been modeled so far, several driving forces that may lead to dimerized states have been hypothesised. Charge ordering, bonding instabilities [76], and Piers instability [77] have been proposed. Immediately below the phase transition temperature (270-280 K) the stripe order appears with a modulation vector of $(1/5, 0, -1/5)$. However, upon further cooling the ordering of the dimer phases changes and phases with modulation vectors of the form $(1/n, 0, 1/n)$ appear [78]. All observed states are still metallic but the phase

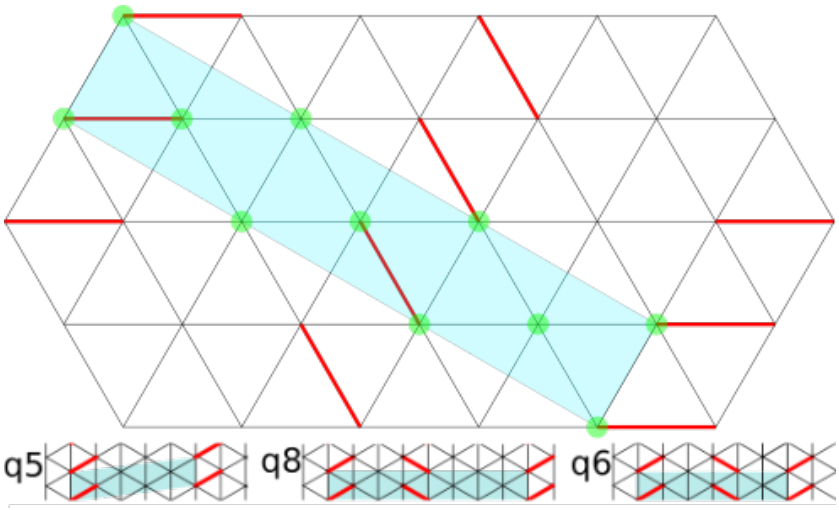

Figure 5.2: (Top) Hexagonal lattice of Ir atoms and dimer stripes (in red) for q_6 state. The light blue rectangle represents the periodic cell in these dimerized phases. Ir atoms in the cell are highlighted in green. In total, 6 Ir atoms and two dimers are contained in the cell, therefore giving a ratio dimers to Ir ions of 2/6. (Bottom) Schematic structure of q_5, q_8 and q_6 phases rotated by 30°.

diagram has not been fully established due to experimental difficulties of discerning the various phases, although scanning tunneling microscopy may be a promising technique to tackle this challenge [79].

In the following section we rationalize the DFT energetics of dimers to build a basis for the description of the mechanism, responsible for dimer pattern formation.

5.3 Dimer energetics

As mentioned in the preceding section, $IrTe_2$ undergoes a phase transition around the temperature of 270-280 K, switching from the regular structure described in figure 5.1 to a phase where Ir-Ir dimers appear arranged in conglomerates of dimers, in the form of stripes. As the temperature is decreased, the periodicity of the stripe pattern changes. In this striped order it is possible to identify a periodic structure, formed by dimers and undimerized Ir atoms. The fraction of dimerized rows grows with decreasing temperature. These different stripe orders have been observed [70] for decreasing temperatures and characterized by wave vectors of $[(1/(3n+2), 0, 1/(3n+2)]$ with integer n. We will see later how this ordering mimics a staircase-like phase diagram which we will refer to as a "Devil Staircase" [80], a picturesque name due to the fact the the number of steps keeps growing as the top of the staircase is approached.

We will classify the different phases according to the denominator $3n+2$ of the wave vector of the phase. Fig. 5.2 shows an example of q_6 state (formally corresponding to $n = \infty$) while also showing in less detail the q_5 and q_8 states. It is worth mentioning that the number $3n+2$ is also the number of Ir atoms in the periodic cell that identify that phase.

5.3.1 First-principles analysis

In this section we approach the problem of the stability of the dimerized phases: different temperatures stabilize phases with a different dimer-to-Ir ratio. Stable up to 280 K, q_5 is the phase characterized by the highest onset temperature. We would like to compare the free energies of different phases to establish a hierarchy, and to reproduce the ground state and phase diagram of the system. DFT was used to model the transition between q_5 and q_8 states, by comparing the free energies of these states, accounting for the phonon entropy contribution to the free energy, computed in the harmonic approximation [81]. However, this approach is increasingly difficult for lower-T states since it requires phonon calculations for large cells within meta-GGA and with SOC included. Even reproducing the energy ordering of the dimerized states at $T = 0$ has been shown in literature [70] to be no trivial task since it requires the inclusion of SOC (that is large for both Ir and Te), and the use of meta-GGA (since commonly used exchange-correlation functionals are unable to reproduce dimer stabilization).

Experimentally, the phases with the dimer fraction given by $n/(3n + 2)$ are observed, with n taking sequential integer values starting from 1 with the decreasing temperature. Calculations of the zero-T total energy of three dimerized states, q_5, q_8 and q_6, [81] are summarized in Fig. 5.3, which shows the total energy dependence on the dimer fraction. Different exchange-correlation functionals have been used, including PBE, PBEsol and meta-GGA M06L with and without SOC. It can be seen that often used exchange-correlation functionals, such as LDA, PBE and PBEsol, are unable to stabilize dimerized states (or at least unable to stabilise the q_6 state at $T = 0$ K). In previous DFT work authors [70, 82] have turned off spin-orbit coupling to artificially stabilize the dimers, but that is not justified. In fact the Ir-z^2 orbitals are the most conducive to Ir-Ir bonding, while also having zero orbital angular momentum, and therefore are reconstructed by SOC. Calculations using meta-GGA functionals with spin-orbit included correctly capture the energy decrease with the increasing number of dimers [81]. This trend is consistent with experimental [70] observations of q_5 ($n = 1$) being the first dimerized phase immediately after the high temperature (HT) state and q_6 ($n \to \infty$) the ground state. The hierarchy of dimerized states is successfully predicted by the meta-GGA based M06L and SCAN functionals when SOC is accounted for. It is important to highlight that the behaviour of energy is almost linear with the dimer fraction, except for a small quadratic correction, cf. Fig. 5.3. This correction can be interpreted as a repulsive interaction between dimerized rows.

In the second part of the numerical analysis we model the dimer-dimer interaction, and provide a possible explanation for the striped order in $IrTe_2$. The reasons behind the peculiar dimer patterns are poorly understood. Here we propose that strain-mediated dimer interactions are the key to these particular dimer arrangements.

In solids, distortions interact via strains and optical phonons, which are also induced by strains, [83, 84]. These distortions are induced, for example, from Jahn-Teller instabilities, charge and orbital ordering, and by substitutions of ions in a lattice. Such interactions between the distortions lead to stripes in doped manganites. As far as strains are concerned, dimers act as ellipsoids inserted in a spherical pore cut in a material [83]. While the induced optical mode amplitudes decay exponentially away from the source of the disturbance, strains decay slower, following a power law. In order to investigate the elastic interactions between dimers in $IrTe_2$, we pick one Ir-Ir bond (highlighted in cyan in Fig. 5.5(z=0)), induce its infinitesimal contraction, and compute the forces on other Ir-Ir bonds by utilizing an ab-initio force constant matrix for HT phase. The contracting

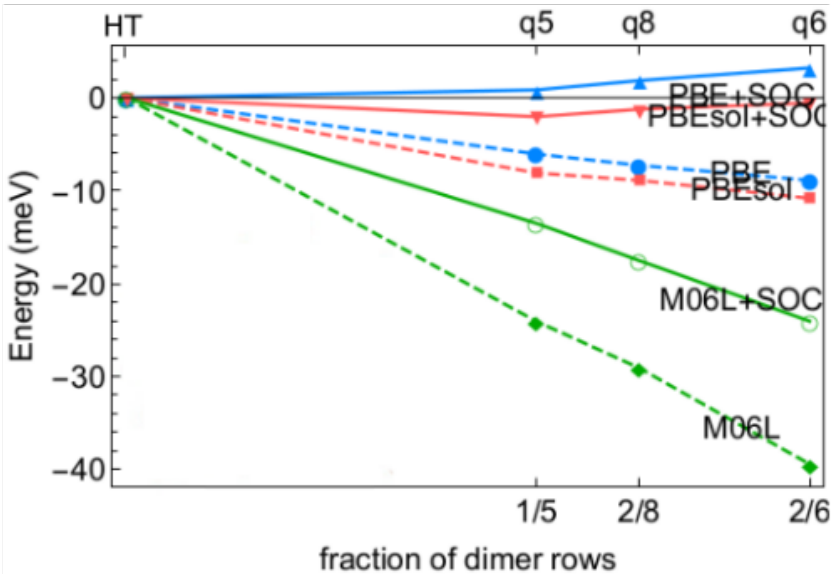

Figure 5.3: Computed total energy as a function of different dimer-Ir ratios. The state q_6 is correctly identified as the lowest energy state for the M06L exchange functionals (both with and without SOC). However PBE and PBEsol cannot stabilize q_6 in presence of SOC

bonds are marked in red, while the expanding ones are shown in violet in Fig. 5.5. Once one dimer has nucleated, it is favorable to create the next one in such a way as to minimize the elastic energy. The contracted bonds (red), are parallel to the initial dimer and tend to be distributed mostly along two particular directions, shaded in grey in Fig. 5.5. The elongated bonds (violet) lie on the direction of the initial dimer, consistently with the discussion in Ref. [83]. This leads to the repulsive interactions of dimerized rows. Our calculations show that if dimerized rows are close enough, strong repulsion arises. This also explains why in q_6 state dimers in the neighboring rows are not parallel to each other, but have alternating orientations.

The wave vectors in all the experimentally observed dimerized phases are along the $(1, 0, -1)$ direction. Equal ab-plane and c-axis components of the wavevectors in all phases is counterintuitive, as the material is layered and hence very anisotropic. The stacking of Ir-Te-Te-Ir layers gives rise to the forces on the bonds in the neighboring layers as well. This particular stacking leads to the stripes of favored dimers in $z = \pm 1$ layers, shifted in the ab plane with respect to the stripes in $z = 0$ layer, as seen in Fig. 5.5. This explains the peculiar orientation of the wave vectors in the observed dimerized phases, $(1/n, 0, -1/n)$.

5.3.2 Finite temperatures – free energy

In this section we are going to address the problem of equilibrium states of $IrTe_2$ at finite T, building on the dimer energetics and their interactions discussed above. In summary, Fig. 5.3 suggests that the energy of dimerized phases is mostly linear with the dimer fraction N, with an additional quadratic correction that we can express, with appropriate coefficients, as $E = -\mu N + \alpha N^2$. This term takes into account the energy gain on dimer formation (μ) and the elastic repulsion between dimer rows (the term with α). At finite temperature, the equilibrium states minimize the free energy $F = E - TS$. We

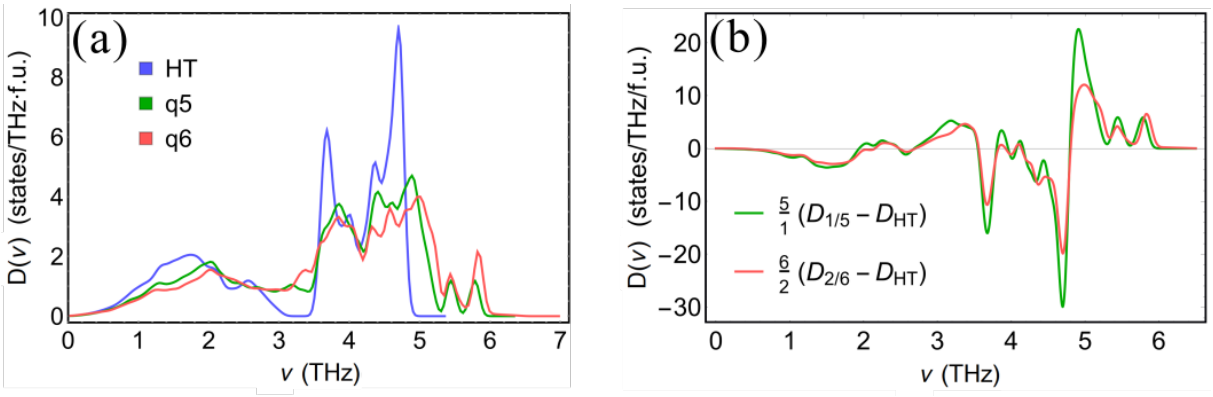

Figure 5.4: (a) Phonon density of states for high-T, q_5 and q_6 phases of $IrTe_2$ from meta-GGA+SOC calculations [81]. Dimer-localized high-frequency phonons are seen above 5 THz for dimerized states. (b) Differences in the phonon DOS between dimerized (q_5 and q_6 states) and high-T state, normalized by the dimer fraction ("phonon DOS change per dimer"). The similarities between the two curves suggest that the dimer phonon DOS can be approximated by contributions of independent dimer rows.

aim to derive an approximate expression for the free energy as a function of temperature and the dimer fraction N.

To obtain the expression for the free energy of the system we must consider the entropic contributions. Since dimers represent stiffer bonds, they host higher-energy phonons. Therefore, dimerization leads to the transfer of phonon DOS to higher frequencies, and to the changes in phonon entropy. This mechanism is responsible for phonon entropy driven phase transition in Sn [85]. Another possible entropic contribution comes from electrons. Modulated states in $IrTe_2$ unlikely result from Fermi surface nesting, as states with many different wave vectors are observed. It is unlikely that the Fermi surface is nested for all these wave vectors. Therefore, in our simplified treatment we neglect Fermi surface contributions to the entropy.

We now discuss the modifications of the phonon DOS in the dimerized states, and extrapolate these modifications to build a more general model. DFT calculations have been performed in order to compute the phonon density of states (DOS) of the dimerized phases as well as the HT one. Figure 5.4(a) shows the phonon spectral weight computed with frozen phonon methodology [81] for the q_5, q_6 and HT phases. Dimerized states possess high frequency phonons above 5 THz. As dimers correspond to stiffer bonds, the phonons, localized on rows of dimers, are harder. Hence the spectral weight is transferred from lower to higher frequencies, affecting entropy. Figure 5.4(b) shows the phonon DOS modification per dimer between HT→q_5 and HT→q_6. The two curves are rather similar despite being based on the states with the lowest (q_5) and the highest (q_6) dimer fractions. This motivates an approximation, where the DOS dependence on the dimer fraction is linear and given by the average of the two curves Figure 5.4(b).

Let $E_N(T)$ be the phonon energy for the systems and S_N the associated entropy. We can write N-dependent free energy for $IrTe_2$ as

$$F(N) = -\mu N + \alpha N^2 + E_N(T) - TS_N. \tag{5.1}$$

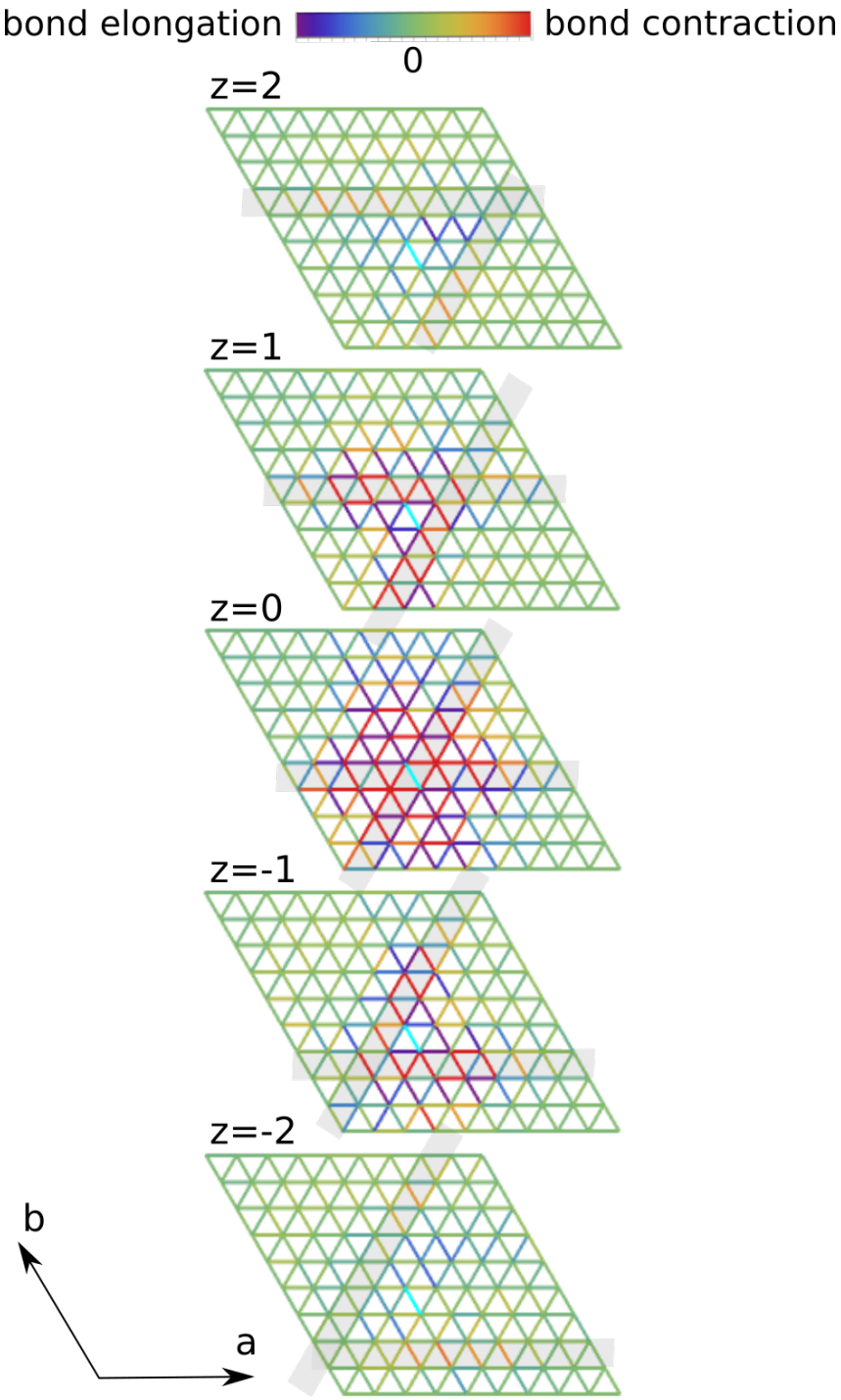

Figure 5.5: Dimer-dimer interactions from first principles: colors encode forces on Ir-Ir bonds resulting from contraction of a single bond (marked in cyan in $z = 0$ layer; cyan marks kept in other layers as a guide to the eye) in the high-T structure. Adjacent layers along the c-axis are shown separately for clarity. Forces are computed from a meta-GGA force constant matrix for high-T structure. Dimerizing red-colored bonds in rows shaded in gray will reduce the energy, therefore once one dimer is nucleated, the dimerized rows grow along one of the gray lines. Peculiar stacking of favored rows accounts for the wave vector of the form $1/n, 0, 1/n$. Bonds in violet, adjacent to the contracted bond, indicate repulsion between neighboring dimerized rows.

In an harmonic approximation the last two terms are rewritten as

$$\begin{aligned} E_N(T) &= \int dE D_N(E) E \left(\frac{1}{2} + \frac{1}{e^{\frac{E}{k_B T}} - 1} \right), \\ S_N &= \frac{1}{2T} \int dE D_N(E) E \left(\coth \frac{E}{2k_B T} - \log \left[2 \sinh \frac{E}{2k_B T} \right] \right). \end{aligned} \tag{5.2}$$

Our choice of units is such that $\hbar = 1$ and $k_B = 1$; $D_N(E)$ is the DOS of the system for a certain dimer fraction N; the Bose-Einstein distribution can be recognized in the expression for $E_N(T)$. Eq. (5.1) can be rewritten as

$$F(N) = -\mu N + \alpha N^2 - T \int dE D_N(E) \log \left[2 \sinh \frac{E}{2k_{\mathrm{B}} T} \right]. \tag{5.3}$$

A further simplification is possible if we try to separate in the DOS the contributions of the dimer phases from the HT phase. We can now show that the dimer contribution to the DOS is proportional to the dimer fraction N. The proof of this is performed by considering Fig. 5.4(b). When we subtract the DOS of the HT phase from the DOS of a dimerized state and normalize the result, we obtain the single-dimer contribution to the DOS. Figure 5.4 shows that the two redefined DOS are really similar, thus the contribution of a dimer phase to the corresponding DOS is in good approximation proportional to N. We rewrite the regular DOS separating the contribution that is linear in N and the HT one

$$D_N(E) = N D_d(E) + D_{HT}(E) \tag{5.4}$$

where $D_d(E)$ is a generic single dimer contribution, then the free energy assumes the following form

$$\begin{aligned} F(N) = -\mu N + \alpha N^2 - NT \int_0^{E_{\max}} dE D_d(E) \log \left[2 \sinh \frac{E}{2k_{\mathrm{B}} T} \right] \\ -T \int_0^{E_{\max}} dE D_{HT}(E) \log \left[2 \sinh \frac{E}{2k_{\mathrm{B}} T} \right]. \end{aligned} \tag{5.5}$$

$E_{\max}$ is a cutoff energy we introduce by observing the phonon DOS in Figure 5.4(a). There are no phonons above a certain frequency $\nu = 6$ THz, and $E_{\max} = h\nu$. The aim of this section is to predict the phase diagram of the dimerized phases, i.e. for a certain dimer fraction N to know the associated temperature. In order to do so we compute the free energy for different values of N, before and after a phase transition, and by equating the two expressions we obtain the phase transition temperature. In this regard we can neglect the last integral in the expression (5.5) as it is not N-dependent. We also notice that the second integral does not depend on the temperature and thus will result into a number with the dimensions of entropy. We can therefore define the single-dimer entropy as

$$S_d = \int_0^{E_{\max}} dE D_d(E) \log \left[2 \sinh \frac{E}{2k_{\mathrm{B}} T} \right], \tag{5.6}$$

expression (5.5) becomes

$$F(N) = -\mu N + \alpha N^2 - NT S_d(T). \tag{5.7}$$

The maximum frequency $\nu = 6$ THz translates into an effective temperature of $\Theta = \hbar\nu/k_B \approx 290$ K. As the phase transitions we are considering occur at lower temperatures than Θ, and all phonons have lower frequencies than ν it results that the quantity $E/2k_B\Theta$ is small. We can expand the logarithmic term in the Eq. (5.6) so that it becomes $\log E/k_BT$. Up to a constant, the entropy per dimer takes the form

$$S_d = \int_0^{E_{\max}} dE D_d(E) \log\left(\frac{E}{\Omega}\right), \tag{5.8}$$

where $\Omega = 1$ eV is only introduced for dimensional consistency and does not change S_d since dimerization does not change the total number of ions (and hence phonons), $\int_0^{E_{\max}} dE D_d(E) = 0$. This approximation results in a simple expression for the phase transition temperatures. If N_1 and N_2 are the two dimer fractions for consecutive phases, $N_1 = N(n)$, $N_2 = N(n+1)$, with $N(n) = n/(3n+2)$ being the experimentally observed dimer fractions, the transition temperature T_{12}, obtained from $F_{N_1}(T_{12}) = F_{N_2}(T_{12})$, is

$$T_{12} = \frac{-\mu + \alpha(N_2^2 + N_1^2)}{S_d}. \tag{5.9}$$

We thus arrive to the phase diagram of the material, shown in Figure 5.6. The transition temperatures are computed using Eq. (5.9) and accurately reproduce the results of the more complex calculations based on the DOS from DFT calculations with meta-GGA exchange-correlation functionals and SOC included. Pressure dependence can be incorporated in the free energy by adding the $F_P = -PV$ term. Since dimerized rows are narrower, each dimerized row reduces the lattice constant, resulting in a linear volume dependence on the dimer fraction, and thus $F_P = -P(V_0 - \gamma N)$. This leads to extra stabilization of the dimerized phases by pressure. The effects of doping are also affecting the stabilization energy of the dimers μ, thus also contributing to the linear N term in the free energy. Therefore we expect the phase diagram in the temperature-doping plane to be similar to that in the T-P axes.

5.4 Conclusions

To summarize the content of this chapter, $IrTe_2$ is a transition metal dichalchogenide, which shows a plethora of dimerized metallic phases and superconducting dome in the temperature-doping plane. Among the peculiar properties of this material we focus on the series of striped states, where Ir-Ir atoms are dimerized. The problem behind the origin of the dimerization is still a fascinating one, despite over a decade of active research. In particular, (1) the reasons behind the peculiar dimer patterns are not well understood, (2) it is not clear what determines this particular direction of the wave vector and (3) a model that would predict the phase diagram is not available.

We rationalize the results of first-principles simulations and derive a simplified model that addresses these questions. The energy of dimerized phases is mostly linear in the fraction of dimerized rows, with non-linear terms describing the repulsion between dimerized rows. Strain-mediated interaction between dimers are computed. The results are compatible with the observed appearance of dimer stripes (analogous to those in doped manganites), as well as the direction of the wave vector $(1, 0, 1)$. Dimers result in high-frequency phonon modes, absent in the spectrum of the HT phase, leading to a reduced entropy and

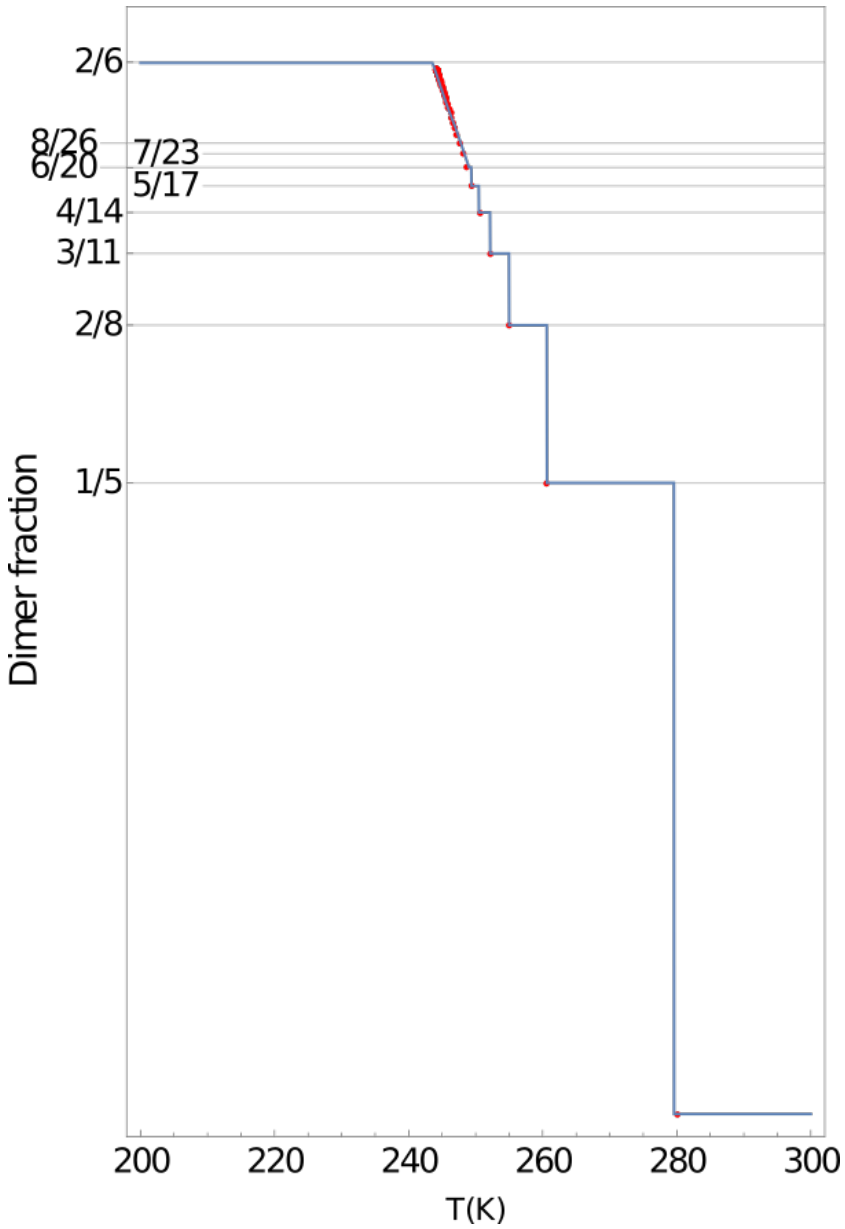

Figure 5.6: Phase diagram of $IrTe_2$: fraction of dimers as a function of temperature. The blue solid line is computed using the phonon spectrum obtained from DFT. Red dots are a fit with Eq. (5.9). The lowest solid line corresponds to HT phase, containing no dimers.

potentially opening new channels for phonon-mediated phenomena and phonon-based devices. We also showed that the contribution to the DOS is linear in the fraction of dimers N, corroborating the hypothesis of weak interaction between dimers. Finally, combining dimer energetics and the harmonic approximation for phonon entropy, we predict an idealized phase diagram (neglecting hysteresis). The computed phase diagram contains an infinite number of states, analogous to the case of the famous "Devil's staircase".

While the computed dimer-dimer interactions provides insight into the specific ordering of the dimers in stripes, it does not explain all the features of striped structures. More questions regarding this material are still open, e.g. it is not clear why the observed dimer fractions follow the peculiar $n/(3n+2)$ law. The competition between stripes and superconductivity may need further research. Further work may be needed to establish the quantitative pressure-doping-T phase diagram. This approach, which quantifies dimer energetics and interactions thermodynamics, is therefore a powerful tool in understanding these materials. It is our hope that this work will stimulate future research and better understanding of the fascinating physical mystery of structural incommensurate phases.

Chapter 6

Conclusions

In this Thesis we considered a number of diverse problems of recent interest, under the overarching theme of interacting orders and modulated states, and addressed them in a detailed and consistent way. The diversity of these problems, while requiring a variety of theoretical tools, allows to build connections between different topics and form a broader perspective. Different problems require different methodologies to be solved, but microscopic models, symmetry arguments, and energetic considerations proved to be general principles that guided us throughout this Thesis to develop adequate methods and tools to tackle every problem.

In Chapters 1 and 2, we studied the magnetic properties of non-collinear spin systems. In Chapter 1 we addressed the problem of identifying elusive magnetic monopoles and toroidal moments and proposed their existence in hexagonal manganites and ferrites. These compounds attract interest due to their multiferroic properties. We also formulate experimentally verifiable predictions, that could help identify the monopolar and toroidal states. We achieved this by formulating an adequate microscopic model that captures these peculiar orders. The model reproduced experimental inelastic neutron scattering data on $LuFeO_3$ and predicted the experimental signatures to be expected in the presence of magnetic monopoles or toroidal moments. Incidentally we demonstrate the non-reciprocal magnon propagation in the material that has not been previously reported. These results should guide experimental identification of these peculiar states.

In Chapter 2 we addressed the reason behind the large-valued dielectric constant in spiral magnets. In particular, we hypothesised that soft domain wall-related excitations may be responsible for the dielectric anomalies. We utilized a model and a set of analytical tools similar to those used in the previous chapter. We studied the effects of magnetic excitation in a spiral configuration, and we evidenced the connection between soft DW-localized modes and the static dielectric constant. Our model predicts electromagnons inside spiral magnets and describes the ME effect. This results open a great number of possibilities for controlling the dielectric properties of spiral magnets through the manipulation of DWs.

In Chapter 3 we discussed the phase-dependent thermal conductivity in GaV_4S_8. trMOKE measurements on GVS reveal a factor of two in the change of thermal conductivity when the magnetic phase of the material (FM, Cyc, and SkL) changes under external magnetic field. In order to explain the behaviour of the thermal conductivity, our atomistic spin dynamics simulations suggest that abundant chiral domain walls are created upon the transition to the spiral state. The associated scattering of magnons off the domain walls explains why switching between different magnetic phases affects the

thermal conductivity. Similar materials with easily switchable magnetic phases can pave the way for magnon-mediated heat control technologies. We also simulated the photoexcitation process of coherent magnons and the change in the magnetization that follows the excitation. This method allowed us to study the coherent magnon dynamics in the material.

Chapter 4 investigated the origin of ferroelectric polarization in MOFs through ordering of the organic molecules. In this case we considered a different type of approach. The structure of the organic-inorganic material framework is very complex and is therefore less suitable for an accurate microscopic model, hence we adopted a phenomenological approach. We describe the appearance of the polarization with a Landau-type theory of phase transitions. The model explains how the improper ferroelectricity results from molecular ordering and predicts a rich phase diagram that can be generalized in order to describe other MOFs. Our results will guide the research toward the realization of new organic-based ferroelectric materials.

In Chapter 5 we analyzed the peculiar valence bond solid states in $IrTe_2$. Different hypotheses have been proposed to explain the dimer formation but no model for the stripe patterns has been put forward. We analyze the material by combining ab-initio calculations and a generalized model of the free energy of the system. The first-principles results on dimer energetics and harmonic phonon entropy are the starting point for a minimal model of the free energy of the system. We use this model to predict the phase diagram of the material, that has the peculiar shape of a "Devil's Staircase", with infinite number of dimerized phases. In experimental measurements, hysteresis may inhibit the experimental detection of the narrower phases, which may still be seen at surfaces in STM-based measurements. We hope this first model of the phase diagram of $IrTe_2$ will enable future studies of valence bond solid states in this and similar materials.

To conclude, this Thesis has been dedicated to a wide set of problems in materials with complex orders, such as non-collinear magnetism, ferroelectricity, and structurally modulated states. Particular attention has been directed to multiferroic materials, with more emphasis on the magnetic properties of these. The study of magnetic excitations is, in fact, a field of great interest both from the application point of view and from the pure theoretical side. We hope that our work can help in understanding of dynamics and magnetic excitations in fascinating non-collinear spin systems. We also explained how electric dipoles originate from molecular ordering in the MOF and how electromagnons arise in materials where electric and magnetic degrees of freedom were present, as in cycloidal spiral magnets. These projects are particularly important due to the polarization oscillations being strictly tied to magnons, in the case of the spiral ordered materials, or to the ordering of organic molecules, in the case of MOF. This provides further insight in the study of electrically controlled phenomena.

We plan to further analyze the results of some of these projects. The most interesting questions that we want to answer regard how the monopolar and toroidal states described in Chapter 1 evolve in time, or how they are affected by the presence of DWs. Another fascinating problem that requires additional work is the motion of a chiral DW under external electric field. We hope the results, presented here, could help the research move forward towards a better comprehension of the physics we studied.

Appendix A

List of abbreviations and acronyms

AFM: Antiferromagnetic

Cyc: Cycloidal

DFT: Density Functional Theory

DOS: Density of states

DM: Dzyaloshinskji-Moriya

DMA: Dymethilammonium

DW(s): Domain Wall(s)

FM: ferromagnetic

GVS: GAV_4S_8

HT: high temperature

INS: inelastic neutron scattering

LLG: Landau-Lifshitz-Gilbert

ME: magneto-electric

MIM: microwave impedance microscopy

MOFs: metal organic frameworks

NN: nearest neighbour

NNN: next nearest neighbour

PM: paramagnetic

RHS: right hand side

SkL: Skyrmion Lattice

SOC: Spin-orbit coupling

trMOKE: time-resolved magneto-optical Kerr effect

Appendix B

Calculation of the magnon spectrum

B.1 Magnon dispersion relation

In this section we show how to compute the magnon spectrum such as the one reported in chapters 1 and 2. We start from a general hamiltonian for a 2D NxN spin lattice with easy ($\hat{\mathbf{n}}$) and hard ($\hat{\mathbf{z}}$) axis anisotropy. We do not include DM interaction only for simplicity, periodic boundary conditions will be used

$$H = J \sum_{i,j,i',j'}^{N} S_{i,j} S_{i',j'} - h \sum_{i,j}^{N} |S_{i,j}^{\hat{\mathbf{n}}}|^2 + k \sum_{i,j}^{N} |S_{i,j}^{\hat{\mathbf{z}}}|^2 \tag{B.1}$$

where J is the spin coupling, h the hard anisotropy constant and k the easy one, i and j are the lattice indexes. We will neglect in further expression the superscript N. For simplicity we only consider NN interaction, we suppose an hexagonal lattice it is possible to express the previous Hamiltonian in a more explicit form

$$H = J \sum_{i,j} \Big[S_{i,j} (S_{i+1,j} + S_{i,j+1} + S_{i+1,j-1}) \Big] - h \sum_{i,j} |S_{i,j}^{\hat{\mathbf{n}}}|^2 + k \sum_{i,j} |S_{i,j}^{\hat{\mathbf{z}}}|^2 \tag{B.2}$$

where we are considering the spin $S_{i,j}$ only to interact with three out of six neighbours, this will make the expression shorter but the reader must keep in mind that, sometimes, it will be necessary to sum over the sites we are not considering. We then express the spins in spherical coordinates:

$$S_{ij} = (S_{ij}^x, S_{ij}^y, S_{ij}^z) = (\sin\theta_{ij} \cos\phi_{ij}, \sin\theta_{ij} \sin\phi_{ij}, \cos\theta_{ij}) \tag{B.3}$$

the generic spin product in eq. (B.2) becomes

$$S_{ij} S_{kl} = (\sin\theta_{ij} \cos\phi_{ij} \sin\theta_{kl} \cos\phi_{kl} + \sin\theta_{ij} \sin\phi_{ij} \sin\theta_{kl} \sin\phi_{kl})\, \hat{\mathbf{s}}_{ij} \cdot \hat{\mathbf{s}}_{kl} + \cos\theta_{ij} \cos\theta_{kl}. \tag{B.4}$$

with $\hat{\mathbf{s}}_{ij}$ the direction of the spin S_{ij} in the plane. Let us now call the direction of the easy axis $\hat{\mathbf{n}} = a\hat{\mathbf{x}} + b\hat{\mathbf{y}}$, where $a^2 + b^2 = 1$. We can define $\phi_{\hat{\mathbf{n}}}$ so that $a = \cos\phi_{\hat{\mathbf{n}}}$ and $b = \sin\phi_{\hat{\mathbf{n}}}$. Then we can rewrite the last two terms of Eq. (B.2) as

$$\begin{aligned} -h \sum_{i,j} |S_{i,j}^{\hat{\mathbf{n}}}|^2 + k \sum_{i,j} |S_{i,j}^{\hat{\mathbf{z}}}|^2 &= -h \sum_{i,j} a \sin\theta_{ij} \cos\phi_{ij} + b \sin\theta_{ij} \sin\phi_{ij} + k \sum_{i,j} \cos\theta_{ij}{}^2 \\ &= -h \sum_{i,j} \cos\phi_{\hat{\mathbf{n}}} \sin\theta_{\hat{\mathbf{n}}} \cos\phi_{ij} + \sin\phi_{ij} \sin\theta_{ij} \sin\phi_{ij} + k \sum_{i,j} \cos\theta_{ij}{}^2 \\ &= -h \sum_{i,j} \sin^2\theta_{ij} \cos^2(\phi_{\hat{\mathbf{n}}} - \phi_{ij}) + k \sum_{i,j} \cos^2\theta_{ij}. \end{aligned} \tag{B.5}$$

We will compute the magnetic excitation of from the Hamiltonian by using the approximation of small spin oscillation. With this choice we can study the Hamiltonian for small angles α_i and β_i such as

$$\theta_{ij} = \frac{\pi}{2} + \alpha_{ij} \qquad \phi_{ij} = \phi_{\hat{\mathbf{n}}} + \beta_{ij} \tag{B.6}$$

As for the case of hexagonal lattice in Chapter 1, we consider the adjacent spins to have a 120° angle, Eq. (B.4) then becomes

$$\begin{aligned} S_{ij}S_{kl} &= -\frac{1}{2}(\sin\theta_{ij}\cos\phi_{ij}\sin\theta_{kl}\cos\phi_{kl} + \sin\theta_{ij}\sin\phi_{ij}\sin\theta_{kl}\sin\phi_{kl}) + \cos\theta_{ij}\cos\theta_{kl} \\ &= \sin\theta_{ij}\sin\theta_{kl}\cos(\phi_{ij}-\phi_{kl}) + \cos\theta_{ij}\cos\theta_{kl} \end{aligned} \tag{B.7}$$

and the expansion around small angles is

$$\theta_{ij} = \frac{\pi}{2} + \alpha_{ij} \qquad \phi_{ij} - \phi_{kl} = \frac{2\pi}{3} + \beta_{ij} - \beta_{kl} \tag{B.8}$$

and

$$\begin{aligned} \cos\theta_{ij} \approx \alpha_{ij} \qquad \sin\theta_{ij} \approx 1 - \frac{\alpha_{ij}^2}{2} \\ \cos(\phi_{ij}-\phi_{kl}) \approx -\frac{1}{2}\left(1 - \frac{\beta_{ij}^2}{2} - \frac{\beta_{kl}^2}{2} - \beta_{ij}\beta_{kl}\right) - \frac{\sqrt{3}}{2}(\beta_{ij}-\beta_{kl}) \end{aligned} \tag{B.9}$$

so that eq. (B.4) becomes

$$S_{ij}S_{kl} = -\frac{1}{2}\left(1 - \frac{\alpha_{ij}^2}{2} - \frac{\alpha_{kl}^2}{2} - \frac{\beta_{ij}^2}{2} - \frac{\beta_{kl}^2}{2} + \beta_{ij}\beta_{kl} - \sqrt{3}\beta_{ij} + \sqrt{3}\beta_{kl}\right) + \alpha_{ij}\alpha_{kl} \tag{B.10}$$

and we can rewrite the entire Hamiltonian as

$$\begin{aligned} H = \sum_{ij}^{N} J \Bigg[&-\frac{1}{2}\left(1 - \frac{\alpha_{ij}^2}{2} - \frac{\alpha_{i+1j}^2}{2} - \frac{\beta_{ij}^2}{2} - \frac{\beta_{i+1j}^2}{2} + \beta_{ij}\beta_{i+1j} + \sqrt{3}\beta_{ij} - \sqrt{3}\beta_{i+1j}\right) + \alpha_{ij}\alpha_{i+1j} \\ &-\frac{1}{2}\left(1 - \frac{\alpha_{ij}^2}{2} - \frac{\alpha_{ij+1}^2}{2} - \frac{\beta_{ij}^2}{2} - \frac{\beta_{ij+1}^2}{2} + \beta_{ij}\beta_{ij+1} + \sqrt{3}\beta_{ij} - \sqrt{3}\beta_{ij+1}\right) + \alpha_{ij}\alpha_{ij+1} \\ &-\frac{1}{2}\left(1 - \frac{\alpha_{ij}^2}{2} - \frac{\alpha_{i+1j-1}^2}{2} - \frac{\beta_{ij}^2}{2} - \frac{\beta_{i+1j-1}^2}{2} + \beta_{ij}\beta_{i+1j-1} + \sqrt{3}\beta_{ij} - \sqrt{3}\beta_{i+1j-1}\right) + \alpha_{ij}\alpha_{i+1j-1}\Bigg] \\ &- \sum_{ij} h\left(1 - \alpha_{ij}^2 - \beta_{ij}^2\right) + k\alpha_{ij}^2. \end{aligned} \tag{B.11}$$

We now are ready to derive the equations of motions for α and β

$$\dot{\alpha_{ij}}\sin\theta_i j = -\frac{\partial H}{\partial \beta_{ij}} \qquad \dot{\beta_{ij}}\sin\theta_i j = \frac{\partial H}{\partial \alpha_{ij}} \tag{B.12}$$

where the term $\sin\theta_i j$ arise from the choice of spherical coordinates. It follows that

$$\dot{\beta}_{ij} = J(\alpha_{i+1j} + \alpha_{ij+1} + \alpha_{i+1j-1} - \frac{3}{2}\alpha_{ij}) + 2h\alpha_{ij} + 2k\alpha_{ij} \tag{B.13}$$

$$\dot{\alpha}_{ij} = \frac{1}{2}J(\beta_{i+1j} + \beta_{ij+1} + \beta_{i+1j-1} - 3\beta_{ij}) + 2h\beta_{ij}, \tag{B.14}$$

the constant $\sqrt{3}$ term cancels out when summing over all sites. We then derive the expression for $\dot{\alpha}$ with respect to time and substitute the one for $\dot{\beta}$

$$\begin{aligned}\ddot{\alpha_{ij}} = \frac{1}{2}J\{J[\alpha_{i+2j} + \alpha_{i+1j+1} + \alpha_{i+2j-1} + 1/J(2k+2h-3/2J)\alpha_{i+1j}] \\ +J(\alpha_{i+1j+1} + \alpha_{ij+2} + \alpha_{i+1j} + 1/J(2k+2h-3/2J)\alpha_{ij+1}] \\ +J(\alpha_{i+2j-1} + \alpha_{i+1j} + \alpha_{i+2j-2} + 1/J(2k+2h-3/2J)\alpha_{i+1j-1}] \\ +(2h/J-3)J[\alpha_{i+1j} + \alpha_{ij+1} + \alpha_{i+1j-1} + 1/J(2k+2h-3/2J)\alpha_{ij}]\}.\end{aligned} \tag{B.15}$$

In order to obtain the dispersion relation for the magnons we move in Fourier space

$$\beta_j = e^{i\mathbf{q}\cdot\mathbf{r}_j - i\omega t}\beta_q \qquad \alpha_j = e^{i\mathbf{q}\cdot\mathbf{r}_j - i\omega t}\alpha_q \tag{B.16}$$

with $q = (q_x, q_y)$ the momentum in Fourier space and r_j gives the coordinates of j-th ion. Therefore we obtain from Eq. B.15

$$\begin{aligned}-\omega^2 = \frac{1}{2}\{J^2[2\cos 2q_x + 4\cos(q_x+q_y) + 4\cos(2q_x-q_y) + 2\cos 2q_y + 4\cos q_x \\ +4\cos(2q_x-2q_y)] + J(2k+2h-3/2J)(\cos q_x + \cos q_y + \cos(q_x-q_y)) \\ +J^2(2h/J-3)[2\cos q_x + 2\cos q_y + 2\cos(q_x-q_y)] \\ +J(2h/J-3)(2k+2h-3/2J)\}\end{aligned} \tag{B.17}$$

lattice constant is supposed equal to 1. Finally the dispersion relation for a magnon in an hexagonal lattice is the following

$$\begin{aligned}\omega^2 = -J^2[\cos 2q_x + 2\cos(q_x+q_y) + 2\cos(2q_x-q_y) + \cos 2q_y + 2\cos q_x \\ +2\cos(2q_x-2q_y)] - J(2k+2h-3/2J)[\cos q_x + \cos q_y + \cos(q_x-q_y)] \\ -J^2(2h/J-3)[\cos q_x + \cos q_y - \cos(q_x-q_y)] \\ +J(2h/J-3)(2k+2h-3/2J).\end{aligned} \tag{B.18}$$

B.2 Magnetic susceptibility

The final step to compute the magnon spectral function is to obtain the magnetic susceptibility.

The equation of motion (B.12) give rise to an eigenvector problem

$$(A - i\omega\mathbb{1})\begin{pmatrix}\alpha_q \\ \beta_q\end{pmatrix} = 0 \tag{B.19}$$

with A the matrix of derivatives of the Hamiltonian respect to the variables α_i, β_i.

$$A = \begin{pmatrix}\partial_{\beta_i\alpha_j} & \partial_{\beta_i\beta_j} \\ -\partial_{\alpha_i\alpha_j} & -\partial_{\alpha_i\beta_i}\end{pmatrix}\mathcal{H} \tag{B.20}$$

In the previous section we effectively solved $\det[A - i\omega\mathbf{I}] = 0$ in order to compute the dispersion relation $\omega(q_x, q_y)$. The magnon spectral function is the magnetic susceptibility that, e.g., INS experiments measure. Magnetic susceptibility is the derivative of magnetization $\mathbf{M}$ with respect to magnetic field $\mathbf{h}$ and magnetization is computed by averaging the magnetic moment of every spins in the material, therefore the susceptibility is

$$\chi_{ij} = \frac{1}{V}\sum_{kl}\frac{\partial\mu_{kl}^{(i)}}{\partial h^{(j)}} \tag{B.21}$$

with $\mu = g_s\, e/2m_e\, \mathbf{S}$ magnetic moment due to the spin and k and l are the lattice indices. $\mathbf{S}$ is a function of α and β, not $\mathbf{h}$. We can express $\mathbf{S}$ in term of $\mathbf{h}$ by solving (q-part of Fourier Transform is omitted)

$$(A - i\omega\mathbb{1}) \begin{pmatrix} \alpha_q \\ \beta_q \end{pmatrix} e^{-i\omega t} = \begin{pmatrix} h_\alpha \\ h_\beta \end{pmatrix} e^{-i\bar{\omega} t} \tag{B.22}$$

with $\begin{pmatrix} h_\alpha \\ h_\beta \end{pmatrix}$ linear component in α and β of the term $\vec{S}\cdot\vec{h}$. The frequency $\bar{\omega}$ is the frequency of the oscillating magnetic field associated to neutrons in neutron scattering experiments. The system will be forced to oscillate at the external magnetic frequency, so $\omega = \bar{\omega}$ and

$$\begin{pmatrix} \alpha_q \\ \beta_q \end{pmatrix} = (A - i\omega\mathbb{1})^{-1} \begin{pmatrix} h_\alpha \\ h_\beta \end{pmatrix} \tag{B.23}$$

substituting (B.23) into (B.21) we get an expression for the susceptibility $\chi(\omega, q_x, q_y)$.

Finally, the neutron scattering cross section for unpolarized spins is computed from the susceptibility with the use of a form factor due to dipole-dipole interactions [16]

$$\frac{d^2\sigma}{dEd\Omega} \sim \sum_{ij} \left(\delta_{ij} - \frac{k_i k_j}{k^2} \right) \chi_{ij} \tag{B.24}$$

Appendix C

Single-spin entropy Contribution

Here we derive Eq. 3.2. We consider the simple case of one spin **S** in an external magnetic field **H**. In Eq. 3.2 **H** is the effective magnetic field that is acting on the spin **S**. The partition function in the case of a classical spin is

$$Z = \int e^{-\frac{\mathbf{H}\cdot\mathbf{S}}{T}} d\mathbf{S} \tag{C.1}$$

where we consider $k_B = 1$. We express the previous integral in polar coordinates and expand the scalar product in the exponential

$$Z = \int_1^1 2\pi e^{-\frac{HS\cos\theta}{T}} d(\cos\theta), \tag{C.2}$$

that, once integrated, results in

$$Z = \frac{4\pi T}{HS} \sinh\frac{HS}{T}. \tag{C.3}$$

We can now write the free energy of the system

$$F = -T\log Z, \tag{C.4}$$

and, from that, the entropy

$$\begin{aligned}\mathcal{S} = -\frac{\partial F}{\partial T} &= \log\left[\frac{4\pi T}{HS}\sinh\frac{HS}{T}\right] + \frac{T}{\frac{4\pi T}{HS}\sinh\frac{HS}{T}}\left(\frac{4\pi}{HS}\sinh\frac{HS}{T} - \frac{4\pi}{HS}\frac{HS}{T}\cosh\frac{HS}{T}\right) \\ &= \log\left[\frac{4\pi T}{HS}\sinh\frac{HS}{T}\right] + \left(1 - \frac{HS}{T}\coth\frac{HS}{T}\right),\end{aligned} \tag{C.5}$$

and, if $HS/T = x$, and up to a constant term, reduces to eq. 3.2

$$\mathcal{S} = \log\left[\frac{\sinh x}{x}\right] - x\coth x. \tag{C.6}$$

Fig. C.1 shows the entropy behavior as a function of x, i.e. the field **H**. We observe from the figure that, for fixed T and S, higher values of effective field H correspond to lower entropy. This is consistent with the argument in Section 3.2.

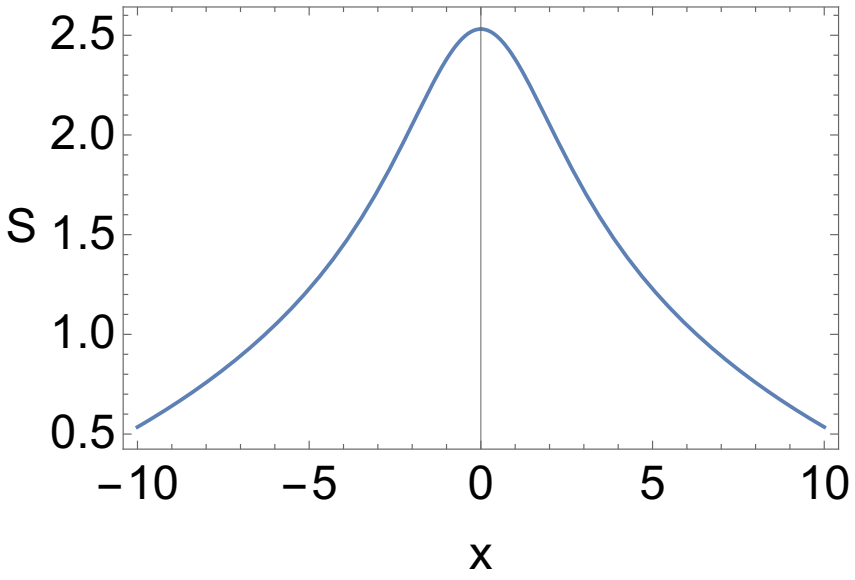

Figure C.1: Single spin entropy in mean field approximation as a function of the variable $x = HS/T$.

References

[1] Sang-Wook Cheong and Maxim Mostovoy. "Multiferroics: a magnetic twist for ferroelectricity". In: *Nature Materials* 6 (2007), p. 13. URL: https://doi.org/10.1038/nmat1804.

[2] Daniel Khomskii. "Classifying multiferroics: Mechanisms and effects". In: *Physics* 2 (2009), p. 20. URL: https://physics.aps.org/articles/v2/20.

[3] Wenbin Wang et al. "Room-Temperature Multiferroic Hexagonal $LuFeO_3$ Films". In: *Phys. Rev. Lett.* 110 (23 2013), p. 237601. DOI: 10.1103/PhysRevLett.110.237601. URL: https://link.aps.org/doi/10.1103/PhysRevLett.110.237601.

[4] Steven M. Disseler et al. "Multiferroicity in doped hexagonal $LuFeO_3$". In: *Phys. Rev. B* 92 (5 2015), p. 054435. DOI: 10.1103/PhysRevB.92.054435. URL: https://link.aps.org/doi/10.1103/PhysRevB.92.054435.

[5] R. Ramesh and Nicola A. Spaldin. "Multiferroics: progress and prospects in thin films". In: *Nature Materials* 6 (2007), p. 21. URL: https://doi.org/10.1038/nmat1805.

[6] A. Muñoz et al. "Magnetic structure of hexagonal $R\mathrm{MnO}_3$ ($R = \mathrm{Y}, \mathrm{Sc}$) : Thermal evolution from neutron powder diffraction data". In: *Phys. Rev. B* 62 (14 2000), pp. 9498–9510. DOI: 10.1103/PhysRevB.62.9498. URL: https://link.aps.org/doi/10.1103/PhysRevB.62.9498.

[7] D I Khomskii. "Magnetic monopoles and unusual dynamics of magnetoelectrics". In: *Nature Communications* 5 (2014), p. 4793. URL: https://doi.org/10.1038/ncomms5793%20http://10.0.4.14/ncomms5793.

[8] Sang-Wook Cheong. "SOS: symmetry-operational similarity". In: *npj Quantum Materials* 4.1 (2019), p. 53. ISSN: 2397-4648. DOI: 10.1038/s41535-019-0193-9. URL: https://doi.org/10.1038/s41535-019-0193-9.

[9] IE Dzyaloshinskii. "On the Magneto-Electrical Effect in Antiferromagnets". In: *Sov. Phys. JETP* 10.3 (1960), p. 628.

[10] IE Dzyaloshinskii. "Theory of helicoidal structures in antiferromagnets. I. Nonmetals". In: *Sov. Phys. JETP* 19.4 (1964), pp. 960–971.

[11] Tôru Moriya. "Anisotropic Superexchange Interaction and Weak Ferromagnetism". In: *Phys. Rev.* 120 (1 1960), pp. 91–98. DOI: 10.1103/PhysRev.120.91. URL: https://link.aps.org/doi/10.1103/PhysRev.120.91.

[12] Hena Das et al. "Bulk magnetoelectricity in the hexagonal manganites and ferrites". In: *Nature Communications* 5 (2014), p. 2998. ISSN: 1. DOI: 10.1038/ncomms3998. URL: https://doi.org/10.1038/ncomms3998.

[13] M. Fiebig, Th. Lottermoser, and R. V. Pisarev. "Spin-rotation phenomena and magnetic phase diagrams of hexagonal RMnO3". In: *Journal of Applied Physics* 93.10 (2003), pp. 8194–8196. DOI: 10.1063/1.1544513. eprint: https://doi.org/10.1063/1.1544513. URL: https://doi.org/10.1063/1.1544513.

[14] Assa Auerbach. *Interacting Electrons and Quantum Magnetism*. Springer-Verlag, 1994.

[15] J. C. Leiner et al. "Magnetic excitations in the bulk multiferroic two-dimensional triangular lattice antiferromagnet (Lu,Sc)FeO3". In: *Physical Review B* 98 (13 2018), p. 134412. DOI: 10.1103/PhysRevB.98.134412. URL: https://link.aps.org/doi/10.1103/PhysRevB.98.134412.

[16] Jens Jensen and Allan R. Mackintosh. "Rare Earth Magnetism: Structures and Excitations". In: Clarendon Press, Oxford, 1991, p. 174. URL: https://www.fys.ku.dk/~jjensen/Book/Ebook.pdf.

[17] Nicola A Spaldin, Manfred Fiebig, and Maxim Mostovoy. "The toroidal moment in condensed-matter physics and its relation to the magnetoelectric effect". In: *Journal of Physics: Condensed Matter* 20.43 (2008), p. 434203. DOI: 10.1088/0953-8984/20/43/434203. URL: https://doi.org/10.1088/0953-8984/20/43/434203.

[18] Naëmi Leo et al. "Polarization control at spin-driven ferroelectric domain walls". In: *Nature Communications* 6.1 (2015), p. 6661. ISSN: 2041-1723. DOI: 10.1038/ncomms7661. URL: https://doi.org/10.1038/ncomms7661.

[19] T. Kimura et al. "Magnetic control of ferroelectric polarization". In: *Nature* 426.6962 (2003), pp. 55–58. ISSN: 1476-4687. DOI: 10.1038/nature02018. URL: https://doi.org/10.1038/nature02018.

[20] A. Pimenov et al. "Possible evidence for electromagnons in multiferroic manganites". In: *Nature Physics* 2.2 (2006), pp. 97–100. ISSN: 1745-2481. DOI: 10.1038/nphys212. URL: https://doi.org/10.1038/nphys212.

[21] Natalya S. Fedorova et al. "Biquadratic and ring exchange interactions in orthorhombic perovskite manganites". In: *Phys. Rev. B* 91 (16 2015), p. 165122. DOI: 10.1103/PhysRevB.91.165122. URL: https://link.aps.org/doi/10.1103/PhysRevB.91.165122.

[22] Souvik Paul et al. "Role of higher-order exchange interactions for skyrmion stability". In: *Nature communications* 11.1 (2020), pp. 1–12.

[23] Jaehong Jeong et al. "Temperature-Dependent Interplay of Dzyaloshinskii-Moriya Interaction and Single-Ion Anisotropy in Multiferroic $BiFeO_3$". In: *Phys. Rev. Lett.* 113 (10 2014), p. 107202. DOI: 10.1103/PhysRevLett.113.107202. URL: https://link.aps.org/doi/10.1103/PhysRevLett.113.107202.

[24] D. Senff et al. "Magnetic Excitations in Multiferroic $TbMnO_3$: Evidence for a Hybridized Soft Mode". In: *Phys. Rev. Lett.* 98 (13 2007), p. 137206. DOI: 10.1103/PhysRevLett.98.137206. URL: https://link.aps.org/doi/10.1103/PhysRevLett.98.137206.

[25] D Senff et al. "Magnetic excitations in a cycloidal magnet: the magnon spectrum of multiferroic TbMnO3". In: *Journal of Physics: Condensed Matter* 20.43 (2008), p. 434212. DOI: 10.1088/0953-8984/20/43/434212. URL: https://doi.org/10.1088%2F0953-8984%2F20%2F43%2F434212.

[26] K. Taniguchi et al. "Magnetic-field dependence of the ferroelectric polarization and spin-lattice coupling in multiferroic $MnWO_4$". In: *Phys. Rev. B* 77 (6 2008), p. 064408. DOI: 10.1103/PhysRevB.77.064408. URL: https://link.aps.org/doi/10.1103/PhysRevB.77.064408.

[27] I. A. Sergienko and E. Dagotto. "Role of the Dzyaloshinskii-Moriya interaction in multiferroic perovskites". In: *Phys. Rev. B* 73 (9 2006), p. 094434. DOI: 10.1103/PhysRevB.73.094434. URL: https://link.aps.org/doi/10.1103/PhysRevB.73.094434.

[28] Maxim Mostovoy. "Ferroelectricity in Spiral Magnets". In: *Phys. Rev. Lett.* 96 (6 2006), p. 067601. DOI: 10.1103/PhysRevLett.96.067601. URL: https://link.aps.org/doi/10.1103/PhysRevLett.96.067601.

[29] Hosho Katsura, Naoto Nagaosa, and Alexander V. Balatsky. "Spin Current and Magnetoelectric Effect in Noncollinear Magnets". In: *Phys. Rev. Lett.* 95 (5 2005), p. 057205. DOI: 10.1103/PhysRevLett.95.057205. URL: https://link.aps.org/doi/10.1103/PhysRevLett.95.057205.

[30] M. Schmidt et al. "Far-infrared optical excitations in multiferroic TbMnO3". In: *The European Physical Journal B* 71.3 (2009), p. 411. ISSN: 1434-6036. DOI: 10.1140/epjb/e2009-00215-3. URL: https://doi.org/10.1140/epjb/e2009-00215-3.

[31] F. Kagawa et al. "Dynamics of multiferroic domain wall in spin-cycloidal ferroelectric $DyMnO_3$". In: *Phys. Rev. Lett.* 102.5 (2009), p. 057604. DOI: 10.1103/PhysRevLett.102.057604. URL: https://link.aps.org/doi/10.1103/PhysRevLett.102.057604.

[32] F. Kagawa et al. "Relaxation dynamics of multiferroic domain walls in $DyMnO_3$ with cycloidal spin order". In: *Phys. Rev. B* 83 (5 2011), p. 054413. DOI: 10.1103/PhysRevB.83.054413. URL: https://link.aps.org/doi/10.1103/PhysRevB.83.054413.

[33] P. Marton, V. Stepkova, and J. Hlinka. "Divergence of dielectric permittivity near phase transition within ferroelectric domain boundaries". In: *Phase Transitions* 86.1 (2013), pp. 103–108. DOI: 10.1080/01411594.2012.727211. eprint: https://doi.org/10.1080/01411594.2012.727211. URL: https://doi.org/10.1080/01411594.2012.727211.

[34] Markus Garst, Johannes Waizner, and Dirk Grundler. "Collective spin excitations of helices and magnetic skyrmions: review and perspectives of magnonics in non-centrosymmetric magnets". In: *Journal of Physics D: Applied Physics* 50.29 (2017), p. 293002.

[35] P. Padmanabhan et al. "Optically Driven Collective Spin Excitations and Magnetization Dynamics in the Néel-type Skyrmion Host GaV_4S_8". In: *Phys. Rev. Lett.* 122 (10 2019), p. 107203. DOI: 10.1103/PhysRevLett.122.107203. URL: https://link.aps.org/doi/10.1103/PhysRevLett.122.107203.

[36] I. Kezsmarki et al. "Neel-type skyrmion lattice with confined orientation in the polar magnetic semiconductor GaV4S8". In: *Nature Materials* 14.11 (2015), pp. 1116–1122. ISSN: 14764660. DOI: 10.1038/nmat4402. arXiv: 1502.08049.

[37] V. Ta Phuoc et al. “Optical Conductivity Measurements of $GaTa_4Se_8$ Under High Pressure: Evidence of a Bandwidth-Controlled Insulator-to-Metal Mott Transition”. In: *Phys. Rev. Lett.* 110 (3 2013), p. 037401. DOI: 10.1103/PhysRevLett.110.037401. URL: https://link.aps.org/doi/10.1103/PhysRevLett.110.037401.

[38] Eugen Dorolti et al. “Half-Metallic Ferromagnetism and Large Negative Magnetoresistance in the New Lacunar Spinel GaTi3VS8”. In: *Journal of the American Chemical Society* 132.16 (2010). PMID: 20356073, pp. 5704–5710. DOI: 10.1021/ja908128b. eprint: https://doi.org/10.1021/ja908128b. URL: https://doi.org/10.1021/ja908128b.

[39] Regina Pocha, Dirk Johrendt, and Rainer Pöttgen. “Electronic and Structural Instabilities in GaV4S8 and GaMo4S8”. In: *Chemistry of Materials* 12.10 (2000), pp. 2882–2887. DOI: 10.1021/cm001099b. eprint: https://doi.org/10.1021/cm001099b. URL: https://doi.org/10.1021/cm001099b.

[40] Yoshihiko Okamoto et al. “Breathing Pyrochlore Lattice Realized in *A*-Site Ordered Spinel Oxides $LiGaCr_4O_8$ and $LiInCr_4O_8$”. In: *Phys. Rev. Lett.* 110 (9 2013), p. 097203. DOI: 10.1103/PhysRevLett.110.097203. URL: https://link.aps.org/doi/10.1103/PhysRevLett.110.097203.

[41] D Ehlers et al. “Exchange anisotropy in the skyrmion host GaV4S8”. In: *Journal of Physics: Condensed Matter* 29.6 (2016), p. 065803. DOI: 10.1088/1361-648x/aa4e7e. URL: https://doi.org/10.1088/1361-648x/aa4e7e.

[42] P. Weinberger. “John Kerr and his effects found in 1877 and 1878”. In: *Philosophical Magazine Letters* 88.12 (2008), pp. 897–907. DOI: 10.1080/09500830802526604.

[43] N. Ogawa, S. Seki, and Y. Tokura. “Ultrafast optical excitation of magnetic skyrmions”. In: *Scientific Reports* 5 (2015), pp. 1–5. ISSN: 20452322. DOI: 10.1038/srep09552.

[44] Fumiya Sekiguchi et al. “Skyrmion signatures in the ultrafast time domain: coherent and incoherent photo-excited spin dynamics of Néel-type skyrmion host GaV_4S_8”. In: *in preparation* (2021).

[45] L. D. Landau and E. M. Lifshitz. “Theory of the dispersion of magnetic permeability in ferromagnetic bodies”. In: *Phys. Z. Sowjetunion* 8 (1935), p. 153.

[46] B Skubic et al. “A method for atomistic spin dynamics simulations: implementation and examples”. In: *Journal of Physics: Condensed Matter* 20.31 (2008), p. 315203. DOI: 10.1088/0953-8984/20/31/315203. URL: https://doi.org/10.1088/0953-8984/20/31/315203.

[47] S. A. Nikolaev and I. V. Solovyev. “Microscopic theory of electric polarization induced by skyrmionic order in GaV4 S8”. In: *Physical Review B* 99.10 (2019). ISSN: 24699969. DOI: 10.1103/PhysRevB.99.100401. arXiv: arXiv:1808.08008v2.

[48] R F L Evans et al. “Atomistic spin model simulations of magnetic nanomaterials”. In: *Journal of Physics: Condensed Matter* 26.10 (2014), p. 103202. DOI: 10.1088/0953-8984/26/10/103202. URL: https://doi.org/10.1088/0953-8984/26/10/103202.

[49] Manuel Sánchez-Sánchez et al. “Synthesis of metal–organic frameworks in water at room temperature: salts as linker sources”. In: *Green Chemistry* 17.3 (2015), pp. 1500–1509.

[50] Yinina Ma and Young Sun. "Multiferroic and thermal expansion properties of metal-organic frameworks". In: *Journal of Applied Physics* 127.8 (2020), p. 080901. DOI: 10.1063/1.5137819.

[51] Hui Li et al. "Novel single component tri-rare-earth emitting MOF for warm white light LEDs". In: *Dalton Trans.* 47 (25 2018), pp. 8427–8433. DOI: 10.1039/C8DT01477A. URL: http://dx.doi.org/10.1039/C8DT01477A.

[52] Prashant Jain et al. "Order-Disorder Antiferroelectric Phase Transition in a Hybrid Inorganic-Organic Framework with the Perovskite Architecture". In: *Journal of the American Chemical Society* 130.32 (2008), pp. 10450–10451. ISSN: 0002-7863. DOI: 10.1021/ja801952e. URL: https://doi.org/10.1021/ja801952e.

[53] Prashant Jain et al. "Multiferroic Behavior Associated with an Order-Disorder Hydrogen Bonding Transition in Metal-Organic Frameworks (MOFs) with the Perovskite ABX3 Architecture". In: *Journal of the American Chemical Society* 131.38 (2009), pp. 13625–13627. DOI: 10.1021/ja904156s.

[54] Laura Cañadillas-Delgado et al. "The Role of Order–Disorder Transitions in the Quest for Molecular Multiferroics: Structural and Magnetic Neutron Studies of a Mixed Valence Iron(II)–Iron(III) Formate Framework". In: *Journal of the American Chemical Society* 134.48 (2012), pp. 19772–19781. ISSN: 0002-7863. DOI: 10.1021/ja3082457. URL: https://doi.org/10.1021/ja3082457.

[55] Prashant Jain et al. "Switchable electric polarization and ferroelectric domains in a metal-organic-framework". In: *NPJ Quantum Materials* 1 (2016), p. 16012. DOI: 10.1038/npjquantmats.2016.12https://www.nature.com/articles/npjquantmats201612#supplementary-information. URL: https://doi.org/10.1038/npjquantmats.2016.12.

[56] S. Horiuchi and Y. Tokura. "Organic ferroelectrics". In: *Nat Mater* 7.5 (2008), pp. 357–66. ISSN: 1476-1122 (Print) 1476-1122 (Linking). DOI: 10.1038/nmat2137. URL: https://www.ncbi.nlm.nih.gov/pubmed/18432209.

[57] Alessandro Stroppa et al. "Electric control of magnetization and interplay between orbital ordering and ferroelectricity in a multiferroic metal–organic framework". In: *Angewandte Chemie International Edition* 50.26 (2011), pp. 5847–5850.

[58] Ying Tian et al. "High-temperature ferroelectricity and strong magnetoelectric effects in a hybrid organic–inorganic perovskite framework". In: *physica status solidi (RRL)–Rapid Research Letters* 9.1 (2015), pp. 62–67.

[59] Jiangbin Guo et al. "An insight into the magnetoelectric coupling effect in the MOF of [NH2(CH3)2]n[FeIIIFeII(HCOO)6]n". In: *Applied Physics Letters* 110.19 (2017), p. 192902. DOI: 10.1063/1.4983169. eprint: https://doi.org/10.1063/1.4983169. URL: https://doi.org/10.1063/1.4983169.

[60] Gang Tang et al. "First-principles study of the structural, electronic, magnetic, and ferroelectric properties of a charge-ordered iron(ii)-iron(iii) formate framework". In: *The Journal of Chemical Physics* 151.12 (2019), p. 124704. DOI: 10.1063/1.5116343. eprint: https://doi.org/10.1063/1.5116343. URL: https://doi.org/10.1063/1.5116343.

[61] Wei Li et al. "Ferroelasticity in a metal–organic framework perovskite; towards a new class of multiferroics". In: *Acta materialia* 61.13 (2013), pp. 4928–4938.

[62] Mantas Šimėnas et al. “Simulation of Structural Phase Transitions in Perovskite Methylhydrazinium Metal–Formate Frameworks: Coupled Ising and Potts Models”. In: *The Journal of Physical Chemistry C* 123.32 (2019), pp. 19912–19919. ISSN: 1932-7447. DOI: 10.1021/acs.jpcc.9b03448. URL: https://doi.org/10.1021/acs.jpcc.9b03448.

[63] Mildred S Dresselhaus, Gene Dresselhaus, and Ado Jorio. *Group theory: application to the physics of condensed matter*. Springer Science & Business Media, 2007.

[64] E Ascher and J Kobayashi. “Symmetry and phase transitions: The inverse Landau problem”. In: *Journal of Physics C: Solid State Physics* 10.9 (1977), pp. 1349–1363. DOI: 10.1088/0022-3719/10/9/009. URL: https://doi.org/10.1088/0022-3719/10/9/009.

[65] Sergey Artyukhin et al. “Landau theory of topological defects in multiferroic hexagonal manganites”. In: *Nature Materials* 13 (2014), p. 42. DOI: 10.1038/nmat3786. URL: https://doi.org/10.1038/nmat3786.

[66] Greg Mills and Hannes Jónsson. “Quantum and thermal effects in H_2 dissociative adsorption: Evaluation of free energy barriers in multidimensional quantum systems”. In: *Phys. Rev. Lett.* 72 (7 1994), pp. 1124–1127. DOI: 10.1103/PhysRevLett.72.1124. URL: https://link.aps.org/doi/10.1103/PhysRevLett.72.1124.

[67] Paolo Giannozzi et al. “QUANTUM ESPRESSO: a modular and open-source software project for quantum simulations of materials”. In: *Journal of Physics: Condensed Matter* 21.39 (2009), 395502 (19pp). URL: http://www.quantum-espresso.org.

[68] P Giannozzi et al. “Advanced capabilities for materials modelling with QUANTUM ESPRESSO”. In: *Journal of Physics: Condensed Matter* 29.46 (2017), p. 465901. URL: http://stacks.iop.org/0953-8984/29/i=46/a=465901.

[69] G. L. Pascut et al. “Dimerization-Induced Cross-Layer Quasi-Two-Dimensionality in Metallic $IrTe_2$”. In: *Phys. Rev. Lett.* 112 (8 2014), p. 086402. DOI: 10.1103/PhysRevLett.112.086402. URL: https://link.aps.org/doi/10.1103/PhysRevLett.112.086402.

[70] G. L. Pascut et al. “Series of alternating states with unpolarized and spin-polarized bands in dimerized $IrTe_2$”. In: *Phys. Rev. B* 90 (19 2014), p. 195122. DOI: 10.1103/PhysRevB.90.195122. URL: https://link.aps.org/doi/10.1103/PhysRevB.90.195122.

[71] AF Fang et al. “Structural phase transition in IrTe 2: A combined study of optical spectroscopy and band structure calculations”. In: *Scientific reports* 3.1 (2013), pp. 1–6.

[72] Masaro Yoshida et al. “Metastable Superconductivity in Two-Dimensional IrTe2 Crystals”. In: *Nano Letters* 18.5 (2018). PMID: 29609462, pp. 3113–3117. DOI: 10.1021/acs.nanolett.8b00673. eprint: https://doi.org/10.1021/acs.nanolett.8b00673. URL: https://doi.org/10.1021/acs.nanolett.8b00673.

[73] Sajedeh Manzeli et al. “2D transition metal dichalcogenides”. In: *Nature Reviews Materials* 2.8 (2017), pp. 1–15.

[74] Sunseng Pyon, Kazutaka Kudo, and Minoru Nohara. “Superconductivity induced by bond breaking in the triangular lattice of IrTe2”. In: *Journal of the Physical Society of Japan* 81.5 (2012), p. 053701.

[75] JJ Yang et al. "Charge-orbital density wave and superconductivity in the strong spin-orbit coupled $IrTe_2$ Pd". In: *Physical review letters* 108.11 (2012), p. 116402.

[76] Huibo Cao et al. "Origin of the phase transition in $IrTe_2$: Structural modulation and local bonding instability". In: *Phys. Rev. B* 88 (11 2013), p. 115122. DOI: 10.1103/PhysRevB.88.115122. URL: https://link.aps.org/doi/10.1103/PhysRevB.88.115122.

[77] D Ootsuki et al. "Band Jahn-Teller effects and Peierls Instability in IrTe2". In: *Journal of Physics: Conference Series* 428 (2013), p. 012018. DOI: 10.1088/1742-6596/428/1/012018. URL: https://doi.org/10.1088/1742-6596/428/1/012018.

[78] M. Rumo et al. "Examining the surface phase diagram of $IrTe_2$ with photoemission". In: *Phys. Rev. B* 101 (23 2020), p. 235120. DOI: 10.1103/PhysRevB.101.235120. URL: https://link.aps.org/doi/10.1103/PhysRevB.101.235120.

[79] Y. Fujisawa et al. "Scanning tunneling microscopy and spectroscopy study of the patchwork structure in Pt doped IrTe2". In: *Physica C: Superconductivity and its Applications* 530 (2016). 28th International Symposium on Superconductivity, pp. 35–37. ISSN: 0921-4534. DOI: https://doi.org/10.1016/j.physc.2016.01.007. URL: https://www.sciencedirect.com/science/article/pii/S0921453416000137.

[80] Per Bak and Van Der Merwe. "Ising model with solitons, phasons, and". In: 21.11 (1980).

[81] Gabriele Saleh and Sergey Artyukhin. "First-Principles Theory of Phase Transitions in IrTe2". In: *The Journal of Physical Chemistry Letters* 11.6 (2020). PMID: 32079398, pp. 2127–2132. DOI: 10.1021/acs.jpclett.0c00012. eprint: https://doi.org/10.1021/acs.jpclett.0c00012. URL: https://doi.org/10.1021/acs.jpclett.0c00012.

[82] K-T Ko et al. "Charge-ordering cascade with spin–orbit Mott dimer states in metallic iridium ditelluride". In: *Nature communications* 6.1 (2015), pp. 1–7.

[83] D. I Khomskii and K. I Kugel. "Why stripes? Spontaneous formation of inhomogeneous structures due to elastic interactions". In: *Europhysics Letters (EPL)* 55.2 (2001), pp. 208–213. DOI: 10.1209/epl/i2001-00401-5.

[84] D. I. Khomskii and K. I. Kugel. "Elastic interactions and superstructures in manganites and other Jahn-Teller systems". In: *Phys. Rev. B* 67 (13 2003), p. 134401. DOI: 10.1103/PhysRevB.67.134401. URL: https://link.aps.org/doi/10.1103/PhysRevB.67.134401.

[85] Pasquale Pavone, Stefano Baroni, and Stefano de Gironcoli. "$\alpha \leftrightarrow \beta$ phase transition in tin: A theoretical study based on density-functional perturbation theory". In: *Phys. Rev. B* 57 (17 1998), pp. 10421–10423. DOI: 10.1103/PhysRevB.57.10421. URL: https://link.aps.org/doi/10.1103/PhysRevB.57.10421.